Study of Water Droplet Trajectories in the NASA Lewis Research Center Icing Research Tunnel (IRT)

Andrew L. Reehorst
Lewis Research Center
Cleveland, Ohio

May 1996

Study of Water Droplet Trajectories

in the NASA Lewis Research Center

Icing Research Tunnel (IRT).

ANDREW L. REEHORST

Abstract

Water droplet trajectories within the NASA Lewis Research Center's Icing Research Tunnel (IRT) were studied through both experiment and computer analysis. Of interest was the influence of the wind tunnel contraction and wind tunnel model blockage on the water droplet trajectories. The computer analysis was carried out with a program package consisting of a three-dimensional potential panel code with integral boundary layer modeling and a three-dimensional droplet trajectory code utilizing a "local Stokes" approximation. An initial computational parameter study was performed using a spherical geometry to assess the accuracy of the computer code methodology. The gravity term was examined by calculating droplets falling in stagnant air. An experiment was conducted that consisted of a single moveable nozzle spraying water onto a grid installed in the center of the tunnel test section. Water impingement on the grid was recorded with the use of blotter paper. Agreement between the calculated trajectories within the IRT and the experimental data was found to be very good. The wind tunnel contraction was found to influence the water droplet cloud size distribution and liquid water content distribution across the test section from that at the inlet. The wind tunnel walls were found to have negligible influence upon the impingement of water droplets upon a wing model.

Table of Contents

v

Nomenclature

2-D	Two-Dimensional
3-D	Three-Dimensional
Beta	Local water collection efficiency, dimensionless
C_D	Drag coefficient, Drag/q_S, dimensionless
D	Droplet diameter, microns
F_{aero}	Aerodynamic forces acting on a droplet, newton (lbf)
F_{buoy}	Buoyancy forces acting on a droplet, newton (lbf)
F_{grav}	Gravitational force acting on a droplet, newton (lbf)
g	Gravitational acceleration constant, 9.80665 m/s^2
IRT	Icing Research Tunnel
LWC	Liquid Water Content, g/m^3
m	Droplet mass, kg (lbm)
MVD	Mean Volumetric Diameter, microns
NASA	National Aeronautics and Space Administration
NACA	National Advisory Committee on Aeronautics
Re	Reynolds number, _Vl/_, dimensionless
S	Reference area of the droplet, _D^2/4, m^2 (ft^2)
V_p	Droplet velocity relative to a fixed reference point, m/s (ft/s)
V_{rel}	Relative velocity between the air and the droplet, m/s (ft/s)
δ	Boundary-layer thickness, m (ft)
$\delta*$	Boundary-layer displacement thickness, m (ft)

ρ Density of air, kg/m^3 $(slug/ft^3)$

ρ_{H2O} Density of water, kg/m^3 $(slug/ft^3)$

Subscripts:

i-1   Previous time step

r   Radial direction in cylindrical coordinate system

z   Axial direction in cylindrical coordinate system

List of Tables

LIST OF FIGURES

xiv

CHAPTER I

INTRODUCTION

1.1 Aircraft Icing Background

The growth of ice on aircraft has been a problem since the time that aircraft first began flying by instruments into visible moisture. Over the years several methods have been developed to examine and hopefully control the aircraft ice accretion process. Data was first obtained by personal accounts of pilots that were unfortunate enough to stray into the icing environment. Later, flight test personnel purposely attempted to accrete ice on their aircraft by flying into known icing conditions. Flight testing is both hazardous, time-consuming, and expensive. To provide controlled testing conditions, refrigerated wind tunnels with water spray systems were developed. This new capability provided a new means to gain better understanding.

1

of the icing phenomenon and develop improved ice protection systems. But even wind tunnel testing can be quite expensive and is not fully compatible with all initial design efforts. Computer analysis provides a powerful tool for engineers during the early phases of design. Initially, mechanical machines were used to predict the flowfield and water droplet trajectories around various aerodynamic surfaces. With the advancement of digital computers, the mechanical machines were quickly displaced. By the mid-1980's several computer codes were developed to calculate the flowfield and water droplet trajectories about arbitrarily shaped bodies. The first codes were strictly 2-D in nature. Today, several codes are capable of performing these calculations for arbitrary 3-D surfaces. Due to these advancements one may now use these computational tools to study the icing wind tunnels. What are the effects of the wind tunnel's contraction upon the water droplet trajectories and the distribution of water droplets in the test section? How can one compare the water impingement from the wind tunnel's artificial icing cloud contained within the tunnel walls to that of a natural icing cloud impinging upon a wing with no surrounding walls? These are the questions that may be now answered with the help of computer analysis and will be addressed in this thesis.

1.2 Basic physics of aircraft icing

Ice accretes on aerodynamic surfaces in flight when an aircraft flying in sub-freezing temperatures makes contact with liquid water. This liquid water is normally in the form of a cloud of water droplets that are super-cooled (below freezing, yet still liquid). The aircraft flying through the icing cloud strikes droplets which either freeze on contact (in colder events) forming rime ice or flow briefly before freezing (for warmer events) forming glaze ice. Before the droplets strike the aircraft they are influenced by the air movement about the vehicle. As the air upstream of the vehicle is displaced to move around the body, the aerodynamic forces acting on the droplets cause them to also be displaced (since the droplets can be seen as non-lifting spheres, the aerodynamic forces can be reduced to drag only). However, the acceleration of the droplets is strongly dependent upon their mass (size). This causes different sized droplets to be displaced at different rates which controls the water impingement rate and therefore the ice accretion rate. Very large droplets will impinge an airfoil rather uniformly over the forward facing surface since they are not greatly influenced by the aerodynamic forces. On the other hand, smaller droplets may only impinge the airfoil around the stagnation line. Also, the overall water impingement on the aerodynamic surface will be

significantly lower for the case of the smaller droplets.

1.3 Literature Review

Due to the complex nature of the computation of droplet trajectories with a wind tunnel and the limits of the computational tools, little work had been performed in this area until quite recently. Because of the development of both high speed computers and flow prediction codes, this problem has just begun to be examined. Several individuals have looked at the problems associated with introducing an artificial cloud within a wind tunnel. Wells and Bragg (1992) performed a 2-D computational study to examine the effect of wind tunnel walls on droplet trajectories impinging upon an airfoil model. This study compared flowfield and droplet trajectory calculations for an airfoil with wind tunnel walls to no-wall calculations and showed that the far-field upwash and near-field downwash effects canceled and resulted in similar water droplet collections on the airfoil. Khodadoust and Bragg (1994) examined the 2-D effect of a wind tunnel contraction on an artificial icing cloud. They found that the aerodynamics introduced by the contraction acted as a droplet size sorting device (moving larger droplets towards the center of the wind tunnel) and tended to contract the overall cloud significantly.

The 3-D code selected for the flowfield calculations was VSAERO. This code is documented by Maskew (1982, 1987). It is a low-order panel method that includes wake and boundary layer modelling. This code was modified and extended from its original use as an external flow solver to more general use that includes internal flows. The use of VSAERO for internal flows is described for several applications by Ashby and Sandlin (1986), Nathman and Frank (1987), and Carlin and Bevan (1987).

The computer code ICE was selected for the calculation of the water droplet trajectories for this effort. ICE was documented by Nathman (1992). ICE was selected for use in this effort because it is closely coupled with VSAERO. ICE relies on both the VSAERO aerodynamic solution and geometry definition in the form of the VSAERO plotfile.

A database of experimental results was required for the validation of the trajectory calculation technique utilized for this effort. Due to the lack of good analytical tools until recent years, a great deal of work had been performed to experimentally determine the water impingement characteristics on various aerodynamic surfaces. During the NACA icing program, a technique was developed to quantitatively measure the water impinging upon aerodynamic surfaces. This technique was utilized by Dorsch and Saper

5

(1955) to study the impingement characteristics associated with spheres. Gelder, Smyers, and von Glahn (1956) used the same techniques for quantifying the water droplet impingement on 2-D airfoil sections. Lewis and Ruggeri (1957) then looked at water impingement on bodies of revolution. The NACA technique was modernized (Papadakis et al., 1989) to allow faster, more repeatable results. This technique was used by Kim (1986) for comparisons to his trajectory calculations.

Additional validation and basic droplet drag data was obtained by reviewing reports dealing with the terminal velocities of small spheres. Prupaccher and Klett (1980) describe the properties of droplets in their discussion of clouds and various forms of precipitation. This data is based upon detailed study of the drag of droplets which was determined by first measuring their terminal velocities (Davies, 1945)(Gunn and Kinzer, 1949)(Beard and Pruppacher, 1969)(Beard, 1976).

A quantitative description of the NASA Lewis Research Center's Icing Research Tunnel (IRT) (Addy, 1993) was required to provide a geometry description required by VSAERO. To validate the results of the flowfield generated by VSAERO a database was required based upon aerodynamic measurements made by Addy and Keith (1989, 1990, and 1992) and Arrington et al. (1992 and 1994).

1.4 Scope of Work

After reviewing the literature available regarding the trajectories of droplets with wind tunnels it became apparent that a computational effort would be most appropriate to quantify the effects of water droplet trajectories within the IRT. To date no 3-D computational effort had been undertaken for this kind of problem, however, 2-D techniques had been undertaken and appeared to be applicable to the 3-D flowfield of the IRT. A purely experimental effort would be very costly and take away testing time from other important projects.

The computer codes VSAERO and ICE were selected for this effort. As discussed above, VSAERO had been utilized for prior internal flow studies of wind tunnels and exhibited good agreement to experimental results. Also, VSAERO is complimented by an excellent visualization code, OMNI3D, that is very useful in interpreting the aerodynamic data produced by the flowfield solver. ICE utilizes the same plot file format as VSAERO. This plot file is how ICE obtains both the aerodynamic and geometry information produced by VSAERO and is also how the trajectory information is presented for 3-D visualization by OMNI3D. VSAERO was available to the author in an executable only

format. ICE was available in a source code form.

No detailed evaluations of the ICE code have been performed in the past. To validate the ICE code for use in this investigation of the trajectories in the IRT several studies were required. A generic study was required to establish the proper values for several variables used by the code and to establish the overall accuracy of the code. Then an IRT wind tunnel test was required to establish the accuracy of the code for that specific configuration. Since no appropriate data existed, an experiment was performed in the IRT to support this study. Comparison to the experimental data lead to the modification of the ICE code to correct several inaccuracies.

Following the evaluation of the codes the primary goal of a computational study of the trajectories within the IRT was performed. Of particular interest was the influence of the wind tunnel contraction upon the droplet cloud size distribution and liquid water content distribution across the test section from that at the inlet and the influence of the wind tunnel walls upon the impingement characteristics of a wing model.

CHAPTER II

DROPLET TRAJECTORY EXPERIMENT

2.1 Test Objective

An experiment was required to gain an understanding of
the water droplet trajectory behavior within the NASA Lewis
Research Center Icing Research Tunnel (IRT) and to validate
the calculations of droplet trajectories within the IRT.
This experiment required testing within the IRT to ensure
the appropriate flow conditions. The test also required a
special spray delivery system. The standard IRT spray
system produces a broad cloud of calibrated droplets that
nearly fills the entire test section. However, icing
prediction computer codes simulate the icing process by
calculating individual droplet trajectories one at a time.
In order to produce data that could be compared to the
computer codes, it was decided that this test should require

9

a special spray system that could provide more of a point source of calibrated water droplets that could be moved about the normal spray bar plane. The test would examine the water droplet trajectories based upon various release locations and two droplet size distributions.

2.2 Background

To satisfy the requirement for a moveable single droplet source, it was decided to use a single spray nozzle. Before this effort, no test in recent memory had been conducted in the IRT with a single spray nozzle.

Olsen (as reported by Ide, 1990) had run the horizontal spray bars individually and had also run vertical columns of spray nozzles in order to gain an understanding of the causes of any IRT icing cloud non-uniformity. This Olsen data would later prove valuable to this effort to help define the level of experimental accuracy.

In an effort to experimentally measure water droplet impingement efficiencies on aerodynamic surfaces a special spray system was developed by a NASA/FAA/Wichita State University/Boeing team (Papadakis, 1989). This spray system consisted of a water tank, twelve spray nozzles, fast action

solenoid valves, and connecting hoses. This system sprayed
a dye solution which allowed the documentation of the
location and intensity of water impingement upon the
aerodynamic surfaces being examined. A portion of this
spray system was utilized for the current effort. To
provide a single, moveable source, only one spray nozzle was
used. This reduction from twelve nozzles to one greatly
simplified the system and reduced the number of hoses and
solenoid valves accordingly.

2.3 Hardware Description

The most important hardware used during this test was
the spray system assembly (Figures 2.1 and 2.2) described
above. This spray system was utilized in place of the IRT
system to allow: 1.) the use of dyed water to document the
spray impingement location, and 2.) to allow relatively easy
movement of the nozzle. The nozzle used for this test was a
NASA Lewis Standard Icing Spray Nozzle. Blue food coloring
dye was mixed with demineralized water for use in the spray
system. Pressures in the water tank and air lines were
independently controlled to set the desired spray water
droplet size. The nozzle mount assembly permitted
attachment to the existing IRT spray bars in the settling

11

chamber just upstream of the contraction. This mounting system allowed for relatively easy movement of the spray nozzle between runs.

The test article in the IRT test section was the Brass Test Section Grid (Figure 2.3). Blotter paper was clipped to the grid to allow the detection and measurement of the impingement region of the dyed water (Figure 2.4). The data gathered is used to compare to empty test section computational data and since the grid's bar stock is placed edge-on to the flow this is seen as a valid assumption.

The NASA Lewis ESCORT data acquisition system was utilized to record tunnel conditions and spray system pressures. The spray nozzle location was measured after each nozzle move and the blotter strips (which recorded the spray impingement) were measured as they were removed from the grid.

2.4 Test Techniques

A calibrated spray was produced by first adjusting the pressures to the air and water supplies to the nozzle, then activating a solenoid valve quickly opening the water supply line. The desired pressures were determined from the

Standard Nozzle calibration based upon two droplet size distributions. The values used were: 1.) P_{air}= 551.5 kPa (80 psig), P_{water}*= 689.5 kPa (100 psig) for an Mean Volumetric Diameter (MVD) of 16.45 microns and 2.) P_{air}= 448 kPa (65 psig), P_{water}*= 689.5 kPa (100 psig) for a MVD=20.36 microns (* Note: the P_{water} was adjusted from run to run to account for head loss due to nozzle height).

Tunnel airspeed was held at 67 m/s (150 MPH) for all runs. Minimal refrigeration was used to prevent over heating of the fan drive system since the formation of ice was not desired.

The spray times were varied depending upon the density of the dye impinging the blotter strips. Therefore, comparisons of resultant dye density between runs is not appropriate.

2.5 Data Analysis

To determine spray density, a guideline was developed for visually examining the blotter strips for dye concentrations. If no dye was visible, a concentration level of 0 was assigned to the strip (Figure 2.5). A trace of dye indicates a concentration level of 1. A well defined

13

line of dye is assigned a level of 2 (upper edge of Figure 2.6) and a saturated line is assigned as level 3 (lower edge of Figure 2.6). If the dyed water ran back from the impingement region in well defined rivulets, then a concentration level of 4 was assigned (right edge of Figure 2.7). And if the run back was so great so that the rivulets blurred together, then a concentration level of 5 was assigned (center of Figure 2.7).

After a numerical concentration value was assigned to a given location on the grid, the data was processed with a contour plotting package. The resulting plots are shown in Figures 2.8 through 2.15. The point of highest concentration on each plot was defined as the center of impingement for that particular spray. Table I shows a summary of the spray runs. Listed are the time, nozzle location, spray impingement center on the brass grid, and MVD for each spray.

Due to time constraints during the testing, the repeatability of the data was not established. To gain an understanding of the repeatability and accuracy of this test, data from a prior test were reviewed. As discussed above, a series of tests were conducted by Olsen to establish a method to improve the cloud uniformity in the IRT. This data is shown in Figure 2.16 and represents the

spray bar (vertically 1 through 8) and nozzle location (horizontally 1 through 51) required for water droplets that pass through a specific point in the wind tunnel test section. A direct comparison of this data to the recent experiment is possible with the dimensions of the nozzle locations and the assumption that the sprays from the two tests are equivalent. The 8 spray bars are spaced 0.61 m (24 in) apart starting at 1.82 m (71.5 in) from the floor, and the 51 nozzles are spaced 0.15 m (6 in) apart starting 0.37 m (14.75 in) from the south wall. The Olsen test used a 20 micron MVD droplet cloud produced with the IRT standard nozzles. The recent test used a single IRT standard nozzle spraying a 21.5 micron MVD cloud. The difference in trajectory paths due to these two different MVDs was calculated to be less than 0.003 m (0.01 ft) and is considered negligible.

Table II presents the comparison between the Olsen data and the recent experimental results. The comparison for the first two rows of data was thrown out because these points fell outside of the bounded region of the Olsen data. The error band that will be used for the experimental data is the maximum difference between the two experimental datasets, 0.2 m (0.7 ft).

2.6 Results

Two significant effects appear upon close examination of this experimental data. The effect first is that the location of the release point influences the spacing of the trajectories in the test section. The second effect indicates the presence of large boundary layers on the walls, floor, and ceiling in the wind tunnel upstream of the test section contraction. Small effects caused by droplet size variation and flow asymmetry are also seen. However, variations from these last two effects are within the experimental error band discussed above, and must therefore be considered insignificant.

2.6.1 Release location effects

The x-direction and y-direction release points and test section impingement centers are plotted against each other in Figures 2.17 and 2.18. The slope from both of these figures was then plotted against the release point distance from the wind tunnel corner (Figure 2.19). Apparent in this figure is that as the release point approaches the center of the tunnel the spacing between the trajectories shown becomes greater. This is a significant point, since it shows that an evenly distributed array of nozzles upstream

of the contraction will result in an uneven cloud in the
test section. Currently the IRT spray bars are evenly
spaced in the vertical direction. The results of this test
suggest that the spray bar spacings should vary with
distance from the tunnel centerline. To aid in the
improvement of IRT cloud uniformity the spray bars near the
floor, ceiling, and walls should be spaced further apart
than at the tunnel centerline. This trend is even more
obvious in the horizontal direction. The horizontal spray
bars currently have evenly spaced nozzle locations. This
may need to be altered in a manner similar to the spray bar
spacing, with more possible nozzle locations installed near
the centerline of the tunnel.

2.6.2 Corner effects

While examining Figures 2.8 through 2.15 another
interesting effect appears. In the plots representing the
trajectories that ended near the corners (in particular,
runs 2, 4, 5, 6, and 7 seen in Figures 2.8, 2.9, 2.10, and
2.11) interesting impingement patterns emerge. Instead of
the expected single point of highest dye concentration
tapering down to nothing in all directions, these runs
display areas of higher dye concentration that pull out
along the walls. This effect is seen to be caused by

interaction between the spray and the wind tunnel boundary layer. It is theorized, based upon this data, that upstream of the test section contraction, in the area of the spray bars, a thick boundary layer exists. When the spray encounters the boundary layer it is able to diffuse further into the region of decelerated flow within the boundary layer than it can outside the boundary layer. This would explain the impingement patterns displayed for the runs listed above.

CHAPTER III

DROPLET TRAJECTORY COMPUTATION

3.1 VSAERO program calculation approach

VSAERO is a first order three-dimensional potential flow
panel code that uses quadrilateral panels of constant doublet
and source distributions (Maskew, 1982). Its approach is
somewhat unique in that it solves for a fictitious internal
Dirichlet boundary condition in addition to the physical
Neumann boundary condition. This results in the solution of
a scalar velocity potential instead of the velocity vector.
Since the velocity is the gradient of the potential, the
potential formulation used by VSAERO behaves as if it is one
order higher than would a direct velocity solution, in other
words it behaves like a second order panel code. The
disadvantage of this formulation is that numerical
differentiation must be performed upon the solution to
provide a velocity distribution. This requires careful
panelling to prevent numerical errors.

19

3.2 ICE program calculation approach

The ICE program calculates the water collection efficiency (Beta) of an arbitrary three-dimensional (3-D) geometry. This calculation is an important first step in the prediction of ice growth on an aerodynamic surface as it calculates the amount of water impinging on each panel of the 3-D surface. The basic technique used by ICE is to search for the trajectories that hit each of the four corners of a particular panel of interest. The Beta for this panel is then the freestream area defined by these four trajectories divided by the panel area on the surface (Figure 3.1). This procedure is then performed for each panel within the region of interest on the 3-D body. The derivation of the equations of motion used by ICE is presented in Appendix A.

3.3 VSAERO accuracy study (sphere)

The solution for a purely potential flowfield about a sphere was calculated with VSAERO for comparison to an analytical solution provided by Dorsch et al, 1955. The analytical solutions are given in cylindrical coordinates as:

$$u_z = 1 - 1/2 * (2z^2 - r^2)/(z^2 + r^2)^{5/2}$$

and

$$u_r = -3/2 * (zr)/(z^2 + r^2)^{5/2}$$

Three levels of panel refinement were run (300, 600, and 1200 panels) for a reflected 1/2 model representation of a 0.23 m (9 in) radius sphere (for an effective panel resolution of 600, 1200, and 2400 panels). As would be expected, the 1200 panel model provided the lowest level of error, followed by the 600 panel model, with the 300 panel model the least accurate (Figures 3.2-3.4). Calculation time for these cases increased roughly linearly with the increase in panels. However, the improvement from 600 to 1200 panels was only about one quarter that seen in going from 300 to 600 panels. The maximum error for the 600 panel model was $0.015 * V_{ref}$ which was deemed reasonable and this solution was used for later studies.

3.4 Summary of Parameter Study Findings

A detailed description of the parameter studies performed is presented in Appendix C. Following is a brief summary of the results of those studies.

1.) For accurate comparison to experimental results, the use of a droplet distribution is preferred over the use of a single droplet size despite the greater computation time required.

2.) Trajectory length did not appear to influence the accuracy of the velocity calculations or the trajectory accuracy.

3.) The greater the resolution of the velocity grid, the more accurate the droplet trajectory. However, the VSAERO time increases exponentially with the refinement in a single grid resolution. For the test geometry, a reasonable grid resolution was found to be 0.006 m (0.02 ft) for all three directions.

4.) Droplet size does have a significant influence of the accuracy of the trajectories. A small droplet's trajectory will have a less accurate trajectory than will that of a large droplet for a given grid resolution.

5.) As minimum step size is decreased the accuracy of the trajectory increases. However, the computation time also increases. The minimum step size of 0.025 was found to yield reasonable accuracies without sharply increasing computation time.

3.5 Terminal velocity of droplets falling in stagnant air

To examine the accuracy of the trajectory calculations in the regime were Reynolds numbers are very small and gravity is active the terminal velocity of droplets in stagnant air was studied.

This case is particularly interesting because it examines a regime very different from normal trajectory calculations. Normally gravity is inactive or if active is quite negligible, the flowfield dominates the droplet path, and the Reynolds numbers have a moderate value. For falling droplets in stagnant air the opposite is true, as the gravity is the driving force that must be balanced by buoyancy and drag, the flowfield is non-existent, and Reynolds numbers are very small.

Several modifications were made to the code to extend its capability to the falling droplet case. First, the minimum Reynolds number was lowered to 0.00001 since values this low are approached for free-falling small droplets. Second, since the droplets are released at rest, time step length determination was decoupled from the droplet velocity. Third, a minimum droplet velocity check was lowered. And finally, the velocity interpolation routine was replaced with one that returned a zero velocity for all points.

Calculations were made for a range of droplets sized from 2.5 to 40 microns that were released in stagnant air. The trajectories calculated showed the droplets accelerate from rest to a stable terminal velocity. These values were recorded and are shown plotted versus experimental data (Pruppacher and Klett, 1980) in Figure 3.5. The agreement between the calculated and the experimental data is excellent. The quality of the calculations is very encouraging and shows that the relationships between drag, droplet velocity, gravity, and buoyancy are modelled accurately in ICE.

3.6 Collection Efficiency on a Sphere

A set of calculations was undertaken to examine the overall accuracy of VSAERO/ICE to calculate the collection efficiency on a body. The geometry for these calculations was the one used above, the 0.23 m (9 in) radius sphere. The NACA experimental data was obtained with four droplet size distributions with MVDs of 11.5, 14.7, 16.7, and 18.6 microns.

To model this geometry several VSAERO runs were made. The first VSAERO run consisted of three viscous/potential flow iterations to determine the boundary layer separation

point. For the second VSAERO run, wake panels were attached to the sphere model just aft of the point where the first run predicted boundary layer separation. Three wake relaxation iterations were performed followed by another three viscous/potential iterations. Due to the presence of the wake panels, the boundary layer separated one panel upstream of the prior prediction. The third VSAERO run was made with the new wake attachment point with three wake relaxation iteration followed by three viscous/potential iterations. Since the predicted boundary layer separation point was less than one panel away from the wake attachment point, the solution from this run was accepted. After a valid aerodynamic solution was obtained VSAERO calculated off-body velocities within a grid whose spacing was determined using the knowledge gained during the parameter studies discussed above. The grid used was 175 by 50 by 25 which yielded approximately a 0.006 m (0.02 ft) spacing in all directions.

Several runs were executed with ICE using the velocities generated by VSAERO. As a check ICE was also run with the analytical velocity solution. The results of these runs are displayed in Figures 3.6, 3.7, and 3.8. Figures 3.6 and 3.7 show the local water collection efficiencies versus the non-dimensional surface distance (surface distance from the stagnation point divided by the sphere's radius) for droplet distributions of 11.5, 14.7, 16.7, and 18.6 microns (the droplet distributions were approximated with the seven bin

Langmuir-D distributions discussed above). Also plotted is the NACA experimental data (Lewis and Ruggeri, 1957).

An area of concern that appears when looking at this data is the drop in local collection efficiency as the stagnation point is approached. To address this concern several cases were run using the analytical potential velocity solution instead of the values from VSAERO. This data is shown in Figure 3.8. Due to the use of a pure potential flow solution instead of one that included wakes and boundary layers, the calculated collection efficiencies curves were shifted down. However, more importantly, the drop near the stagnation point is no longer present. Therefore, one may assume that the drop seen in the calculations using VSAERO velocities is due to an error in the VSAERO values. One should also note that the panels near the stagnation point of the sphere were very small and that they were not rectangular, but quite triangular in shape (Figure 3.9). This panel configuration would lead to errors in the calculation of the velocities in this region, and these velocity errors would in turn lead to errors in the calculated local water collection efficiencies. One should note, however, that this is quite a severe test of the codes, and that normal wing shaped surfaces would not produce these small triangular shaped panels.

The overall agreement between the calculated values and the experimental data is quite good for the 11.5 and 14.7 micron cases, but gets progressively worse for the 16.7 and the 18.6 micron cases. A possible explanation for this is the selection of the droplet distribution for the calculations. As discussed above, the water droplet distribution selected for use in the code can significantly influence the final results. In an attempt to improve the results for the larger droplet sizes, the calculations were repeated with an alternate droplet size distribution. The distributions used for these repeat runs were determined by Papadakis, 1989 for his experimental effort. His two distributions were for MVDs of 16.448 and 20.362 microns. These distributions were applied to the 16.7 and the 18.6 micron cases respectively. The seven bin distributions used are shown in Table IV.

Figure 3.10 shows the significant improvement in collection efficiency accuracy using the Papadakis droplet distribution over the Langmuir-D distribution.

When one considers that the error of the experimental maximum local impingement efficiency varies from 10 to 25 percent (Gelder et al., 1956), the overall agreement between the experimental NACA data and the VSAERO/ICE calculations must be considered to be quite good.

3.7 Flowfield calculation in IRT

Modeling of the IRT was accomplished using VSAERO's
capability for internal flow calculations. To perform this
calculation, the flow duct must be accurately modelled to
ensure no "leakage" and the inlet and outlet flow normal
velocities must be set. The geometry for these VSAERO runs
(figure 3.11) was produced using an algorithm (Addy, 1992 and
1993) based on the IRT blue prints. To produce computational
solutions appropriate for comparison to IRT experimental
measurements, proper inlet and boundary layer conditions were
required. The model inlet was defined as the IRT's spray bar
plane. A map of the flow field measured with a hand-held
anemometer (Arrington et al., 1992 and 1994) was used to
define the inlet velocity conditions. Based upon this
velocity data and also qualitative information from personnel
involved with the facility, it appears that the boundary
layer in the wind tunnel settling chamber is quite thick. A
discernable velocity deficit is apparent as far as 1.5 m (5
ft) from the wind tunnel floor and ceiling. This knowledge
along with the assumption that the boundary layer was
turbulent allowed the setting of the initial boundary layer
conditions for VSAERO. A plot of the _ and _* for the
boundary layer along streamlines is presented in figure 3.12.
It should be noted that the value of _ is not physically
representative, since the boundary layers on the different
surfaces are likely merging. However, the resultant _* and

28

the velocity profile appear realistic based upon the available information.

3.8 Requirements for calculation of trajectories in IRT

The water droplet trajectories within the IRT were calculated in a manner similar to those about the sphere discussed earlier. A three-dimensional grid of velocities was calculated by VSAERO and stored within the flowfield output file. This flowfield data was then accessed by ICE.

The optimal velocity grid spacing for the spherical geometry discussed above was 0.6 m (0.2 ft). Over a distance equal to the radius of the sphere, 0.23 m (9 in), the velocity increases from 0 to 1.5 V_∞. This results in a non-dimensional velocity change of 0.04 per grid cell. The velocity grid spacing used in the IRT calculations was 0.06 m (0.2 ft). The flowfield accelerates from roughly 0.1 to 1.0 V_∞ through the contraction over approximately 9.1 m (30 ft). This results in a non-dimensional velocity change of less than 0.01 per grid cell. This IRT velocity grid resolution was therefore decided to be more than adequate.

To simplify the trajectory calculations, an assumption was made that the trajectory path of a single droplet with

the size of the cloud's MVD would impact at the site of maximum water impingement from the cloud itself. This assumption was validated when the mass weight-average of the distribution's test section location was compared to that of a droplet with the distributions mean volumetric diameter. This is shown in the Table V.

CHAPTER IV

COMPARISON BETWEEN EXPERIMENT AND COMPUTATION

4.1 Comparison of calculated trajectories to experimental data

Water droplet trajectories were calculated using the IRT geometry and the droplet size information and release points from the experimental effort. These calculations were made by releasing the droplets within the plane of the spray bars and tracing the trajectories until they reached the plane of the center of the test section. This data and the corresponding experimental values are presented in Table VI.

Trajectories were also calculated for the release point of Y=3.04 m (9.98 ft) and Z=-2.57 m (-8.44 ft). These calculations were rejected for two reasons. The first problem with these trajectories is that they should be

passing through a significant portion of the boundary layer. However, VSAERO handles boundary layers by displacing the surface streamlines with surface normal transpiration, so the velocities in the near-wall region will not be physically representative. The second problem with trajectories that pass very close to the wall is the accuracy of the velocity solution due to proximity of the panel edges. Disregarding the presence of the boundary layer, to properly perform this calculation a more finely resolved panelling would be required in the region of the contraction.

Experimental data was also gathered to examine the asymmetry of trajectories from the north-side to the south-side and the top-half to the bottom-half of the wind tunnel. These cases did not show any asymmetry greater than the experimental error band. Because of this, these trajectories were not calculated.

The agreement between the experimental and computational values appears very good. The difference between these values is less than the experimental error, 0.2 m (0.7 ft), discussed above. Based upon these results, the VSAERO/ICE model of the flowfield and resultant water droplets trajectories within the IRT are judged to be more than adequate for this effort.

4.2 Examination of tunnel contraction influence on trajectories

4.2.1 Program Inputs

While the inlet and boundary layer values discussed above produced good agreement with the experimental data and likely describe the current flowfield within the IRT, it was decided that a uniform inlet and no boundary layers would be used for the remaining studies. These assumptions remove the peculiarities of the existing IRT flowfield from the examinations and provide a more idealized flow environment for the studies.

VSAERO was run with the uniform inlet non-dimensional blowing velocity set to provide a test section non-dimensional velocity of 1.0. With this flowfield solution in hand, ICE was run to predict the water droplet trajectories for droplet sizes ranging from 5.539 microns to 65.084 microns and test section velocity of 67 m/s (150 mph). The droplet size distribution used was the seven bin distribution for a 20.0 micron spray from a NASA standard icing nozzle that was discussed earlier. The droplets were released in a square grid pattern with a 0.3 m (1 ft) spacing.

4.2.2 Results

Figure 4.1 shows the wind tunnel with calculated droplet trajectories from the spray bar plane through the test section. By examination of this figure, one can gain a sense of the very large influence the wind tunnel contraction has upon the water droplet trajectories. To examine this influence, the analysis methodology developed by Khodadoust and Bragg (1994) was employed. The water concentration in the test section was calculated for each droplet size by dividing the upstream area defined by four adjoining trajectories $(0.09 \text{ m}^2 (1 \text{ ft}^2))$ by the similar area at the test section center. To obtain an idea of the water mass distribution, this value was then divided by the tunnel's area contraction, 14.13255. The resultant concentration (or relative LWC) for each droplet size across the test section are shown in Figures 4.2 through 4.8 (these and following plots represent a quarter of the test section with the center of the coordinate system located at the tunnel centerline). At this point the water concentrations have not been weighted by the droplet size distribution. For comparison, the relative LWC for droplets not influenced by the wind tunnel walls would be 1.0. With that in mind, one can see that as the droplet size increases the droplets are forced closer towards the center of the tunnel,

increasing the relative LWC there. To maintain a mass balance, this also indicates that the outer boundary of the droplet cloud contracts with increasing droplet size.

Due to the influence of the tunnel contraction, the distribution of water as a function of droplet size varies across the test section. This is shown in Figure 4.9 which plots the water concentration distribution at the point closest to the wind tunnel center, the center of the region of interest, and the point furthest from the wind tunnel center. For comparison, the NASA standard nozzle distribution is also plotted. The area under these distributions represents the total amount of water present at the respective test section location. A plot of the total water distribution (effective LWC) is shown in Figure 4.10. Within the area of interest examined here, the effective LWC is seen to vary by approximately +/-7.5 percent.

To examine the variation of MVD across the test section, it is first required that the water concentration distribution seen in Figure 4.9 be non-dimensionalized by the effective LWC for each point in space. This results in the water concentration distributions seen in Figure 4.11. These distributions are for the same locations examined in Figure 4.9. For the entire region of interest, the

calculated water concentration distributions are seen to vary from that of the NASA standard nozzle, which indicates that the MVD will in fact be influenced.

To calculate the MVD at a given location, the cumulative LWC as a function of droplet size must first be determined. This is shown in Figure 4.12. The MVD is then determined by finding the droplet size at the 50 percent point of the cumulative LWC curve. The plot of the resultant effective MVD distribution is shown in Figure 4.13. Since the spray bar plane droplet distribution represented a 20.0 micron MVD, the test section MVD was raised by 0.35 microns near the tunnel center and by 0.45 near the outer edge of the area examined. This increase in MVD is due to the increase in the number of large droplets in this region as seen earlier. A related decrease in MVD would be expected near the test section walls due to the decrease in the number of large droplets in that region.

This series of calculations was also carried out for a test section velocity of 134 m/s (300 mph). The results from these calculations are shown in Figures 4.14 through 4.25. As would be expected, the droplet cloud continues to contract as the wind tunnel velocity is increased. Within the area of interest, the effective LWC for this tunnel condition is seen to vary by approximately -7 and +10

percent. And the MVD is elevated by between 0.45 and 0.7 microns from the initial value of 20.0 microns.

4.3 Examination of tunnel wall influence on trajectories

Similar inlet conditions were utilized for the calculations that included a model in the test section. The model panelled was a section of DeHavilland Twin Otter wing spanning the wind tunnel test section from floor to ceiling. The actual wind tunnel model was constructed from a piece of aircraft wing, so it is quite large with respect to the IRT's test section area, 2.0 m (78 in) chord with a 16 percent thickness. Specific care must be exercised when including a model in the wind tunnel paneling to ensure panel matching and ensure no "leaks" develop that would influence the aerodynamic solution.

Figures 4.26 through 4.29 show the calculated pressure distributions about the Twin Otter wing installed in the IRT test section for 0 and 4 degrees angle of attack. Figures 4.30 through 4.32 show similar results for the Twin Otter wing with no wind tunnel walls and a span of 12.2 m (40 ft). By comparing the 2-D plots it becomes obvious that the pressure distribution about the Twin Otter wing is significantly influenced by the presence of the wind tunnel

wall. As would be expected, this influence increases as the model's angle of attack is increased. A simple 2-D wall correction calculation was completed using a technique described by Rae and Pope (1984) to correct the lift calculated for the installed wing. When compared to the calculated lift for the isolated wing the error was only 3.3%.

The water droplet collection efficiency (beta) was calculated with ICE for these geometries. The first cases to be examined were the installed and isolated wing at four degrees angle of attack. Figure 4.33 shows the results for a 20 micron MVD droplet distribution when the droplets were released at station X=2.3 m (7.7 ft) (which represents the spray bar plane in the IRT). Because the installed droplets are originating in the settling chamber, the betas for this case were corrected by the wind tunnel contraction ratio, 14.13. Overall, the two curves agree well, with the maximum beta and the impingement limits agreeing very well and only a slight dip for the installed wing just below the maximum beta point. Figure 4.34 shows the collection efficiency curves for a monodisperse 20 micron cloud with release points at stations X=2.3 m (7.7 ft) and X=13.4 m (44.0 ft) (which represents the test section inlet in the IRT). Here, agreement is still good. However, the upper impingement limit appears to be different by one or two panels between

the installed and isolated wing cases. Also, the dip just

below the maximum beta for the installed wing appears more

evident. Figure 4.35 shows the collection efficiency curves

for a monodisperse 40 micron cloud with release points at

stations X= 2.3 m (7.7 ft) and X=13.4 m (44.0 ft).

Agreement between all four curves appears very good. The

improved agreement for this case makes sense since the more

massive droplets with a higher mass inertia are influenced

less by the flowfield than for the 20 micron case.

The agreement demonstrated between the installed and

isolated wing cases is very interesting considering the

difference seen in the pressure distributions for the two

geometries. Even more interesting is the level of agreement

when the trajectories themselves are observed. Figures 4.36

show the impingement limit trajectories for the two

geometries at 4 degrees angle of attack with a 20 micron

droplet cloud. The effect of the wind tunnel contraction

upon the installed wing's trajectories is very evident in

the region up roughly X=12.2 m (40 ft). The differences

beyond this point are due to straight-wall effects. Figure

4.37 shows a close-up of the final part of these

trajectories. The trajectories are seen to merge as they

enter the last 0.15 m (0.5 ft) before impact on the wing

surface. Both the beta curve agreement and the trajectory

merging were also observed by Wells and Bragg (1992). They

39

concluded that the far-field and near-field upwash effects canceled. The near-field (less than 1/10 chordlength ahead of the model) upwash increases as the wind tunnel walls are brought closer to the model and the far-field (greater than one chordlength ahead of the model) upwash decreases as the walls are brought closer. The Wells/Bragg results were for long parallel walls, so it is very significant that the trends hold true for this IRT data since the IRT contraction ends just one chordlength ahead of the Twin Otter wing model.

The velocities encountered by a droplet along its trajectory are shown in Figures 4.38 (isolated wing) and 4.39 (installed wing). These plots proved to be a valuable diagnostic tool in determining the quality of the trajectory solutions. An adequate grid resolution would result in smooth gradients along a droplet trajectory while a poorly resolved grid would result in visible, discrete steps. The velocity curves are quite smooth for the majority of the trajectory for both cases. This confirms that the grid was adequately refined. However, the curves become fairly bumpy near the model for the installed wing case. This bumpiness in the velocity curves is not caused by grid resolution, but rather by the close proximity to the wing panel edges in that region. It should be noted that the particle trajectories in Figures 4.38 and 4.39 were not visibly

influenced by this level of variation in velocities, nor were the final collection efficiency plots adversely influenced.

Figure 4.40 shows the water droplet collection efficiency curves calculated for the isolated and installed wing at zero degrees angle of attack with a 20 micron MVD droplet cloud distribution. The lower impingement limits for the two curves match and the upper limits are within one panel width. The shape of the two curves are close except for the higher maximum beta for the installed wing case. Figure 4.41 shows the beta curves for a monodisperse 20 micron cloud with release points at stations X=2.3 m (7.7 ft) and X=13.4 m (44.0 ft). Again, the lower limits match, the maximum beta for the installed wing is higher than for the isolated wing, and the upper limits are greater for the installed wing than for the isolated wing. The maximum beta for the installed wing was checked by calculating the collection efficiency with an array of droplets released at evenly spaced points. The resultant curve is shown in Figure 4.42. Since the maximum beta seen in Figure 4.42 is very close to those in Figures 4.40 and 4.41, the beta calculation technique used by ICE is seen to be correct. The spike in these curves is likely due to inadequate panel resolution at this point which influenced calculation of the off-body velocity. The difference in the curves near the

upper impingement limit is again likely tied to panel resolution. As discussed above, error is introduced to the particle trajectory as it passes near panel edges. Due to the Twin Otter wing geometry, at zero degrees angle of attack, droplets are skimming the wing's forward-facing upper surface. This means that the droplet trajectories are passing very close to several panel edges. The error in the calculated trajectories is also increased since the panels in this region are larger than those near the stagnation point. Also, due to wall effects the velocities in this region are greater for the installed wing than for the isolated wing, and this will amplify any velocity error. While the errors that arose in these calculation do not make it the best validation candidate, the results for the zero degree cases do support the findings from the four degree cases.

CHAPTER V

CONCLUSIONS

The VSAERO/ICE code package has been shown to be valuable tool in calculating the trajectories of water droplets and their impingement upon aerodynamic surfaces. Good agreement was found for both aerodynamic and droplet impingement comparisons to experimental data for spheres. Code parameters were studied and adjusted for optimal trajectory performance. The gravity terms in the formulation of ICE were updated to allow good agreements to experimental data for droplets falling in stagnant air. And the droplet trajectories calculated for flow within the NASA Lewis Research Center Icing Research Tunnel (IRT) was found to agree well with experimental data.

The methodology developed by Khodadoust and Bragg (1994) for 2-D analysis of the effects of a wind tunnel contraction upon droplet cloud parameters was extended to 3-

43

D and performed for the IRT. The droplet size distribution and liquid water content was found to vary from the inlet conditions and has been quantified for idealized flow conditions.

The contraction and wall effects upon droplet trajectories and their impingement upon a wing model were examined. The IRT contraction and walls were found to have negligible influence upon the impingement of water droplets upon a wing model despite their significant influence upon the model's pressure distribution. The explanations forwarded by Wells and Bragg (1992) of canceling near-field and far-field upwash effects are accepted for trajectories within the IRT despite the presence of the tunnel contraction.

BIBLIOGRAPHY

Addy, H.E. Jr., personal communication, July 1993.

Addy, H.E. Jr. and Keith, Jr., T.G.,"Investigation of the Diffuser Flow Quality in an Icing Research Wind Tunnel, AIAA Journal of Aircraft, Vol. 29, No. 1, January 1992, pages. 47-51.

Addy, H.E. Jr. and Keith, Jr., T.G.,"A Numerical Simulation of the Flow in the Diffuser of the NASA Lewis Icing Research Tunnel, AIAA 90-0488, January 1990.

Addy, H.E. Jr. and Keith, Jr., T.G.,"Investigation of the Flow in the Diffuser Section of the NASA-Lewis Icing Research Tunnel", AIAA 89-0755, January 1989.

Allaire, Paul E.,_Basics of the Finite Element Method_, Wm. C. Brown Publishers, 1985.

Arrington, E. Allen, Pickett, Mark T., and Sheldon, David W.,"Flow Quality Studies in the NASA Lewis Research Center Icing Research Tunnel", NASA TM-106311, January 1994.

Arrington, E.Allen and Sheldon, David, W., personal communication, February 1992.

Ashby, D.L., and Sandlin, D.R.,"Application of a Low Order Panel Method to Complex Three-Dimensional Internal Flow Problems", NASA CR-177424, September 1986.

Beard, K.V.,"Terminal Velocity and Shape of Cloud and Precipitation Drops Aloft", Journal of the Atmospheric Sciences, Volume 33, 1976, pages 851-864.

Beard, K.V. and Pruppacher, H.R.,"A Determination of the Terminal Velocity and Drag of Small Water Drops by Means of a Wind Tunnel, Journal of the Atmospheric Sciences, Volume 26, 1969, pages 1066-1072.

Borger, G.G.,"The Optimization of Wind Tunnel Contractions for the Subsonic Range", NASA Technical Translation F-16899, March, 1976.

Carlin, G.J. and Bevan,D., "Prediction of Subsonic Wind Tunnel Mounting System Interference",AIAA Journal of Aircraft, Vol. 24, No. 5, May 1987, pages 317-321.

Chmielewski, G.E.,"Boundary-Layer Considerations in the Design of Aerodynamic Contractions", Journal of Aircraft, Volume 11, Number 8, August 1974, pages 435-438.

Coirier, W.J. and Bragg, M.B.,"Computational Method for Screened Two-Dimensional Wind Tunnel Inlets, Journal of Aircraft, Volume 24, Number 4, pages 281-283.

Davies, C.N.,"Definitive Equations for the Fluid Resistance of Spheres", The Proceedings of the Physical Society, Volume 57, Part 4, July 1945, pages 259-270.

Dorsch, Robert, G., Saper, Paul G., and Kadow, Charles F.,"Impingement of Water Droplets on a Sphere", NACA Technical Note 3587, November, 1955.

Farag K.A. and Bragg M.B.,"The Effects of Wind Tunnel Walls on Droplet Trajectories in the Vicinity of a Three Dimensional Wing", AIAA 94-0604, January, 1994.

Gelder, Thomas F., Smyers, William H. Jr., and von Glahn, Uwe, "Experimental Droplet Impingement on Several Two-Dimensional Airfoils with Thickness Ratios of 6 to 16 Percent", NACA Technical Note 3839, December 1956.

Gunn, Ross and Kinzer, Gilbert D., "The Terminal Velocity of Fall for Water Droplets in Stagnant Air", Journal of Meteorology, Volume 6, August 1949, pages 243-248.

Heinrich, A., Ross, R., Zumwalt, G., Provorse, J., Padmanabhan, V., Thompson, J., and Riley, J., Aircraft Icing Handbook, DOT/FAA/CT-88/8-1, March 1991.

Hornbeck, Robert W., Numerical Methods, Quantum Publishers, Inc., 1975.

Ide, Robert F. "Liquid Water Content and Droplet Size Calibration of the NASA Lewis Icing Research Tunnel", NASA TM-102447, AVSCOM TM-89-C-014, AIAA-90-0669, January 1990.

Khodadoust, A., and Bragg, M.B., "A Numerical Study of the Spray Characteristics of the UIUC Subsonic Wind Tunnel", AIAA-94-0603, January, 1994.

Kim, John, J.,"Particle Trajectory Computation on a 3-Dimensional Engine Inlet", NASA CR-175023, DOT-FAA-CT-86-1, January, 1986.

Lewis, J.P. and Ruggeri, R.S., "Experimental Droplet Impingement on Four Bodies of Revolution", NACA TN 4092, 1957.

Maskew, B."Program VSAERO Theory Document: A Computer Program for Calculating Nonlinear Aerodynamic Characteristics of Arbitrary Configurations", NASA CR-4023, September 1987.

Maskew, B.,"Prediction of Subsonic Aerodynamic Characteristics: A Case for Low-Order Panel Methods", AIAA Journal of Aircraft, Vol. 19, No. 2, February 1982, pages 157-163.

Maskew, B."Program VSAERO: A Computer Program for Calculating Nonlinear Aerodynamic Characteristics of Arbitrary Configurations", NASA CR-166476, December 1982.

Mikhail, M.N. and Rainbird, W.J.,"Optimum Design of Wind Tunnel Contractions", AIAA-78-819.

Nathman, J.K.,"ICE Particle Trajectory and Ice Accretion Program, User's Manual, Version 2.0", December 1992.

Nathman, J.K., and Frank, J.H., " Application of VSAERO to Internal Flows", AIAA 87-241, 1987.

Papadakis M., et al.,"An Experimental Method for Measuring Water Droplet Impingement Efficiency on Two- and Three- Dimensional Bodies", NASA CR-4257, November 1989.

Peerless Engineering Service, FORTRAN Scientific Subroutine Library, John Wiley and Sons, 1986.

Pruppacher, Hans R., and Klett, James D., Microphysics of Clouds and Precipitation, D. Reidel Publishing Company, 1980.

Rae, William H. Jr. and Pope, Alan, Low-Speed Wind Tunnel Testing, 2nd edition, John Wiley and Sons, 1984.

Wells, S.L. and Bragg, M.B.,"A Computational Method for Calculating Droplet Trajectories Including the Effects of Wind Tunnel Walls", AIAA 92-0642, January, 1992.

White, Frank M., Viscous Fluid Flow, McGraw-Hill, 1974.

APPENDICES

APPENDIX A

DERIVATION OF ICE EQUATIONS OF MOTION

The droplet trajectory calculation used in ICE (Nathman, 1992) is based upon a derivation of Newton's second law:

$$m \, dV_p/dt = \Sigma F \tag{A1}$$

where,

m	is the droplet mass
V_p	is the droplet's velocity relative to a fixed reference point
ΣF	is the total force on the droplet

The total force acting on the droplet is made up of aerodynamic, buoyancy, and gravity forces.

$$\Sigma F = F_{aero} + F_{buoy} + F_{grav} \tag{A2}$$

Note, that buoyancy and gravity are usually small relative to the aerodynamic forces, and therefore normally neglected.

The aerodynamic force is defined as:

$$F_{aero} = -1/2 \; \rho \; S \; V_{rel}^2 \; C_D)$$
(A3)

where:

ρ is the air density

S is the reference area, $\pi D^2/4$, of the droplet

V_{rel} is the relative velocity between the air and the droplet

C_D is the drag coefficient of the droplet

A plot of C_D versus Re for spheres is shown in Figure A.1 (White, 1974). An empirical fit (White, 1974) for this curve is given by:

$$C_D = 24/Re + 6/(1+\sqrt{(Re)}) + 0.4$$
(A4)

Which is valid within 10% for $0 \leq Re \leq 2*10^5$.

At this point we must recall what we are trying to solve. We want to solve for the trajectory of the water

droplet particle, so what we want to solve for is the particle velocity. To simplify things here, let us temporarily ignore gravity and buoyancy. The fundamental equation is then:

$$m \, dV_p/dt = F_{aero} \qquad (A5)$$

or,

$$dV_p/dt = F_{aero} \, / \, m = - \, 1/2 \, \rho \, S \, V_{rel}^2 \, C_D. \qquad (A6)$$

It is a form of Equation A6 that many water droplet trajectory codes solve. They use numerical integration techniques that can cause problems for droplet sizes below 20 microns. To avoid this problem, ICE utilizes a linearized version of Equation A6 which can be directly solved:

$$dV_{rel}/dt = - \, 1/2 \, \rho \, S \, V_{rel} \, C_{Do} \; - \; dV_{air}/dt \qquad (A7)$$

where,

$$dV_{rel}/dt = dV_p/dt - dV_{air}/dt \qquad (A8)$$

and

$$C_{Do} = V_{rel} \; C_D \tag{A9}$$

this formulation is valid as long as V_{rel} and dV_{air}/dt are relatively constant over the integration step. This is accomplished by limiting Δt to a sufficiently small value. This works to our advantage, since it turns out that a small Δt is required in regions of trajectory curvature, where we would want a small Δt anyway.

Accepting Equations A7 and A8, let us now return to the derivation of the entire equation of motion.

Starting with Equations A2 and A3, and adding:

$$F_{buoy} = - \; \rho \; \pi \; / \; 6 \; D^3 \; g \tag{A10}$$

$$F_{grav} = \rho_{H2O} \; \pi \; / \; 6 \; D^3 \; g \tag{A11}$$

where,

g   is the acceleration of gravity

ρ_{H2O} is the density of water

we obtain:

$$F = - \; 1/2 \; \rho \; \pi \; D^2/4 \; V_{rel} \; C_{Do} + \rho_{H2O} \; \pi/6 \; D^3 \; g - \rho \; \pi/6 \; D^3 \; g \tag{A12}$$

Placing this into Equation A1 results in:

$$dV_p/dt = 1/m \left[-\pi/8 \; \rho \; D^2 \; V_{rel} \; C_{Do} + \pi/6 \; D^3 \; g \; (\rho_{H2O} - \rho) \right]$$

(A13)

Including Equation A8 and bringing m inside the brackets:

$$dV_{rel}/dt = -\pi/8m \; \rho \; D^2 \; C_{Do} \; V_{rel} + \pi/6m \; D^3 \; g \; (\rho_{H2O} - \rho) - dV_{air}/dt$$

(A14)

Rearranging:

$$dV_{rel}/dt + (\pi/8m \; \rho \; D^2 \; C_{Do}) \; V_{rel}$$
$$= (\pi/6 \; D^3 \; \rho_{H2O} \; / \; m) \; g \; (\rho_{H2O}/\rho_{H2O} - \rho/\rho_{H2O}) - dV_{air}/dt$$

(A15)

where,

$$\pi/6 \; D^3 \; \rho_{H2O} \; / \; m = 1$$

Cleaning up:

$$dV_{rel}/dt + k \; V_{rel} = (1 - \rho/\rho_{H2O}) \; g - dV_{air}/dt \qquad \text{(A16)}$$

where,

$$k = \pi/8m \; \rho \; D^2 \; C_{Do}$$

(A17)

Further:

$$dV_{rel}/dt + k\ V_{rel} = C \tag{A18}$$

where,

$$C = (1- \rho/\rho_{H2O})\ g - dV_{air}/dt \tag{A19}$$

C and k are assumed to be constant within any given time step, Δt.

Equation A18 can be readily solved to result in:

$$V_{rel} = A\ e^{-k\Delta t} + C/k \tag{A20}$$

A is found by setting $\Delta t = 0$:

$$V_{rel} = A + C/k\ ,\ @\ \Delta t = 0 \tag{A21}$$

And noting that:

$$V_{rel} = V_{rel,i-1} = V_{p,i-1} - V_{air,i-1}\ ,\ @\ \Delta t = 0 \tag{A22}$$

where the i-1 notation represents the values from the previous time step.

Finally:

$$A = V_{rel,i-1} - C/k \qquad \text{(A23)}$$

APPENDIX B

MODIFICATIONS MADE TO ICE CODE

Gravity term in particle acceleration routine

While reviewing the derivation of the equations of motion described above, it became obvious that there was a problem in the coding. At one point in the routine that calculates the acceleration of the water droplet particle, several terms are summed together:

GZ=-GRAV*RMASS   (gravity acceleration times mass of droplet)

BZ=GRAV*0.1667*PI*(DMICRN*3.28E-06)**3*ROE   (gravity accel times mass of air within droplet volume)

VZT= dV$_{airz}$/dt

FZ=BZ+GZ-VZT

59

This last line of coding is supposed to be the right hand side of Equation A15. To correctly represent the equation, the mass terms were removed and the gravity terms were divided by the reference velocity to match dimensional units. After modifications, the coding should read:

GZ=-GRAV/VREF

BZ=GRAV*ROE/ROEH2O/VREF   (ROE/RHOH2O = ρ / ρ_{H2O})

FZ=BZ+GZ-VZT

This correction has been incorporated into the ICE FORTRAN source coding and has been accepted by the ICE program author.

Beta formula

As discussed above, the ICE program calculates the collection efficiency for a panel by first determining the four trajectories that hit the corners of the panel and then dividing the freestream area between these trajectories by the target panel area. Assuming that the trajectories have in fact hit the panel corners, this is an accurate technique. However, due to computer error, a precise hit of

60

the panel corner is not usually possible. Therefore, a small tolerance value is utilized in ICE to determine a trajectory that is "close enough" to the panel corner to constitute a "hit". A problem arises here for the Beta calculation on small panels. If a relatively large tolerance is utilized to determine the corner trajectories for a relatively small panel, then a large error in the Beta calculated can be expected. This problem was eliminated by modifying the Beta calculation so that the actual trajectory hit points are used to define the area on the surface. The Beta values calculated with this new formula have no error introduced by the selection of the "close enough" tolerance value. Therefore, only inaccuracies in the particle trajectories calculations contribute to the error in the final Beta values.

Search routine for particle release point

The original ICE code utilized a Newton-Raphson technique in the UPDATE routine for determining the release point for trajectories that will result in hitting a specific panel corner. In the use of the program this technique had proven to be quite robust for most cases. However, during the author's study of trajectories in the vicinity of a wing (Figure B.1), a problem arose with this

method. In the region near a wing, one will encounter regions of droplet concentrations due to the trajectories that just miss the wing's leading edge. The Newton-Raphson method often "blew up" when this geometry was studied. This difficulty occurred due to the local distribution of droplets. If a local minimum or maximum or region of zero slope in the droplet distribution is encountered by the method it will most likely fail (Hornbeck,1975). This problem can often be overcome by prior knowledge of the behavior of the function of interest. However, in order to keep the coding robust, it was decided to use a more simple search routine.

In place of the Newton-Raphson method, a bisection method was applied. This simple technique was chosen over more advanced methods in order to keep the technique robust and to minimize coding and debugging time. A complete replacement for the UPDATE routine was written. In this way, either routine may be included in the compiled source code.

Results for the two methods are shown in Figures B.2 through B.5. With all other code parameters held constant, the bisection technique not only was able to calculate the collection efficiencies over the whole region of interest, but the average trajectory calculation was faster. Normally

a Newton-Raphson technique will yield faster results than the bisection technique, but in this case the Newton-Raphson technique resulted in time consuming trajectories far from the region of interest.

APPENDIX C

ICE ACCURACY STUDIES (FOR SPHERE)

C.1 Potential sources for error in calculation of droplet trajectories

The following sources of error were identified for the ICE droplet trajectory program:

1.) Error in calculated velocity: The flowfield velocities used by ICE are generated by VSAERO in grid form, stored in a binary file, then passed to ICE. The accuracy of VSAERO to calculate flowfield velocities was examined above, and is a function of the quality of the body panelling. The values passed to ICE, are then mostly limited by the precision of the computation. The versions of VSAERO and ICE utilized for this effort were single precision. Greater accuracy at the cost of computation time and storage space would be possible by working in double precision.

2.) Error in interpolation of velocity: ICE accepts the flowfield velocities in a grid format and then must interpolate between grid point to calculate the velocity at a given point in a droplet trajectory. This process can produce significant errors if the original grid in too sparse. The error caused by grid density is studied below.

3.) Error caused by large step size: If the time steps in the trajectory calculation are too large significant error will be introduced to the calculation of the trajectory. The error caused by step size is studied below.

4.) Error caused by long trajectories: As the trajectories become longer and longer it is logical that more and more error will be introduced into the computed droplet trajectory. The error caused by trajectory length is studied below.

5.) Error caused by use of improper droplet sizing: The selection of the proper droplet size(s) for the calculation is not trivial. A natural or IRT icing cloud is made up of a continuum of droplet sizes bounded by some statistical envelope. However, the computer can practically only perform the trajectory calculation for several droplet sizes. The resultant error caused by droplet sizing concerns is studied below.

A 0.23 m (9 in) radius sphere was panelled for runs
with VSAERO and ICE to serve as a testbed for the parameter
studies discussed above (Figures C.1-C.4). This is one of
the geometries that was tested by NACA in the mid 1950's
(Lewis and Ruggeri, 1957). This was deemed a good test case
because of the three-dimensional nature of the flowfield,
the simplicity of the geometry, and the availability of the
NACA data.

C.2 Study influence of droplet size distribution versus single droplet size on collection efficiency accuracy

Most water droplet trajectory codes have an option to
calculate the collection efficiencies on a body using either
a single droplet size or a distribution of droplet sizes.
ICE is no exception to this point.

Typically, either a Langmuir distribution or the Mean
Volume Diameter (MVD) are utilized in aircraft icing
calculations. Table III presents the Langmuir
distributions.

Note that distribution "A" is actually a single droplet
size equal to the MVD. An example of a droplet size
distribution would be an MVD of 20 microns using the "B"

distribution:

5% of the LWC is in droplets of 11.2 micron diameter

10% of the LWC is in droplets of 14.4 micron diameter

20% of the LWC is in droplets of 16.8 micron diameter

30% of the LWC is in droplets of 20.0 micron diameter

20% of the LWC is in droplets of 23.4 micron diameter

10% of the LWC is in droplets of 26.4 micron diameter

5% of the LWC is in droplets of 29.8 micron diameter

where,

LWC is the Liquid Water Content with units of grams of water per cubic meter.

The Langmuir "D" distribution is generally accepted as the best distribution for representing a natural icing cloud and an appropriate tunnel cloud droplet size distribution for the IRT (Lewis and Ruggeri, 1957)(Kim, 1986).

Several cases were run to examine the influence of the use of a distribution of drop sizes versus a single droplet size. Figures C.5 and C.6 demonstrate the trends seen in all cases. These figures show the collection efficiency as a function of non-dimensional surface distance around the sphere for the monodispersion (single droplet size) and the Langmuir-D distributions. Figure C.5 shows the computed

collection efficiencies for these two cases and Figure C.6 shows the computation times required. By comparing the two curves in Figure C.5, one can see that there is a significant difference between the two methods. A calculation using only a single droplet size will generally underpredict the collection efficiency near the body's stagnation point and will underpredict the water collection impingement limits. The underprediction of the collection efficiency near the stagnation point is caused by not having the influence of droplets smaller than the MVD and the underprediction of the impingement limits is caused by not having the influence of droplets larger than the MVD. An easy way to visualize the effect of droplet size upon where the droplets will impact a body is to look at the two size extremes. An infinitely small droplet will follow a flow streamline and can only impact the body directly at the body's stagnation point and an infinitely large droplet will not be influenced by the flowfield at all and can impact anywhere on the forward facing surface.

The huge differences seen in computation time in Figure C.6 are caused by performing a much larger number of trajectories for the Langmuir-D distribution. As shown above, seven different droplet sizes were used for the Langmuir-D calculation. Also, since the impingement limits were further aft for the Langmuir-D case, more trajectories

were required for this region. Finally, the smaller droplet sizes included in the Langmuir-D calculations often require more steps (therefore more time) to complete their trajectories. It is this great difference in computation time that often leads the user back to the single droplet size calculation. It should be noted that since the 0.23 m (9 in) radius sphere is a relatively large aerodynamic surface this configuration can be considered to be a worst case. For smaller (and more airfoil-like) surfaces, the difference between the two calculated collection efficiency curves would not be so great.

C.3 Velocity error studies

The following parameter studies look at the errors of particle trajectories due to the errors in the calculated flowfield velocities. The only parameter the user can control to influence the accuracy of the trajectories calculated by ICE for a given configuration is the velocity grid resolution. All other parameters are dependent upon either the flow environment, the icing cloud environment, or the aerodynamic surface.

One reason for choosing a sphere as the test geometry was the availability of an analytical potential flow

solution. ICE was modified to allow the comparison of the flowfield velocities from VSAERO to the analytical values and the comparison of trajectories based upon VSAERO velocities to trajectories based upon analytical velocities. The code was also modified so that the maximum error and the summed error for each velocity component for each trajectory was printed. It should be noted that for these comparisons to the analytical potential solution the sphere was modelled by VSAERO with no boundary layer and no wakes.

C.4 Study influence of grid resolution on trajectory accuracy

Three series of runs were made with a droplet size of 14.7 microns to examine the influence of grid resolution along each of the three axes. The over all grid dimensions used for this exercise were 0.9 m (3.5 ft) in the x-direction, 0.2 m (0.7 ft) in the y-direction, and 0.06 m (0.2 ft) in the z-direction.

Figures C.7, C.8, and C.9 examine the influence of the x-direction grid spacing. Figure C.7 is a plot of the x-direction hit location error. The hit location error is the distance between the hit calculated by the standard VSAERO/ICE package and the hit calculated by ICE using the

analytical velocity solution. As expected, the x-direction hit error is seen to decrease as the grid is more finely resolved. Figure C.8 shows the maximum velocity error as a function of grid resolution. The velocity error is the difference between the interpolated velocity from VSAERO/ICE and the analytical velocity for the same point in x,y,z-space. The maximum velocity error is the greatest error encountered during a droplet trajectory. Figure C.8 shows a general decrease in error as the grid is refined in the x-direction. Figure C.9 shows the calculation time for VSAERO required to obtain the corresponding grid resolution in the x-direction. Note that the grid was kept constant in the y- and z-directions at 25 by 25. Since the computation time is approximately linear with the number of grid points, the computation time increases exponentially as the grid becomes more finely resolved. The jagged form of the two error plots is likely a result of the interpolation scheme used by ICE. The accuracy of the interpolation probably is a function of where the point of interest lies in a given grid cell (ie. near the cell center or boundary).

Figures C.10, C.11, and C.12 examine the influence of the y-direction grid resolution. Figure C.10 shows the hit location error curve, Figure C.11 shows the maximum velocity error curve, and Figure C.12 shows the VSAERO calculation time curve. The x- and z-direction grids were kept constant

at 25 by 25 for this series. The hit error in Figure C.10 seems fairly constant below a delta y value of 0.018 m (0.06 ft). Note that the error is greater in this series than in the prior one. This is due to the x-direction grid resolution of delta x equal to 0.043 m (0.14 ft), which is much more coarse than the range shown in Figure C.7. The plot of the maximum velocity error, Figure C.11, shows little variation. However, it is interesting to note that the level of velocity error is on the same order as seen in Figure C.8. So, one must assume that for this problem the y-direction hit location error is strongly tied to the x-direction grid resolution. This makes sense when it is realized that the trajectories examined here were predominantly in the x,y-plane. As before the VSAERO calculation time increases exponentially as grid resolution becomes more fine.

Finally, Figures C.13, C.14, and C.15 show the influence of z-direction grid resolution. Figure C.13 shows the z-direction hit accuracy improvement with increasing z-direction grid resolution. Accuracy improves below a delta z value of 0.006 m (0.02 ft) and is on the same order as that seen in the x-direction series (Figure C.7). The maximum velocity error is fairly steady also below a delta z value of 0.006 m (0.02 ft) (Figure C.14). The VSAERO calculation time curve behaves similar to the previous

plots.

Based on the results from this series, the value of
0.006 m (0.02 ft) was selected as a reasonable grid density
to be used for the 14.7 micron droplet cases in the future.
This was seen to be an appropriate value to balance accuracy
and computer time.

C.5 Study influence of droplet size on trajectory accuracy for given velocity grids

The accuracy of trajectories was examined for three
different drop sizes, 18.6, 14.7, and 11.5 microns. Figures
C.16 through C.30 examine this sequence of runs. For each
droplet size the x-,y-, and z-direction hit accuracies, the
maximum velocity errors, and the VSAERO calculation times
are plotted against the x-direction grid resolution.

It should be noted that the plots from different
droplet sizes should not be directly compared for this
series. This is due to the trajectories being different for
each droplet size. The trajectories for the 18.6 and 14.7
micron droplets started at the same point, but trajectory
for the 11.5 micron droplet did not. Due to the reduction
in the impingement limits as droplet size decreases, the

73

11.5 micron droplets were released much closer to the
centerline of the sphere to ensure that they struck the
sphere. Also, due to the differences between the mass and
drag of the 14.7 and 18.6 micron droplets, their
trajectories varied even though they started at the same
point.

The comparisons that should be made going from one
droplet size to another are the relationships between the
trajectory accuracies and the velocity accuracies. The hit
locations for all three directions (Figures C.16, C.17,
C.18, C.21, C.22, C.23, C.26, C.27, and C.28) become less
accurate as you go to smaller droplet sizes despite the
velocities becoming more accurate (Figures C.19, C.24,
C.29). This is due to the smaller droplets being more
influenced by the flowfield than their larger, more massive
counterparts. An infinitely massive droplet will not be
influenced by the flowfield at all, while the massless
droplet will follow the flowfield. Therefore, it makes
sense that the smaller droplets are more sensitive to error
in the flowfield than are larger droplets. One may conclude
from this that for a given level of accuracy, a more finely
resolved grid is required for a smaller droplet size than
would be needed for a larger droplet.

C.6 Influence of trajectory length upon trajectory accuracy

Trajectories were calculated for a range of starting x-locations (.9 to 2.6 m (3 to 8.5 ft) from sphere). The grid had a constant x-direction step size of 0.006 m (0.02 ft) with overall indices of 800x25x25. The trajectory lengths appeared to have minimal influence upon the accuracy of the trajectories (Figure C.31). No clear trend in maximum or summed velocity errors over the range of trajectory lengths were found (Figures C.32 and C.33). It is theorized that the error in velocity is only significant near the sphere, where the difference between droplet and flow velocities is greatest.

C.7 Study influence of minimum step size on trajectory accuracy

ICE uses a variable step size scheme for the trajectory calculations. An initial step size is set at the beginning of the trajectory, then at each step the step size is re-evaluated. If the curvature of the trajectory is greater than a threshold (about 2.5 degrees), then the step is subtracted and repeated with a smaller step size. This process is repeated until the trajectory curvature is within bounds, or a minimum step size is reached. A series of

calculations was performed varying minimum step size (0.00078 to 0.075) for two different droplet sizes (14.7 and 18.6 microns). As expected, the trajectories converge to a solution as minimum step size decreases (Figure C.34). Also, the larger droplet size converges much faster than the smaller one. As discussed above, this is caused by the lower influence of the velocity field on the trajectory of the larger, more massive droplet. To counter the increased accuracy gained by using a smaller minimum step size is the increase in computation time (Figure C.35). The number of steps to compute a trajectory goes up quite sharply when the minimum step size is reduced below 0.025. For the droplet sizes studied, the value of 0.025 for the minimum step size was deemed the best.

TABLES

Table I

Experimental spray run summary

DROPLET TRAJECTORY EXPERIMENT						
RUN #	Spray Time	Nozzle Location		Impingement Center		Drop Size
		from ___ wall	from floor	from ___ wall	from floor	MVD
	sec.	inches	inches	inches	inches	microns
------	------	------	------	------	------	------
1	30	south		south		21.5
		55.25	55.75	18	10	
2	20	south		south		21.5
		55.25	55.75	5	10	
3	20	south		south		16.5
		55.25	55.75	6	7	
4	20	north		north		16.5
		55.25	55.75	7	4	
5	20	north		north		21.5
		55.25	55.75	5	5	
6	20	north		north		21.8
		73	227.25	10	60	
7	25	north		north		15.2
		73	227.25	15	60	
8	25	north		north		16.5
		73	between sb 1&2	9	15	

RUN #	Spray Time	Nozzle Location		Impingement Center		Drop Size
		from ___ wall	from floor	from ___ wall	from floor	MVD
sec.	inches	inches	inches	inches	microns
9	25	north		north		21.5
		73	between sb 1&2	9	17	
10	20	north		north		16.5
		97	107	17	15	
11	20	north		north		21.5
		97	107	18	18	
12	20	north				
		121	131			
13	20	north		north		16.2
		121	131	27	25	
14	20	north		north		21.5
		121	131	28	25	
15	20	north		north		22
		145	154	44	34	
16	20	north		north		21.8
		145	154	44	37	
17	20	north		north		16.5
		145	154	42	33	

Table II

Comparison between Olsen and Reehorst experimental results

| Release Point (ft) | | Test Section Point, Reehorst data (ft) | | Test Section Point, Olsen/Ide data (ft) | | Error (Distance between points) (ft) | Notes |
Y	Z	Y	Z	Y	Z		
-9.98	-8.44	0.42	0.83	0.94	0.25	0.78	Outside of Curves
9.98	-8.44	8.58	0.42	8.75	0.25	0.24	Outside of Curves
8.5	5.85	8.17	5	7.5	4.75	0.72	Max. Error
8.5	-6.17	8.25	1.42	8.19	0.75	0.67	
6.5	-4.17	7.5	1.5	7.5	1.38	0.12	
4.5	-2.17	6.67	2.08	6.75	1.88	0.22	
2.5	-0.25	5.33	3.08	5.5	2.5	0.61	

Table III

Langmuir cloud droplet size distributions (Heinrich et al., 1991)

Total LWC in Each Size Group	Distributions of diameter/MVD				
percent	A	B	C	D	E
5	1.00	0.56	0.42	0.31	0.23
10	1.00	0.72	0.61	0.52	0.44
20	1.00	0.84	0.77	0.71	0.65
30	1.00	1.00	1.00	1.00	1.00
20	1.00	1.17	1.26	1.37	1.48
10	1.00	1.32	1.51	1.74	2.00
5	1.00	1.49	1.81	2.22	2.71

Table IV

Spray system droplet size distributions

Percent LWC	16.7 micron MVD case	18.6 micron MVD case
	Droplet Size (microns)	Droplet Size (microns)
5	5.27887	5.1522
10	8.31827	8.2956
20	11.47624	12.30762
30	16.7	18.6
20	22.94079	29.5089
10	32.75538	42.67398
5	47.24096	60.52812

Table V

Comparison of weighted average of cloud trajectory end-points and end-points from droplet with diameter of cloud MVD

IRT DROPLET DISTRIBUTION RUNS						
WEIGHTED AVERAGE		MVD VALUES		Yerror (feet)	Zerror (feet)	Run#
Y(ft)	Z(ft)	Y(ft)	Z(ft)			
3.310	-1.738	3.334	-1.760	-0.023	0.022	9
2.737	-1.201	2.754	-1.214	-0.017	0.013	11
1.968	-0.639	1.979	-0.645	-0.010	0.006	14
1.177	-0.078	1.183	-0.079	-0.006	0.001	16

Table VI

Comparison between experimental and computational trajectories

	IRT TRAJECTORY STUDIES (NO MODEL INSTALLED)						
	Experimental Release Point		Experimental Test Section Point		VSAERO/ICE Test Section Point		
RUN #	Y(ft)	Z(ft)	Y(ft)	Z(ft)	Y(ft)	Z(ft)	MVD
8	8.50	-6.17	3.75	-1.75	3.35	-1.78	16.5
9	8.50	-6.17	3.75	-1.58	3.33	-1.78	21.5
10	6.50	-4.17	3.08	-1.75	2.77	-1.23	16.5
11	6.50	-4.17	3.00	-1.50	2.75	-1.22	21.5
13	4.50	-2.17	2.25	-0.92	1.98	-0.66	16.2
14	4.50	-2.17	2.17	-0.92	1.98	-0.66	21.5
15	2.50	-0.25	0.83	-0.17	1.18	-0.09	22.0
16	2.50	-0.25	0.83	-0.08	1.18	-0.09	21.8
17	2.50	-0.25	1.00	-0.25	1.18	-0.09	16.5
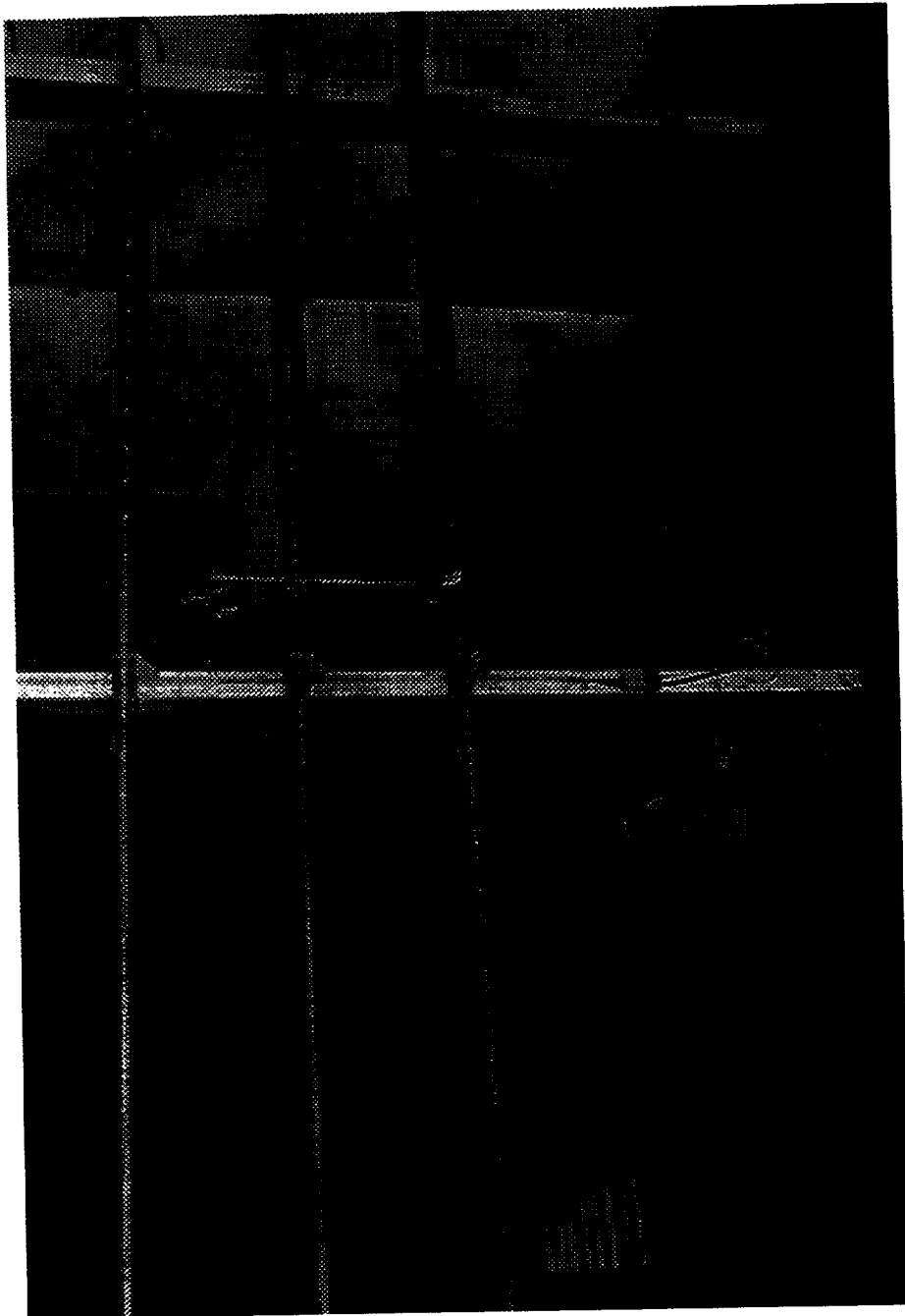
Figure 2.1 Dyed water spray system
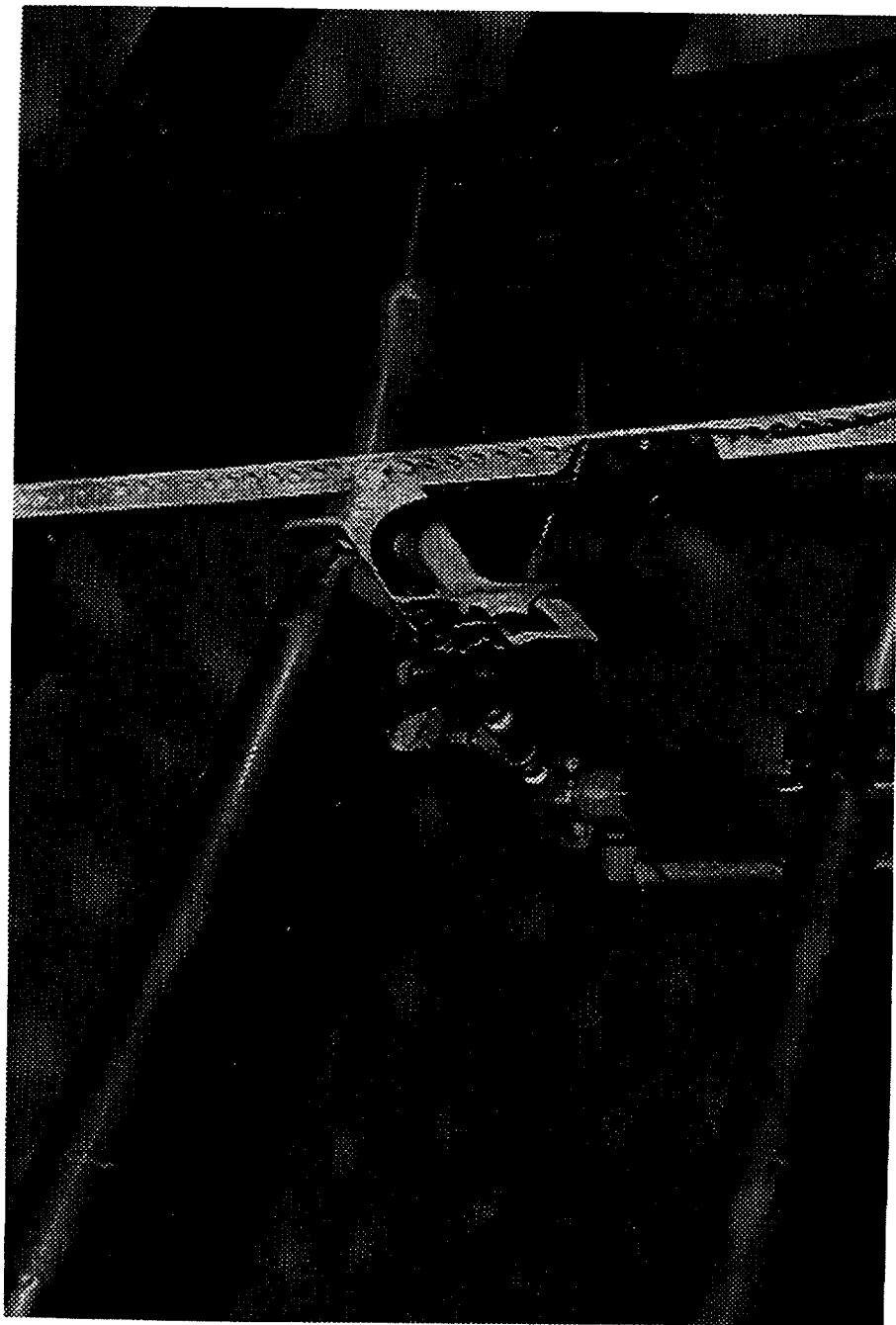
Figure 2.2   Spray nozzle assembly
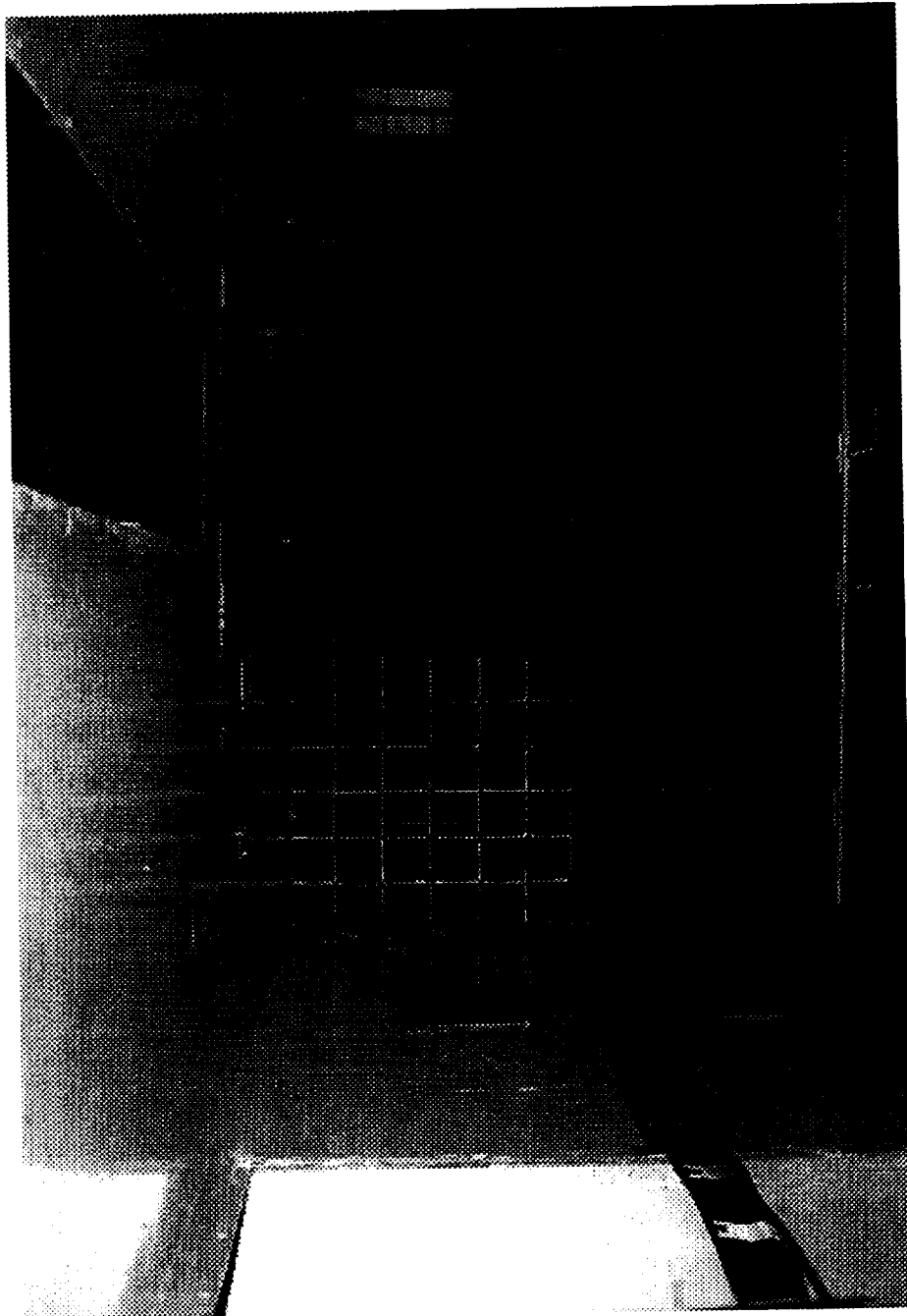
Figure 2.3 Brass grid installed in the IRT test section

Figure 2.4   Grid close-up showing blotter strips clipped in place
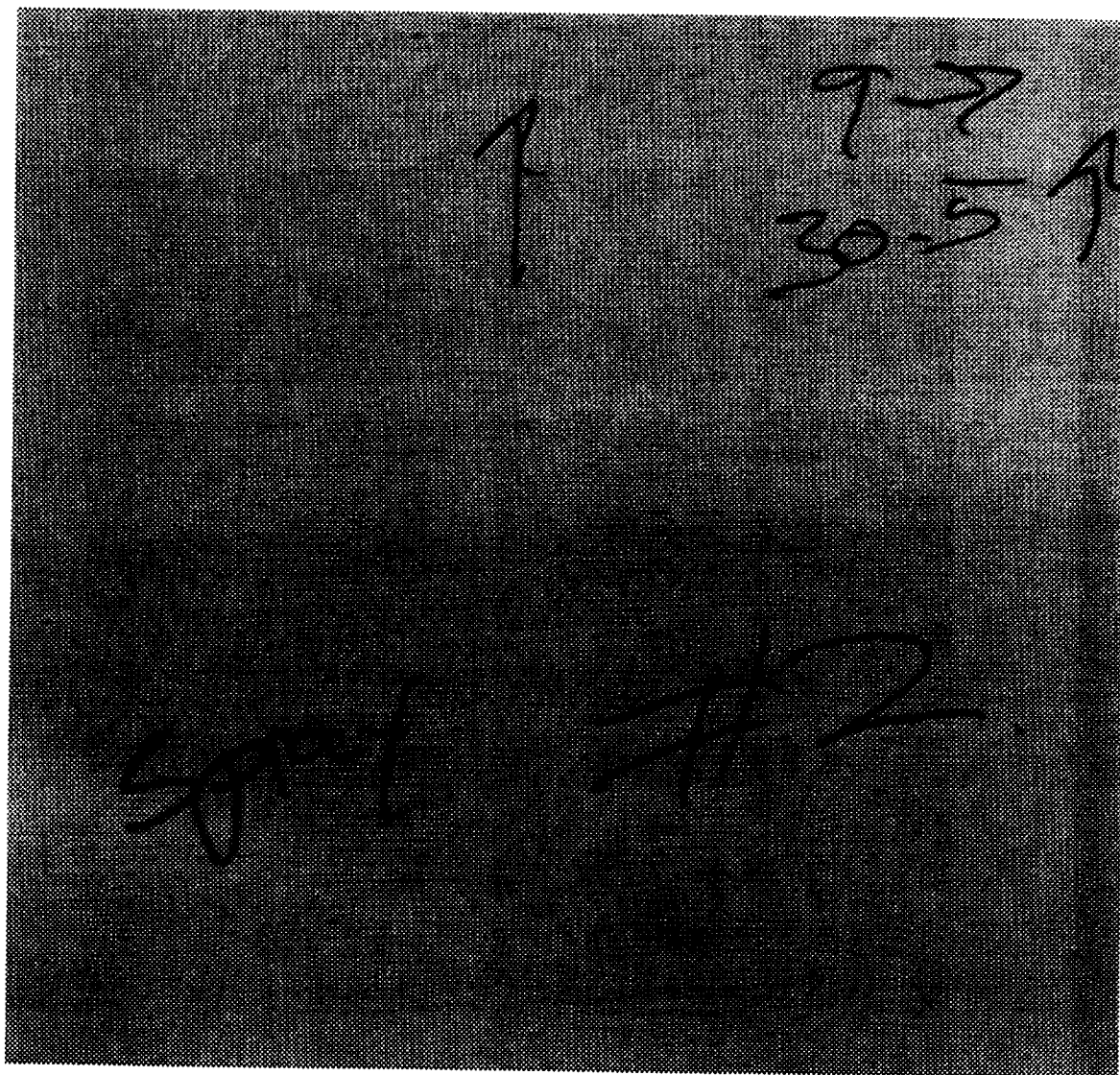
Figure 2.5   Blotter strip, level 0 dye concentration
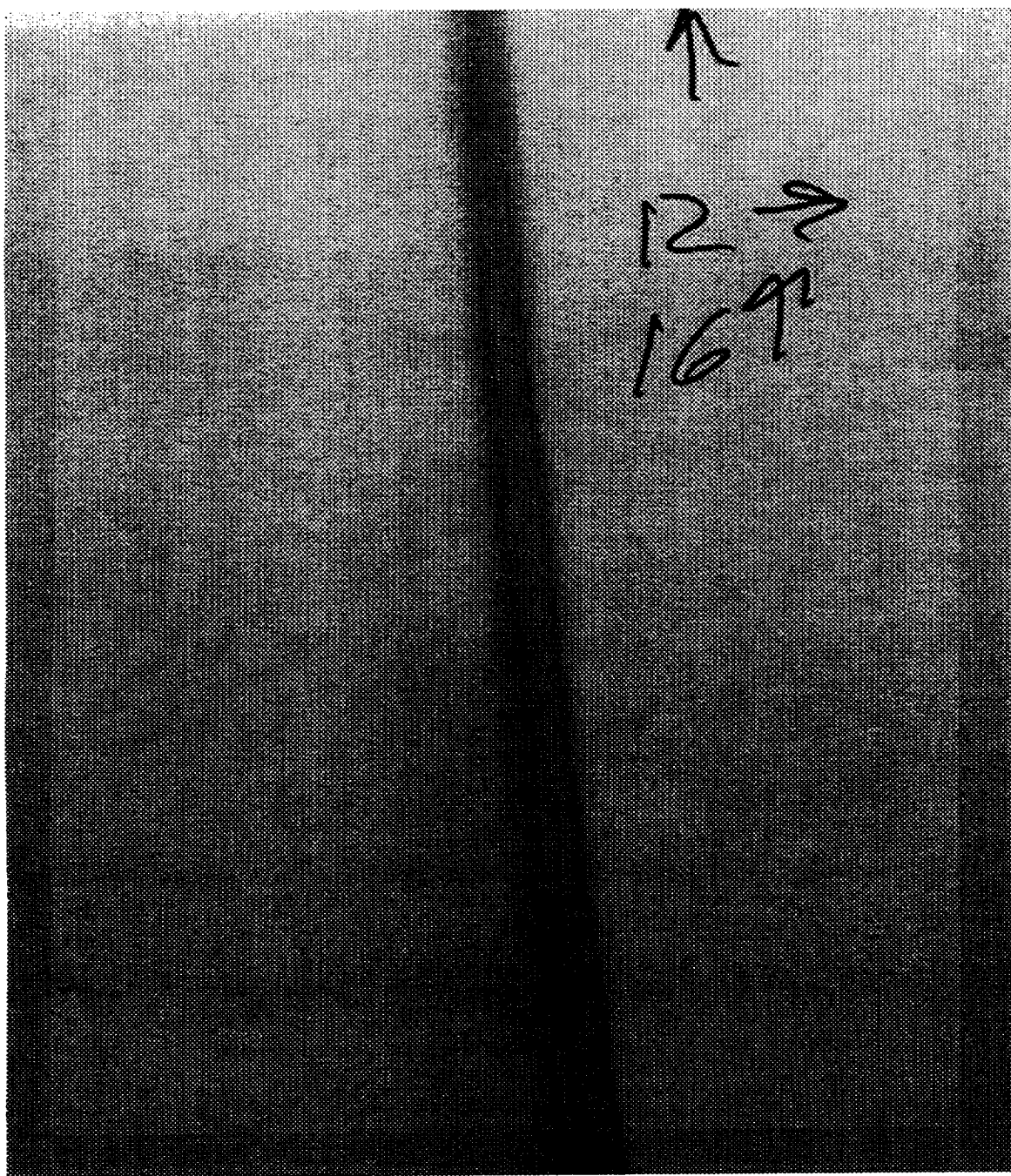
Figure 2.6 Blotter strip, level 2 dye concentration (top) and level 3 dye concentration (bottom)
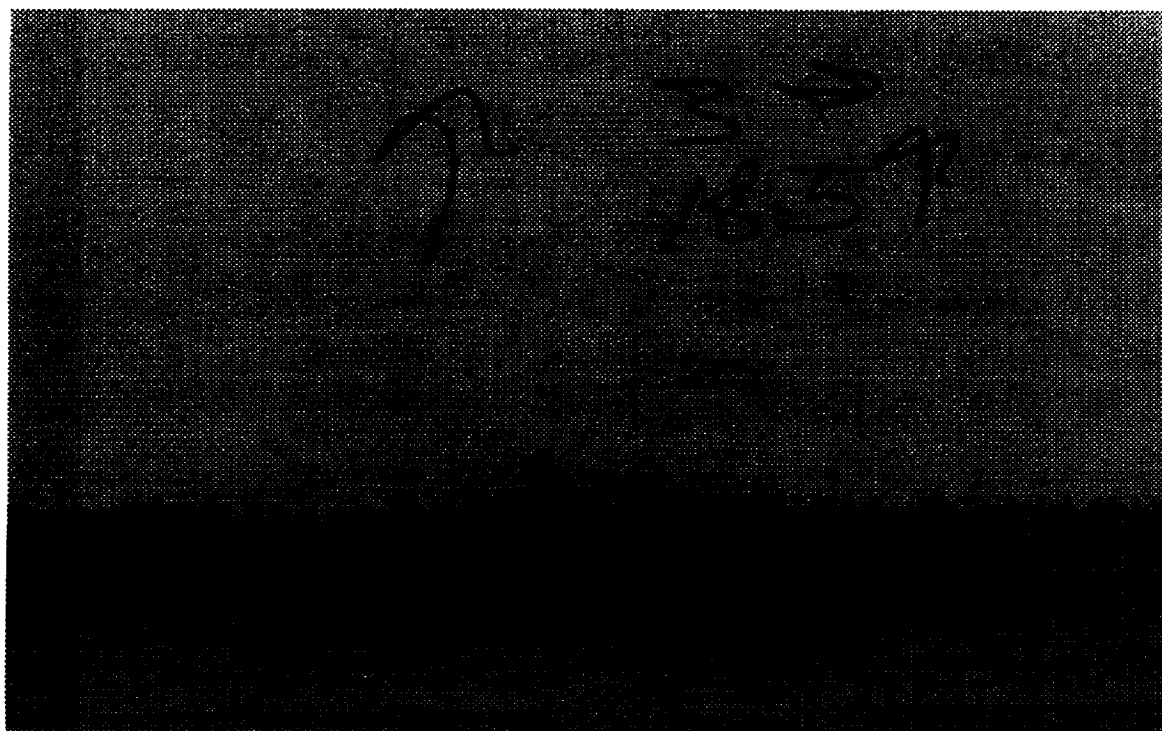
Figure 2.7   Blotter strip, level 4 dye concentration (right) and level 5 dye concentration
(center)
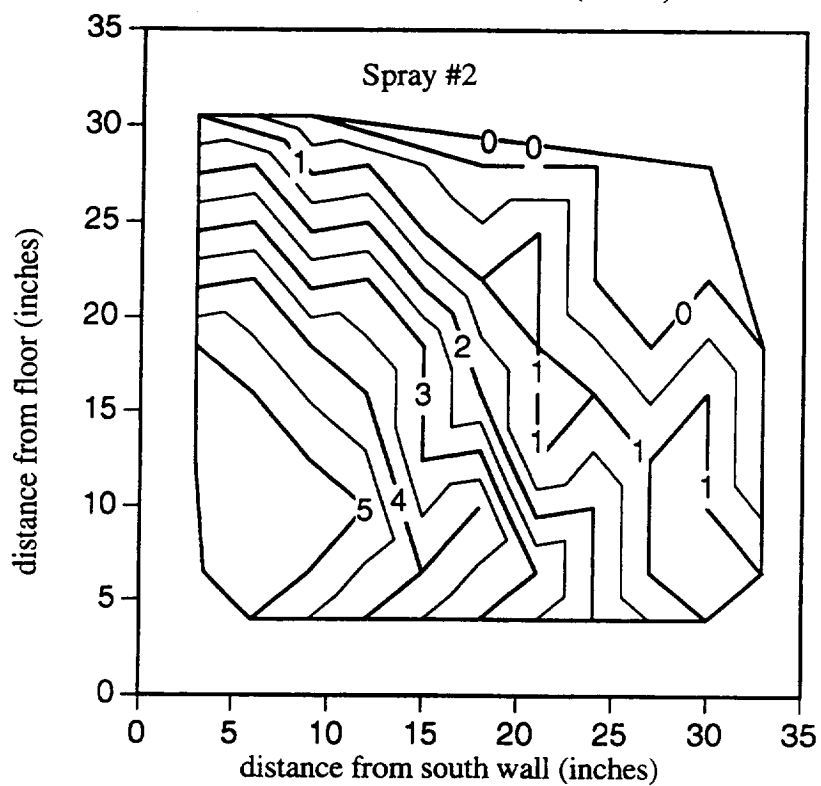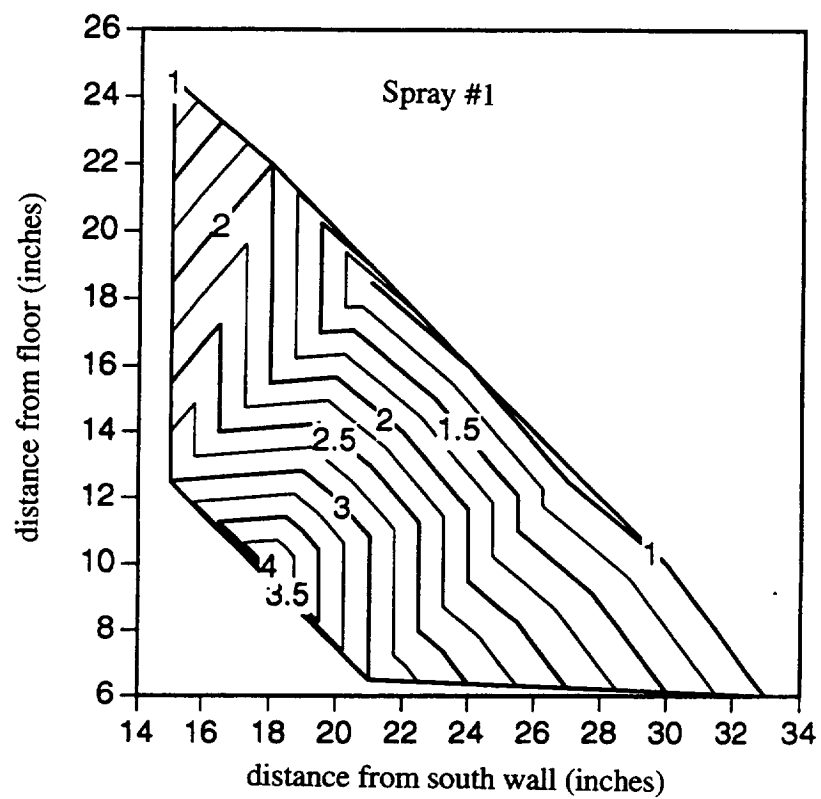
Figure 2.8   Contour plots of dye concentration for runs 1 and 2

91
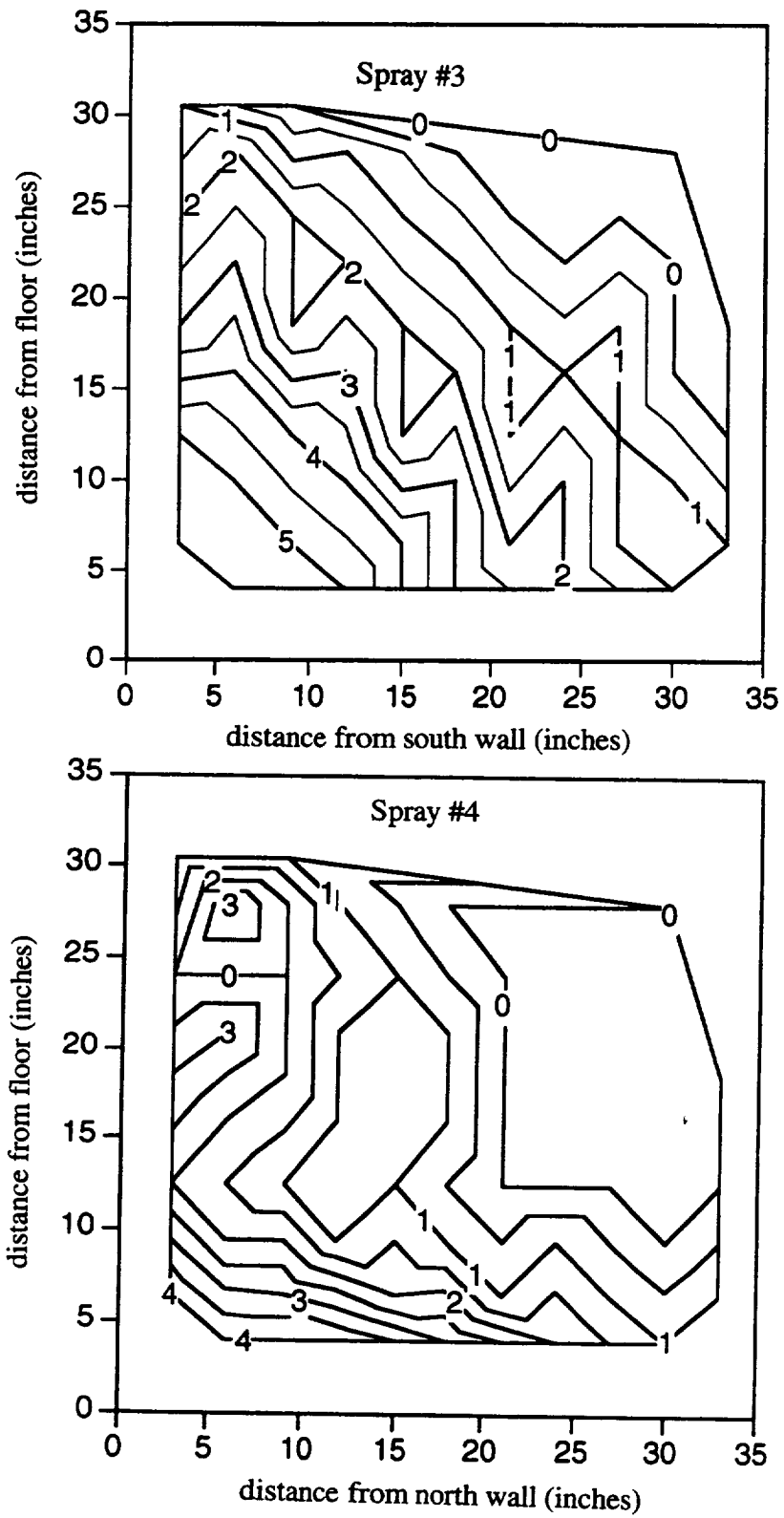
Figure 2.9 Contour plots of dye concentration for runs 3 and 4
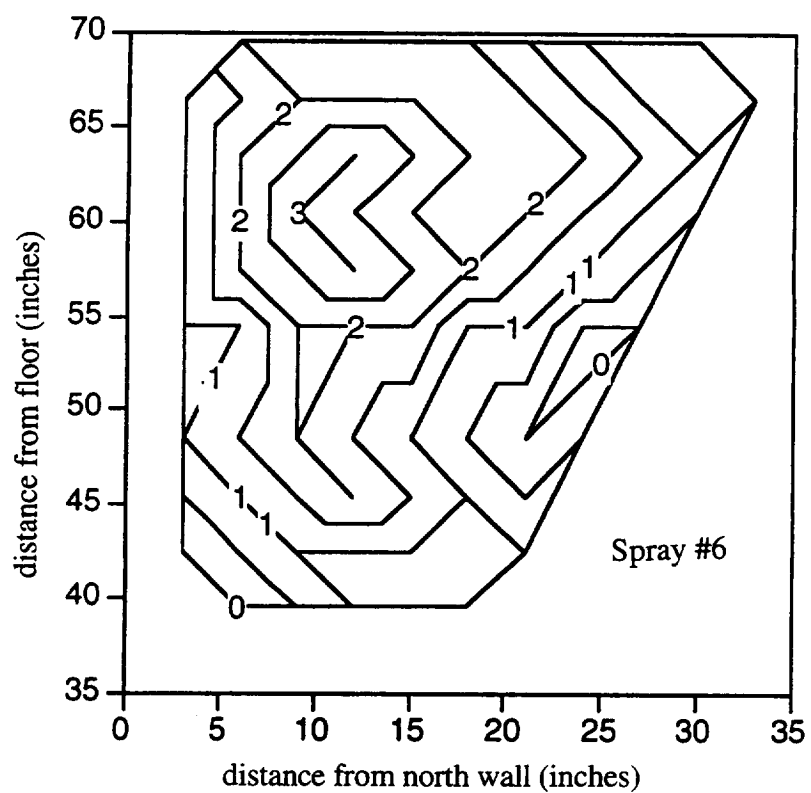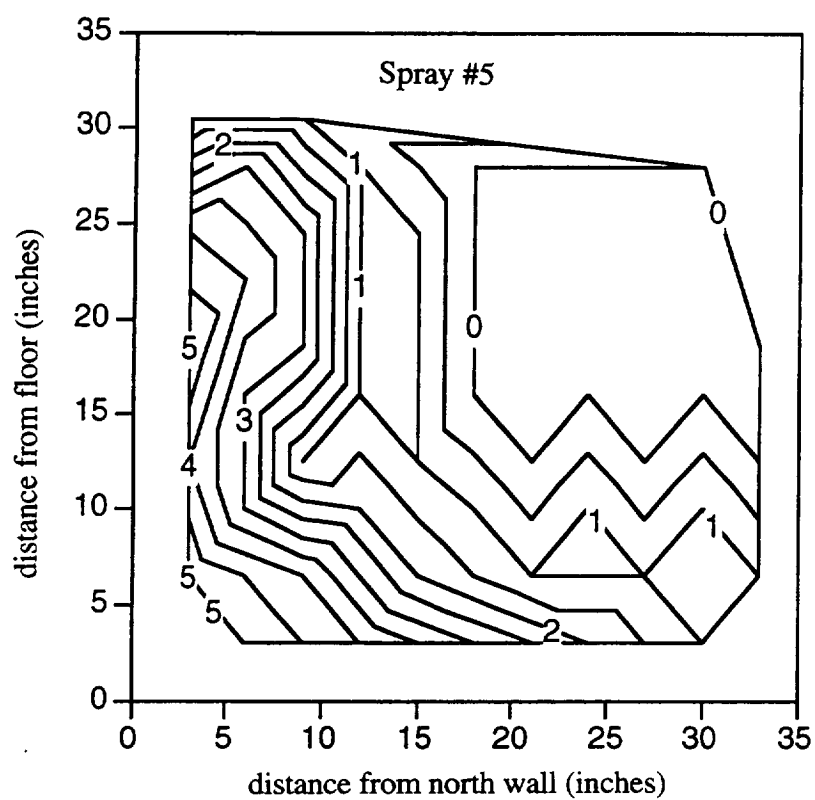
Figure 2.10 Contour plots of dye concentration for runs 5 and 6
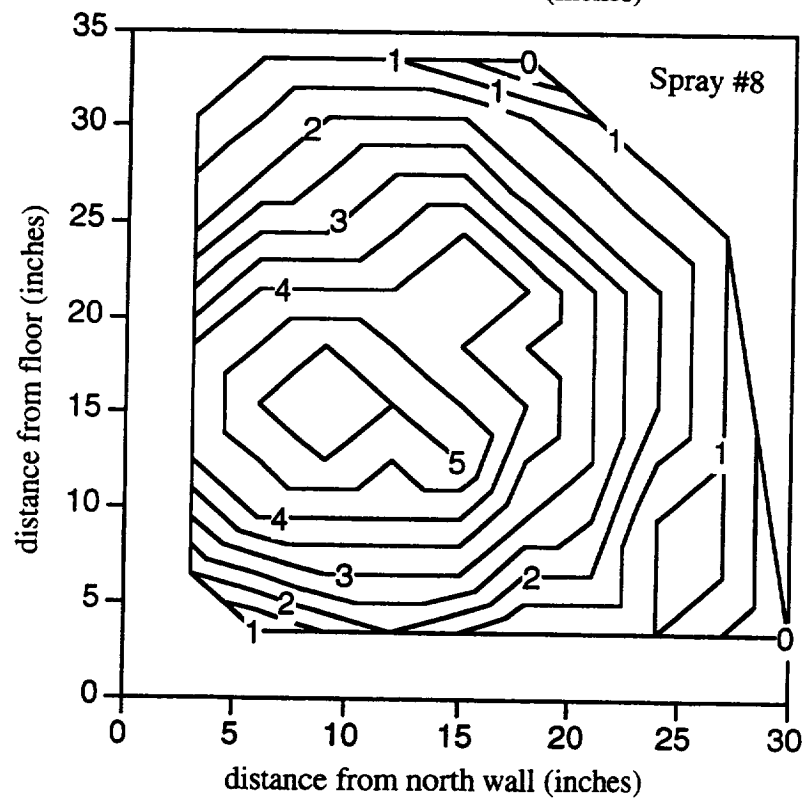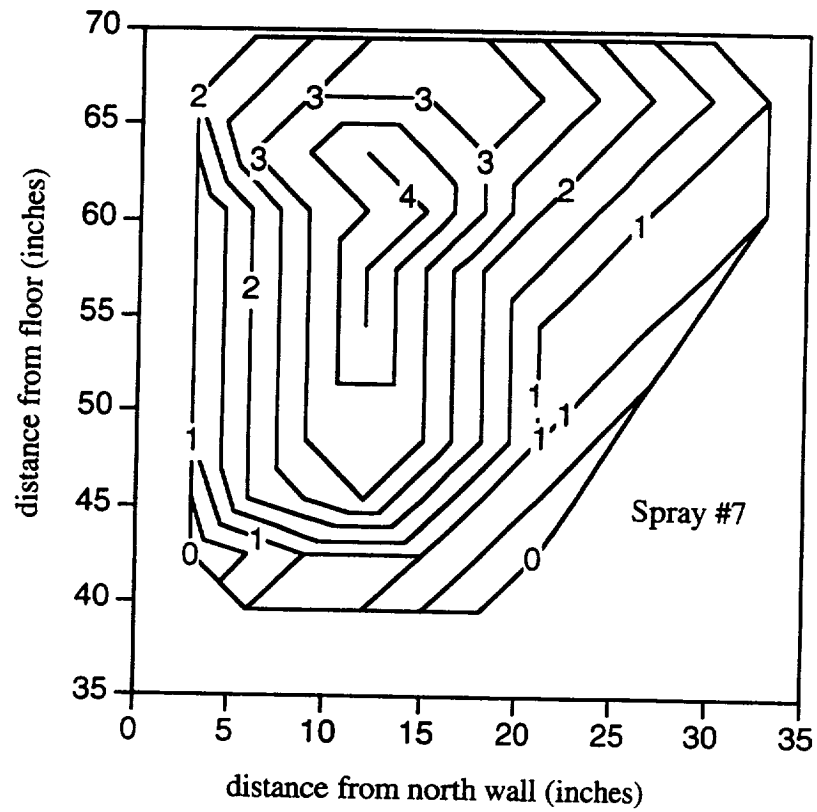
Figure 2.11 Contour plots of dye concentration for runs 7 and 8
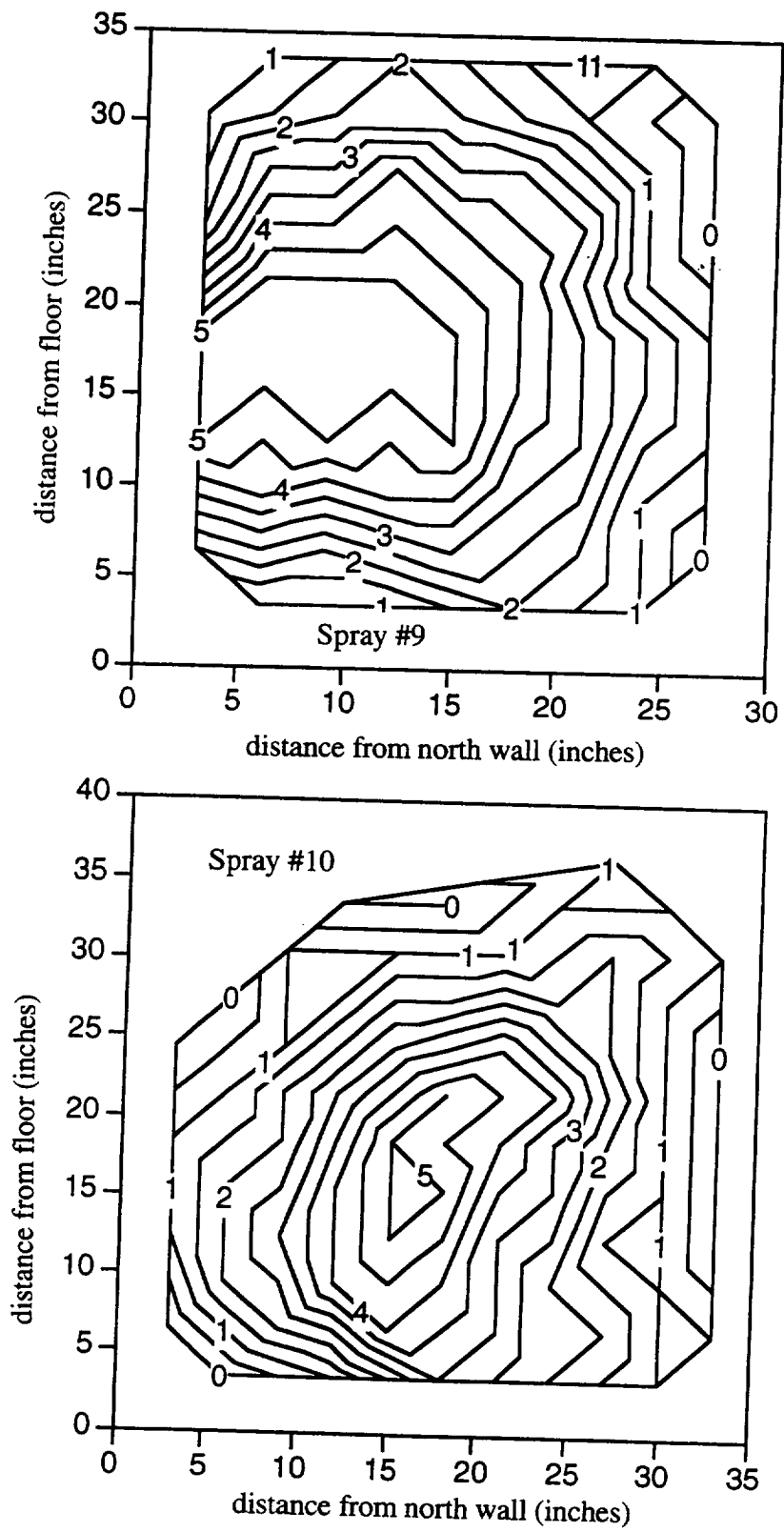
Figure 2.12 Contour plots of dye concentration for runs 9 and 10
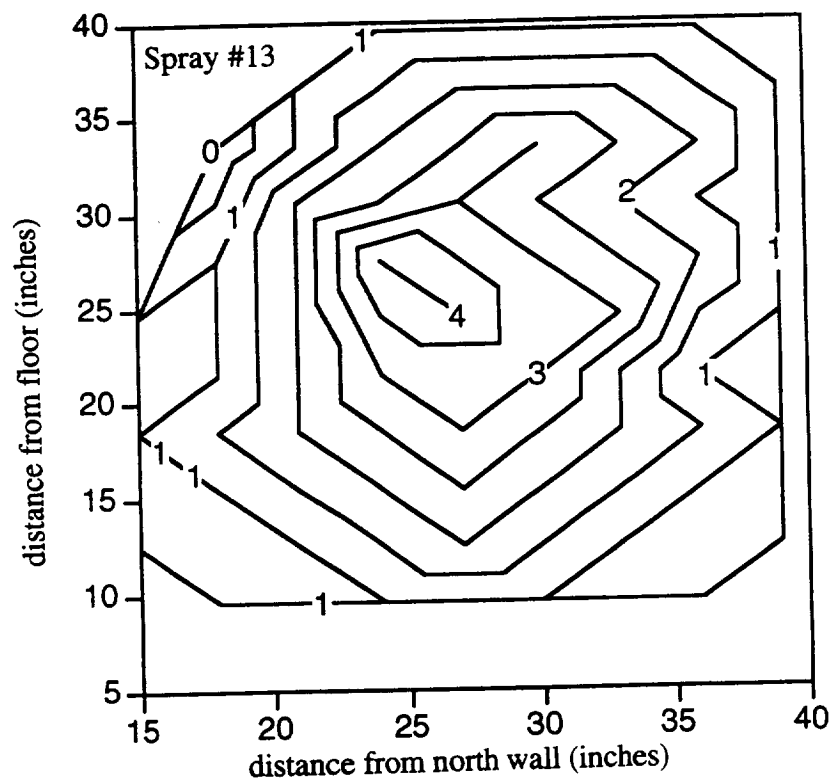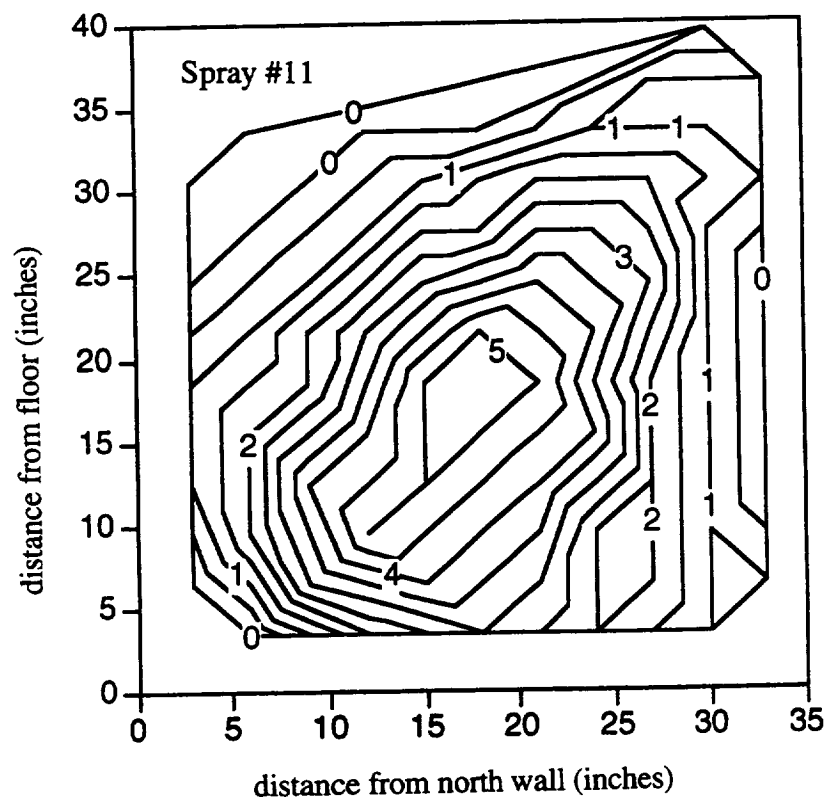
Figure 2.13 Contour plots of dye concentration for runs 11 and 13
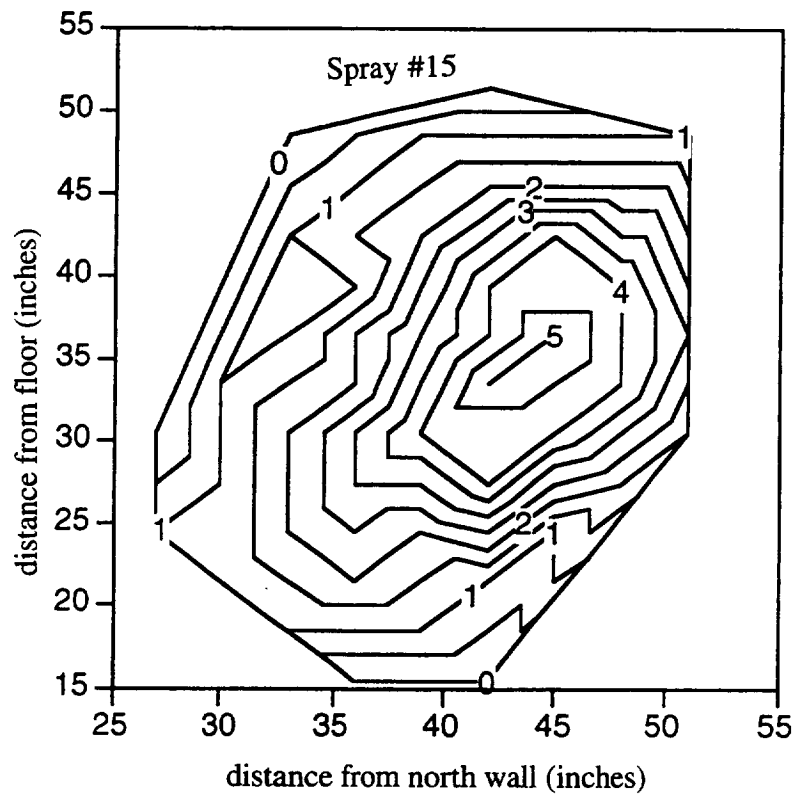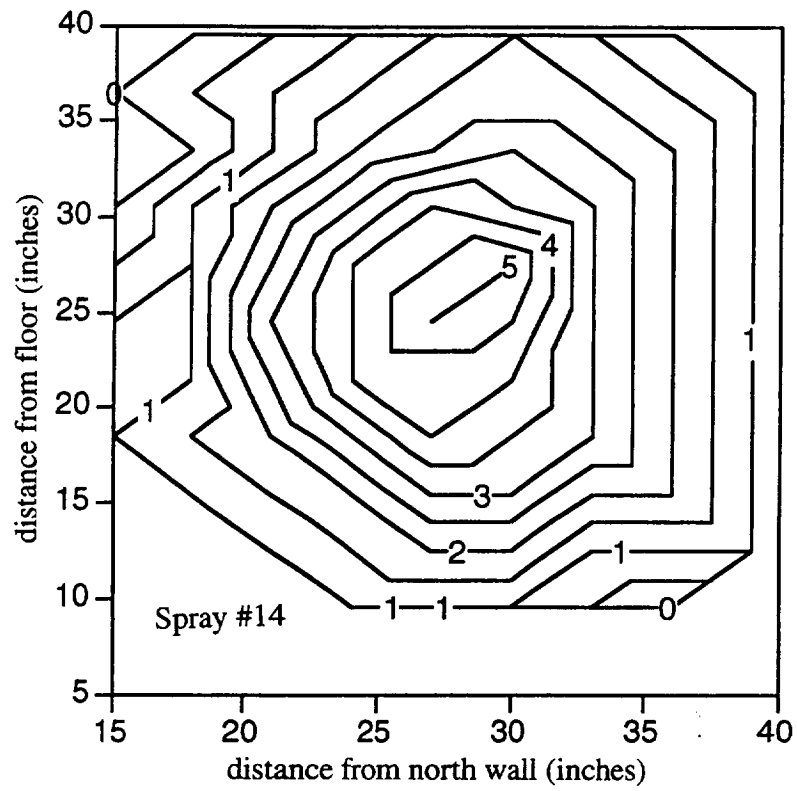
Figure 2.14 Contour plots of dye concentration for runs 14 and 15
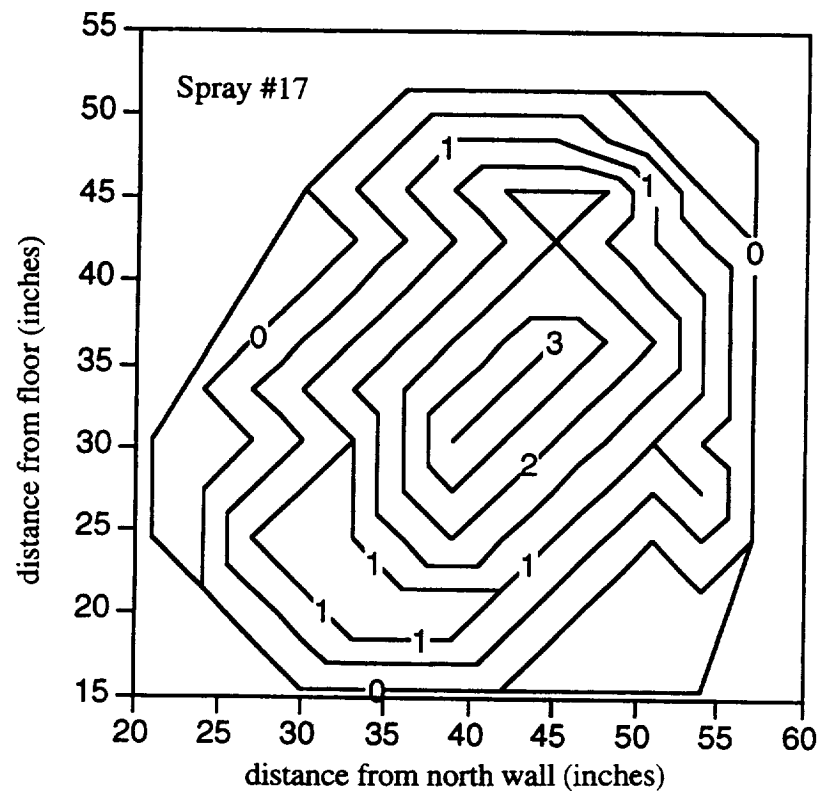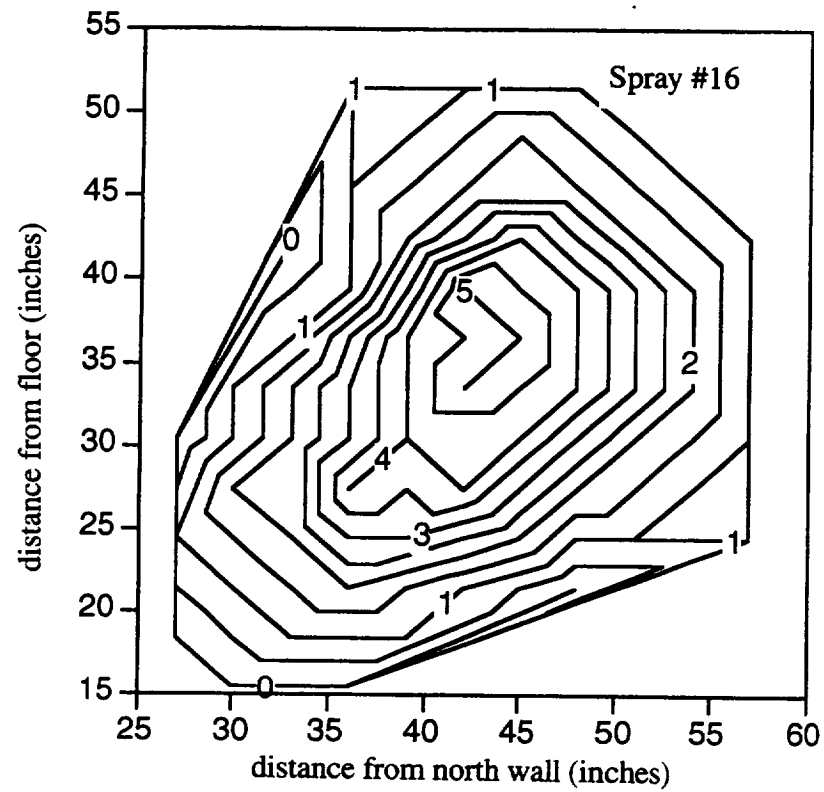
Figure 2.15 Contour plots of dye concentration for runs 16 and 17
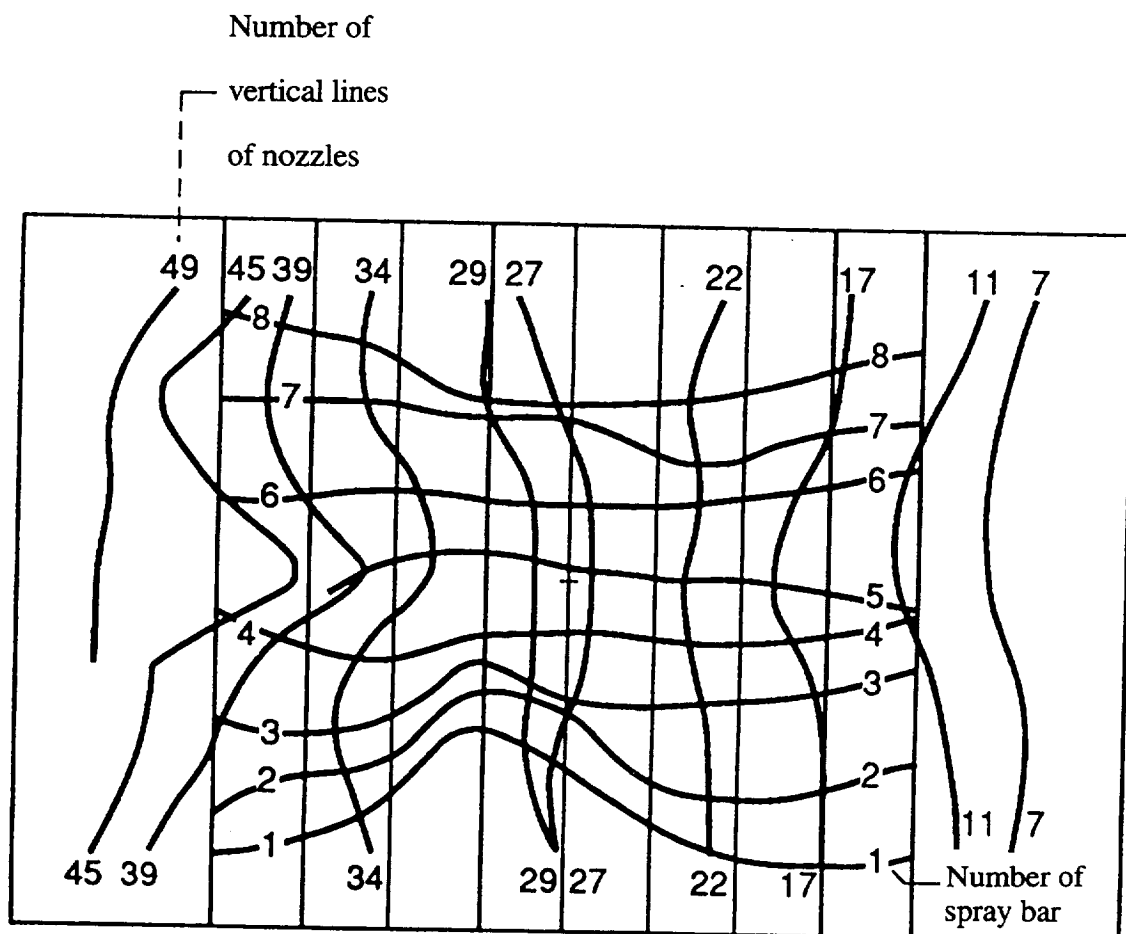
Figure 2.16 Map of peak LWC from each spray bar and vertical line of nozzles

(Ide, 1990)
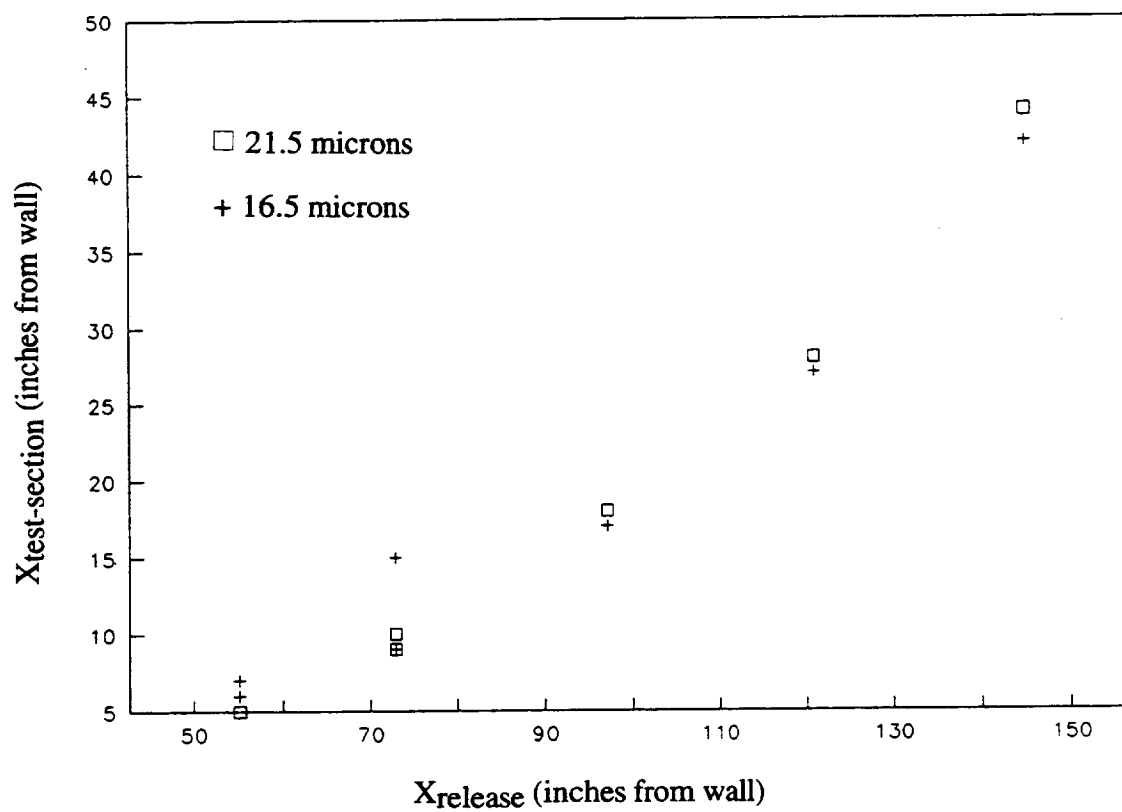
Figure 2.17 X-direction trajectory data plot
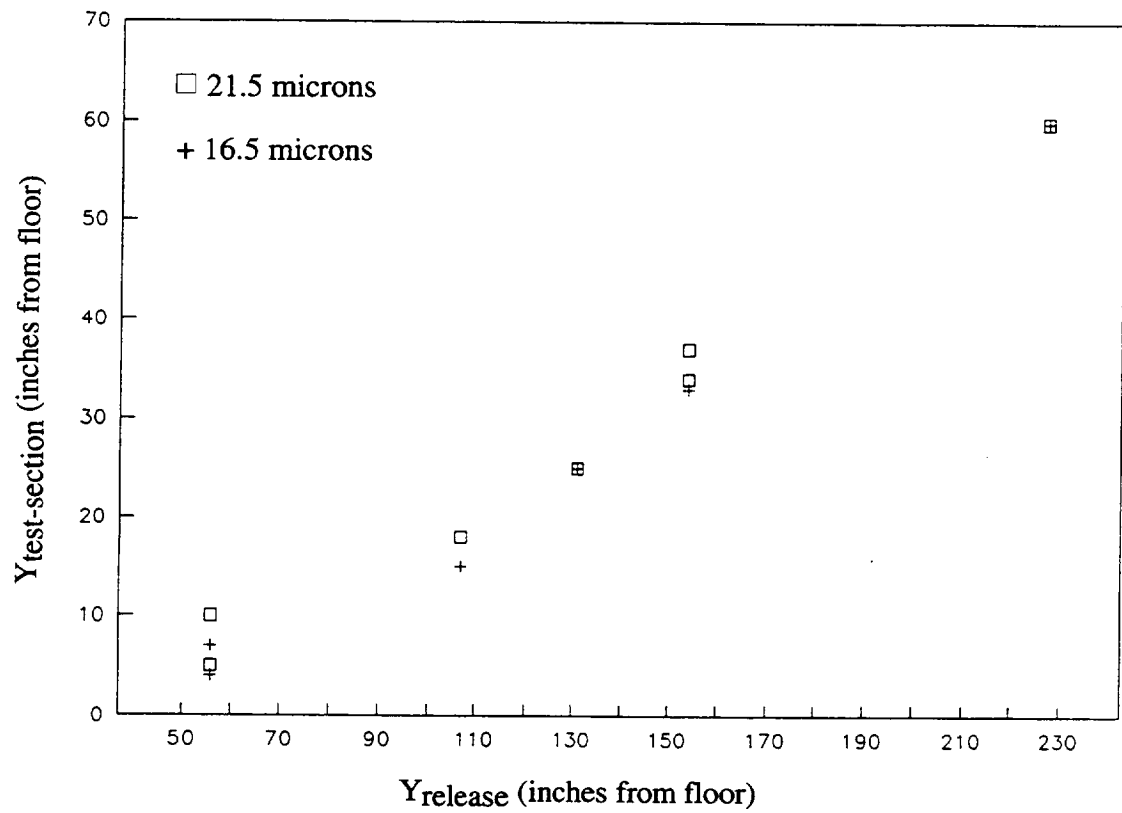
Figure 2.18 Y-direction trajectory data plot
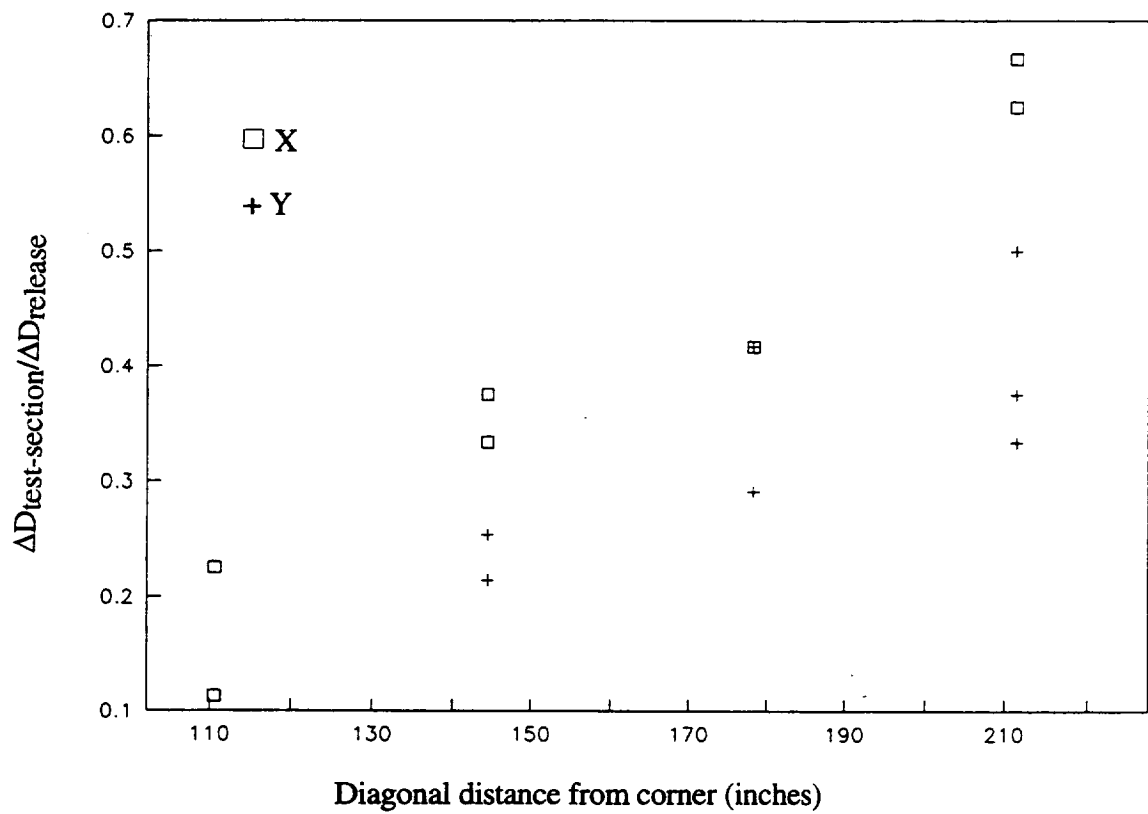
Figure 2.19 Change in trajectory spacing based upon release point
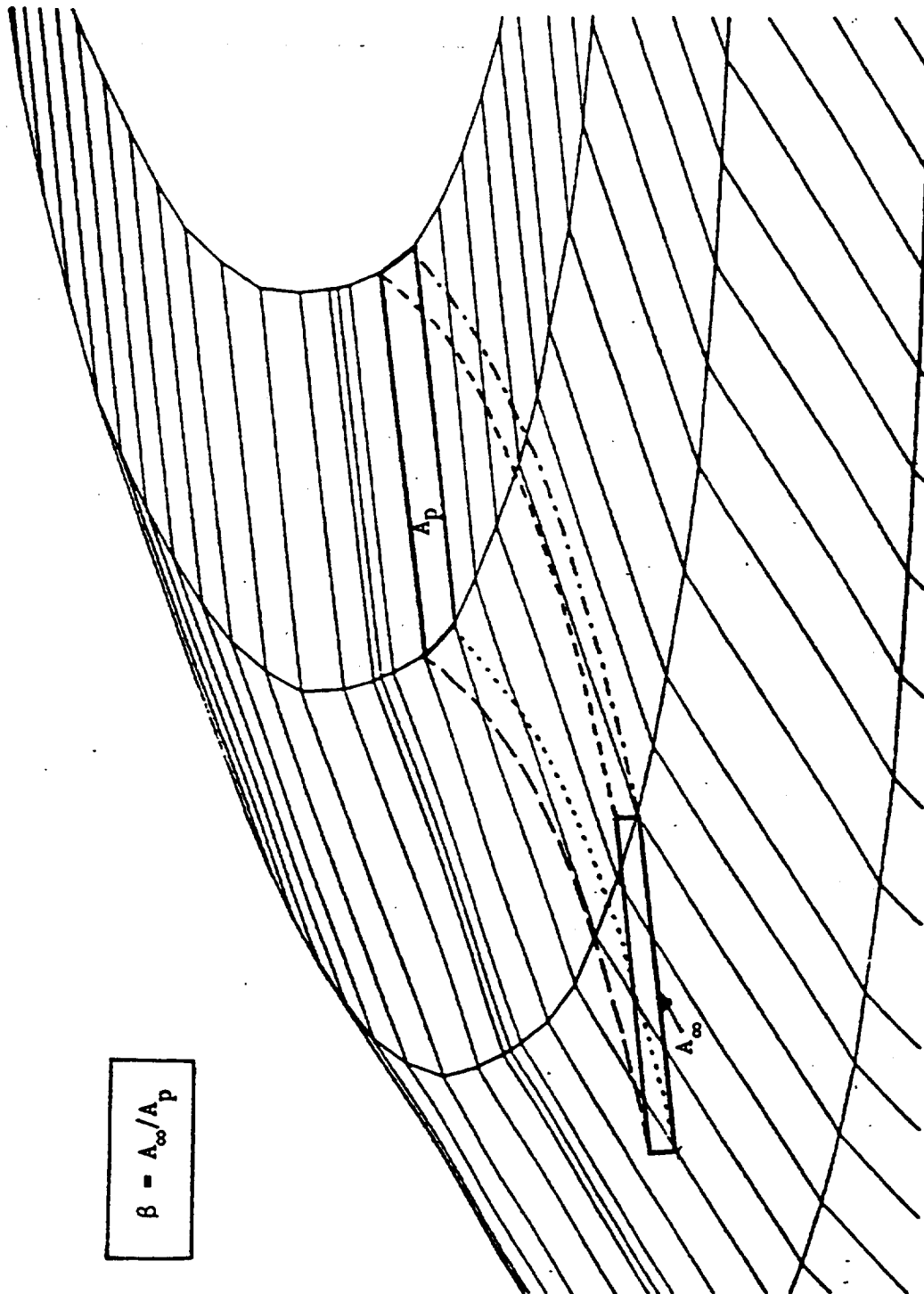
Figure 3.1 The panel-by-panel collection efficiency calculation

$$\beta = A_\infty / A_p$$

103
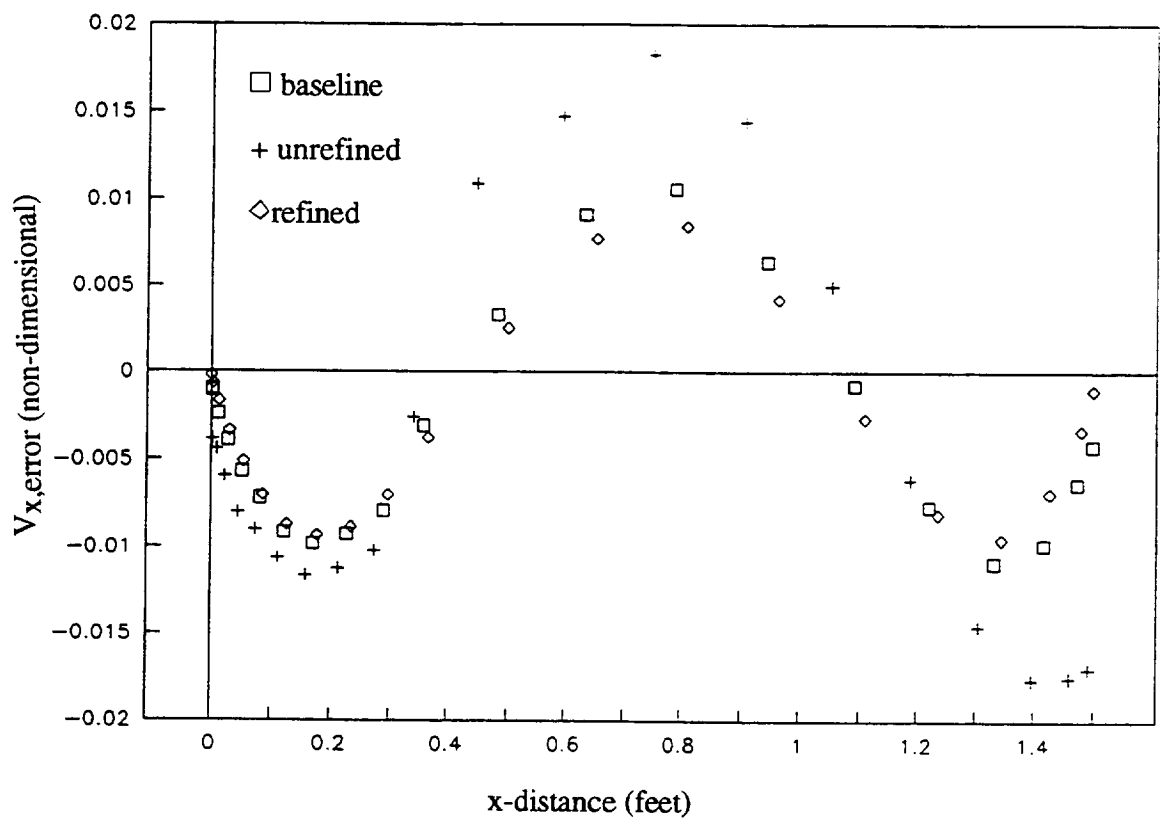
Figure 3.2   VSAERO sphere accuracy study, $V_{x,error}$ vs. x
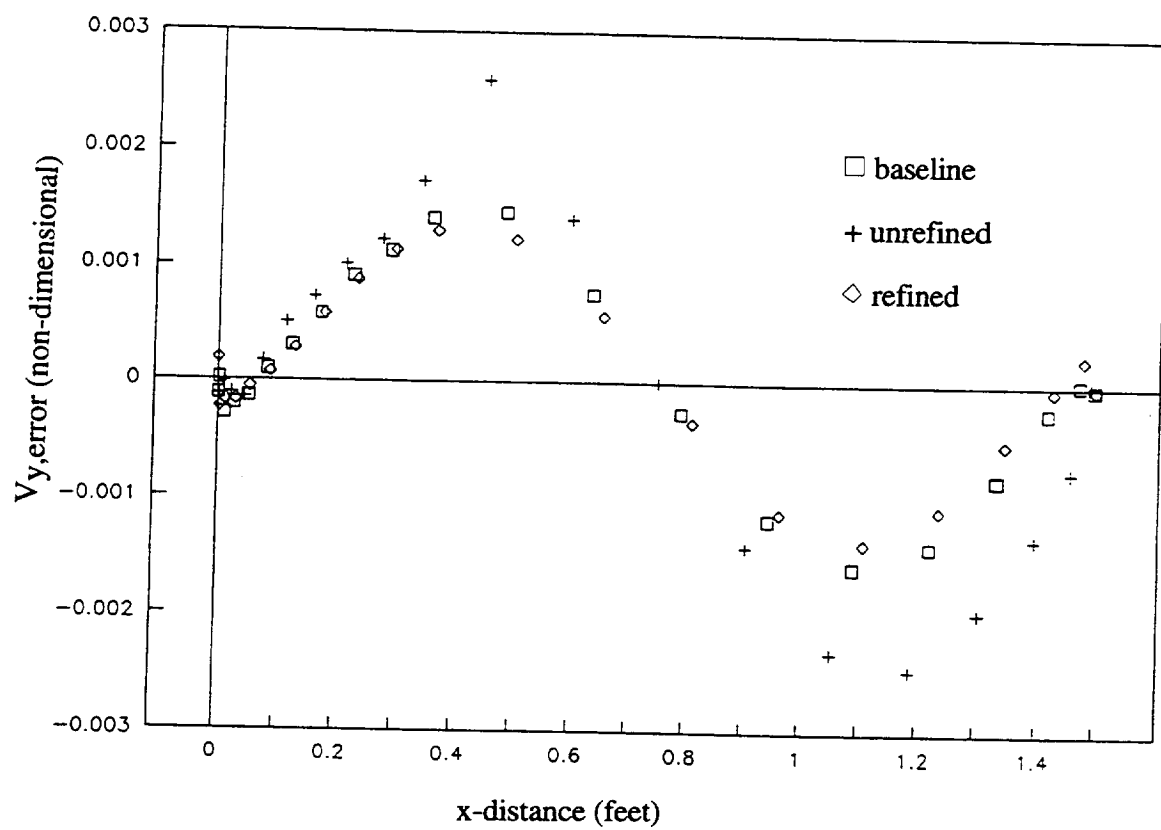
Figure 3.3 VSAERO sphere accuracy study, $V_{y,error}$ vs. x

105
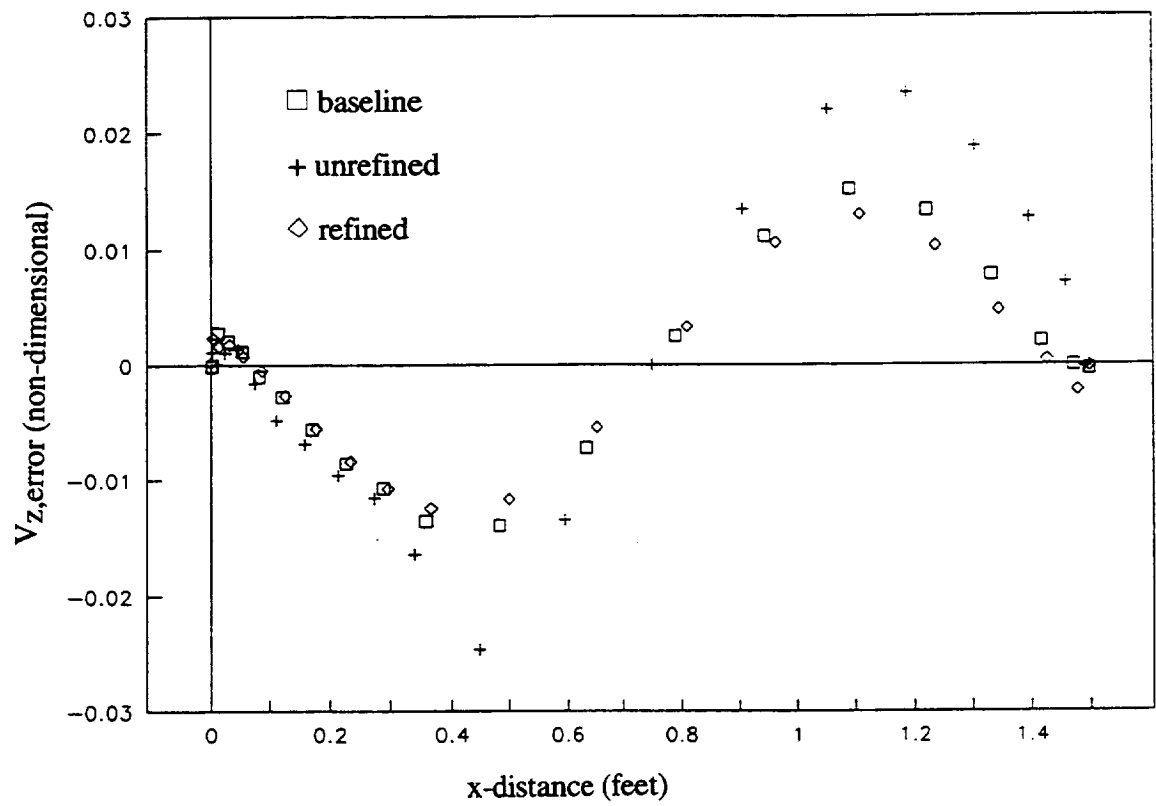
Figure 3.4   VSAERO sphere accuracy study, $V_{z,error}$ vs. x
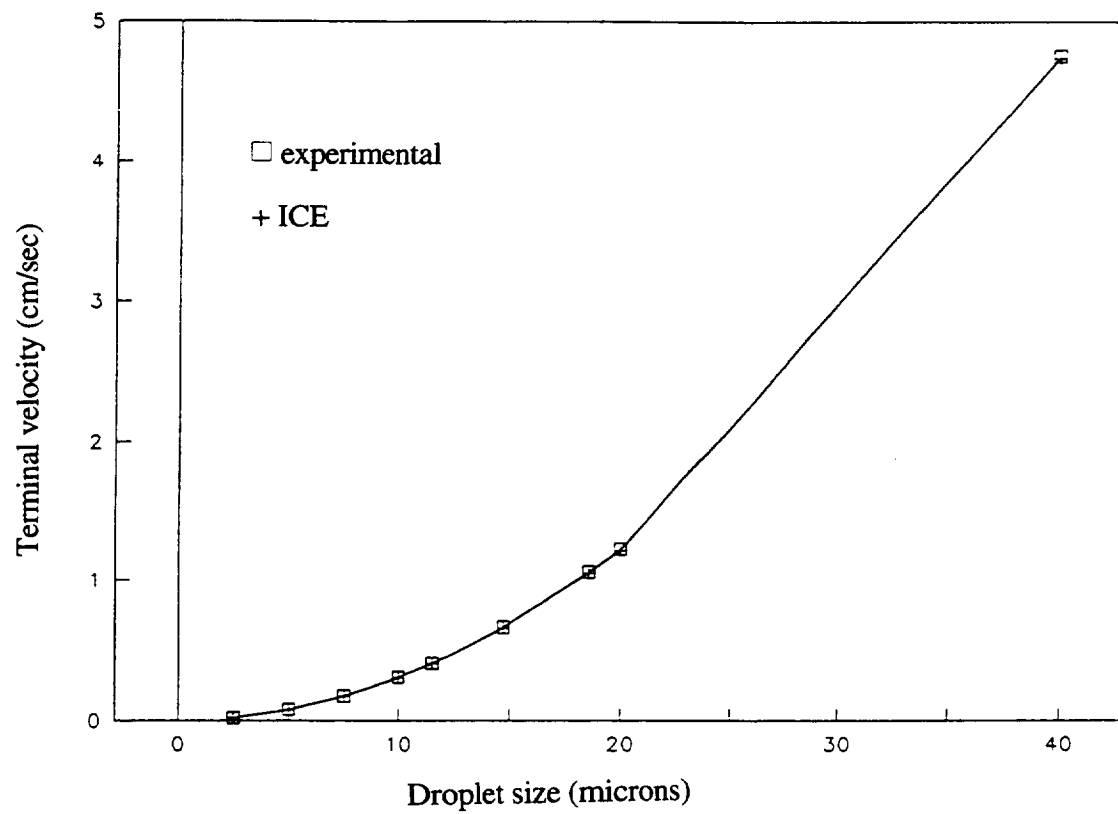
Figure 3.5 Terminal velocities for droplets released in stagnant air
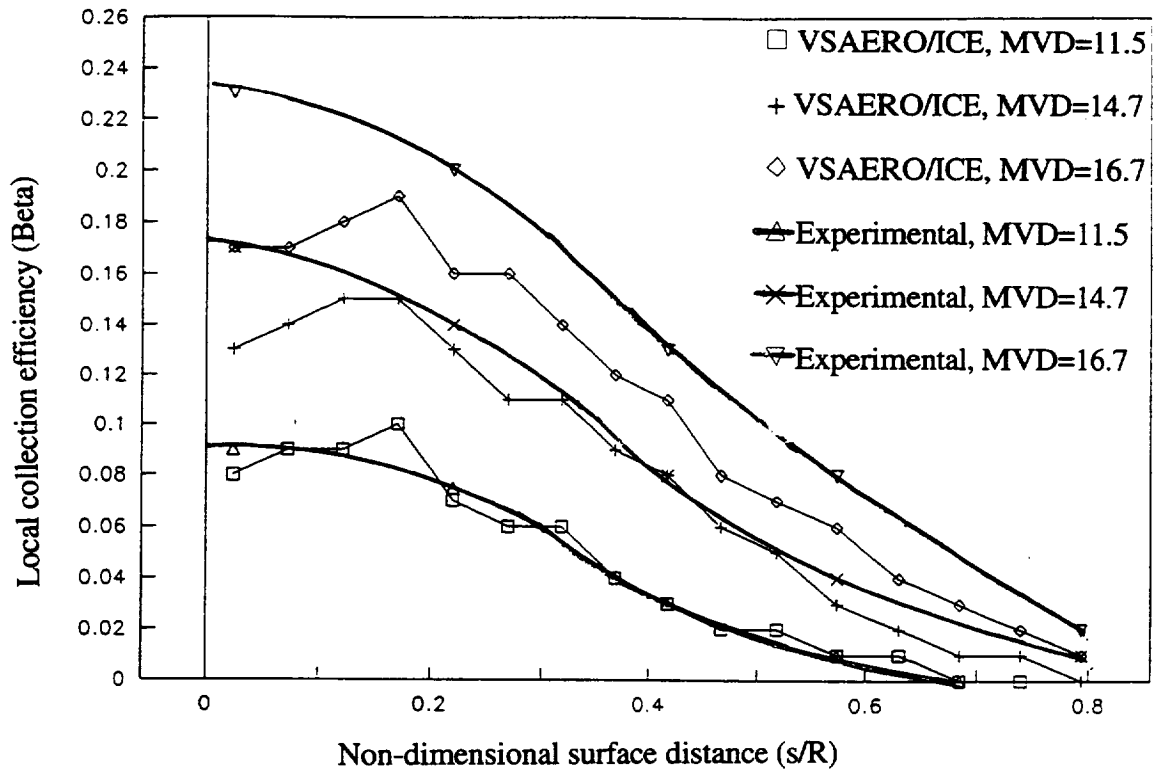
Figure 3.6 Collection efficiency calculated by ICE using VSAERO velocities and a seven

bin Langmuir-D droplet distribution on a nine inch sphere for MVDs of 11.5, 14.7, and

16.7 microns
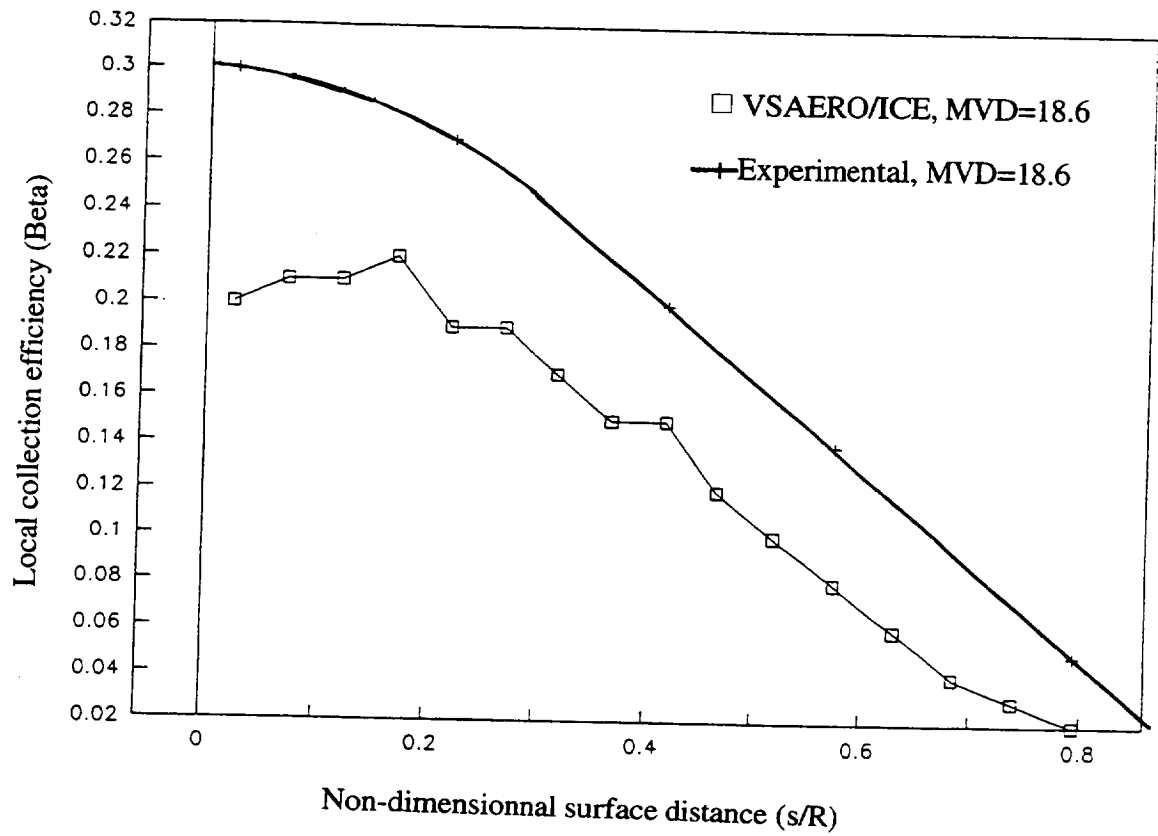
Figure 3.7   Collection efficiency calculated by ICE using VSAERO velocities and a seven
bin Langmuir-D droplet distribution on a nine inch sphere for MVD of 18.6 microns
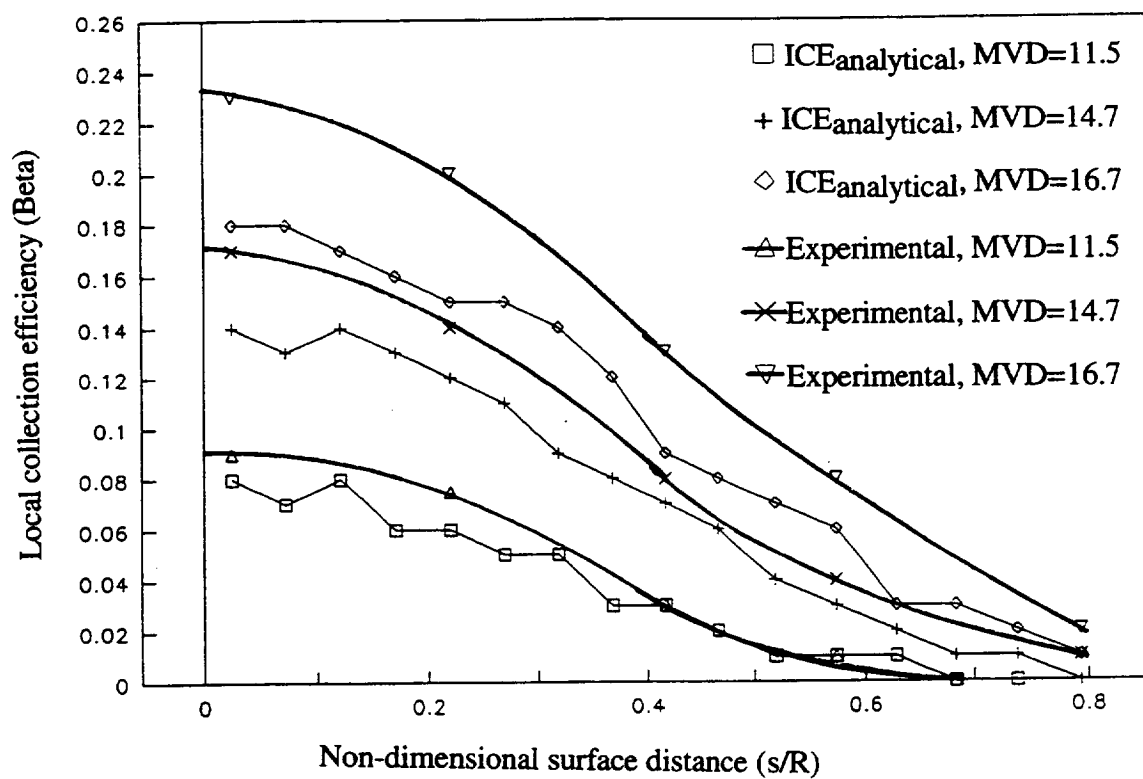
Figure 3.8 Collection efficiency calculated by ICE using analytical velocities and a seven

bin Langmuir-D droplet distribution on a nine inch sphere for MVDs of 11.5, 14.7, and

18.6 microns
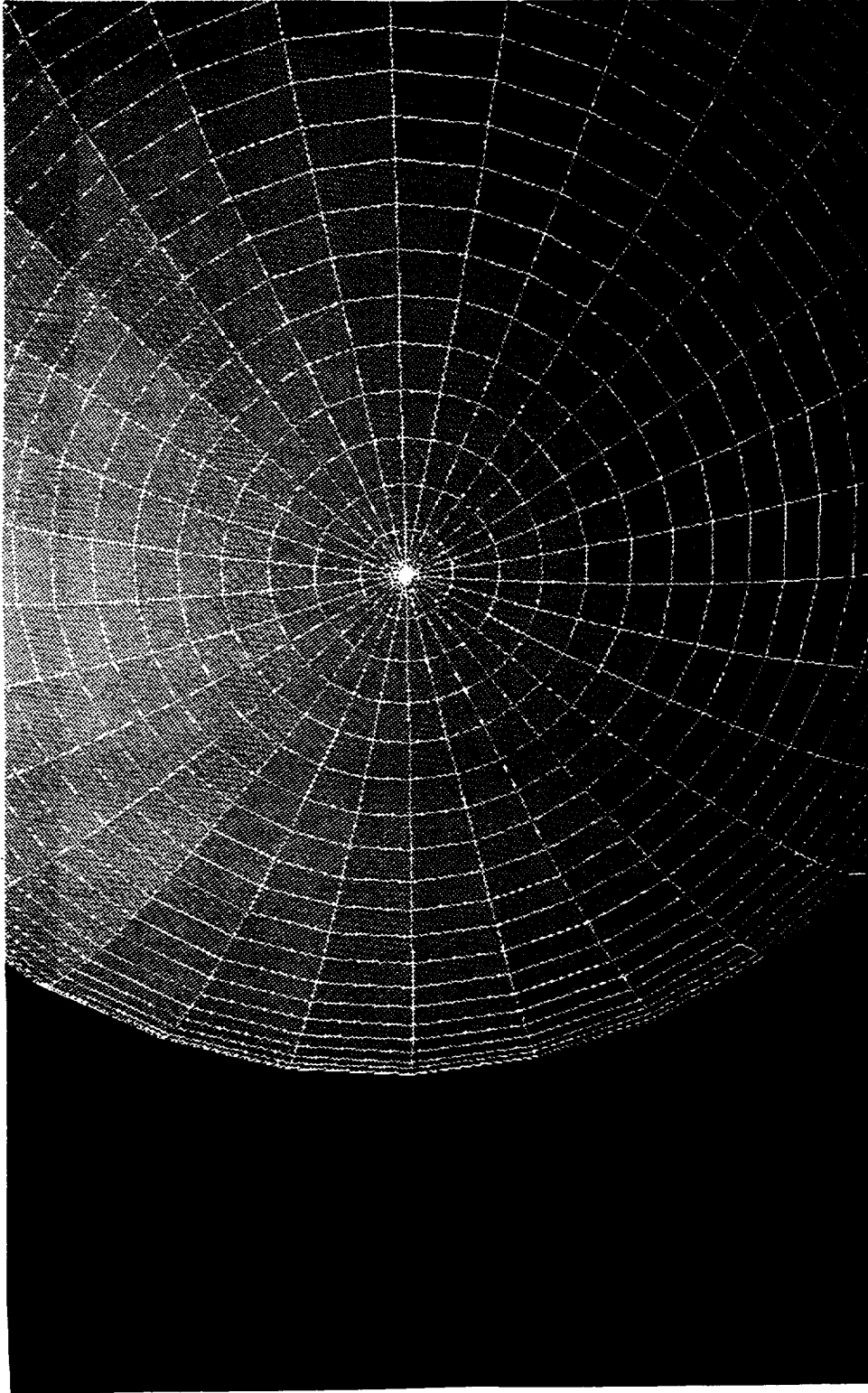
Figure 3.9 Panel representation of a sphere showing small triangular panels near the stagnation point
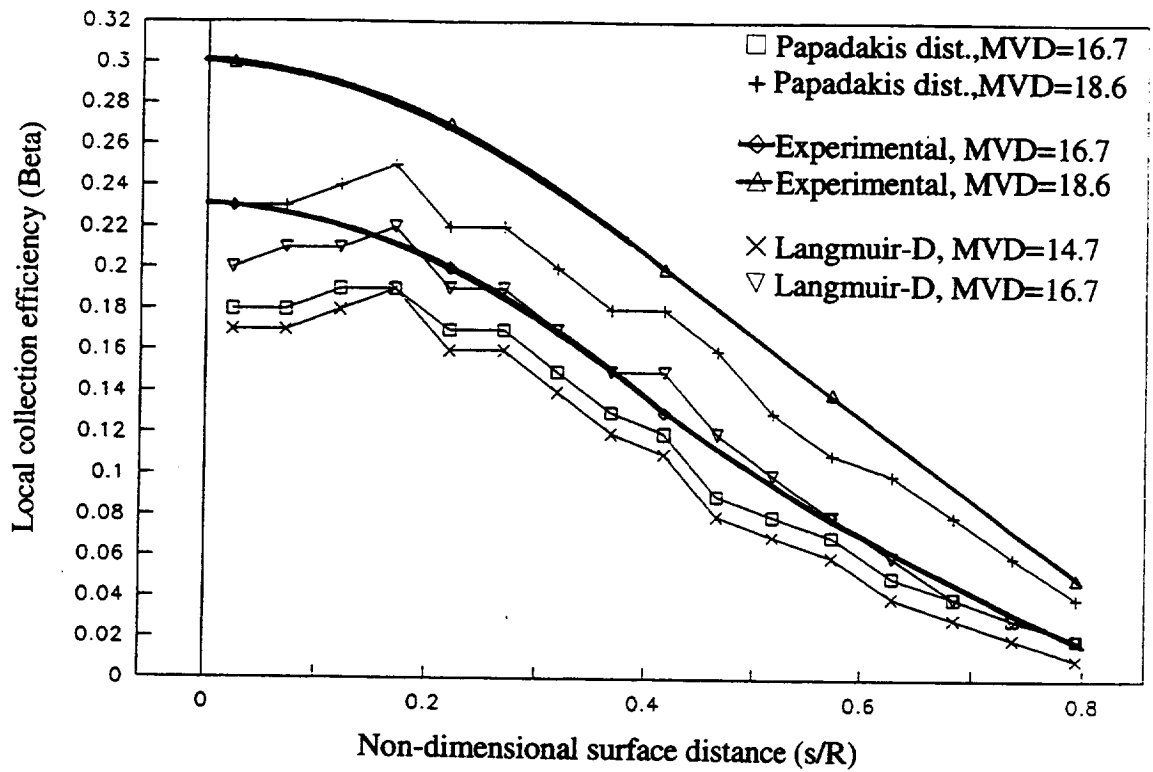
Figure 3.10 Collection efficiency calculated by ICE using VSAERO velocities and seven bin Papadakis and Langmuir-D droplet distributions on a 0.23 m (9 in) sphere for MVDs of 16.7 and 18.6 microns

Figure 3.11 VSAERO panel model of IRT from spray bar plane through the test section and diffuser

113
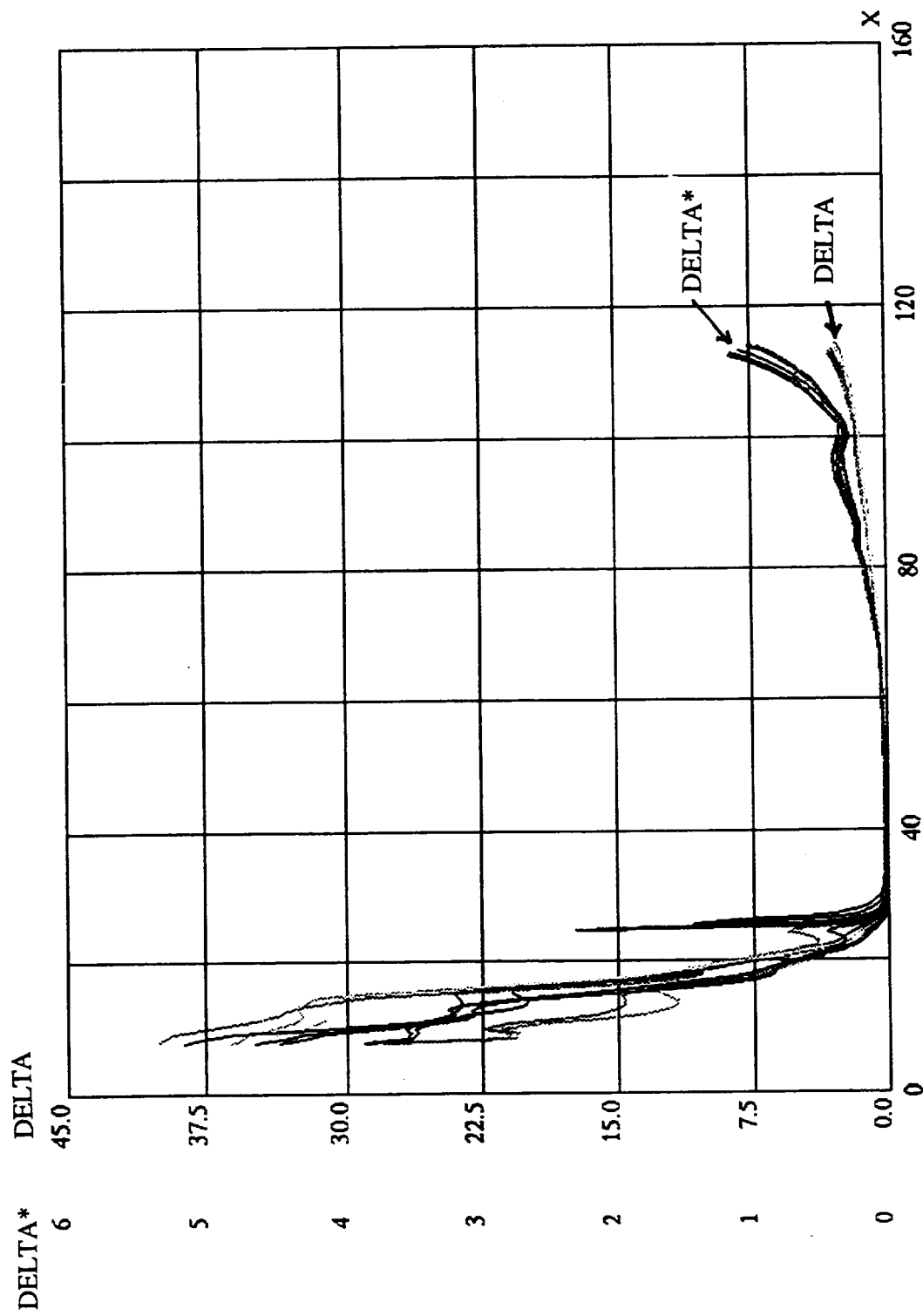
Figure 3.12 Boundary layer thickness and displacement thickness calculated along streamlines in the IRT

114
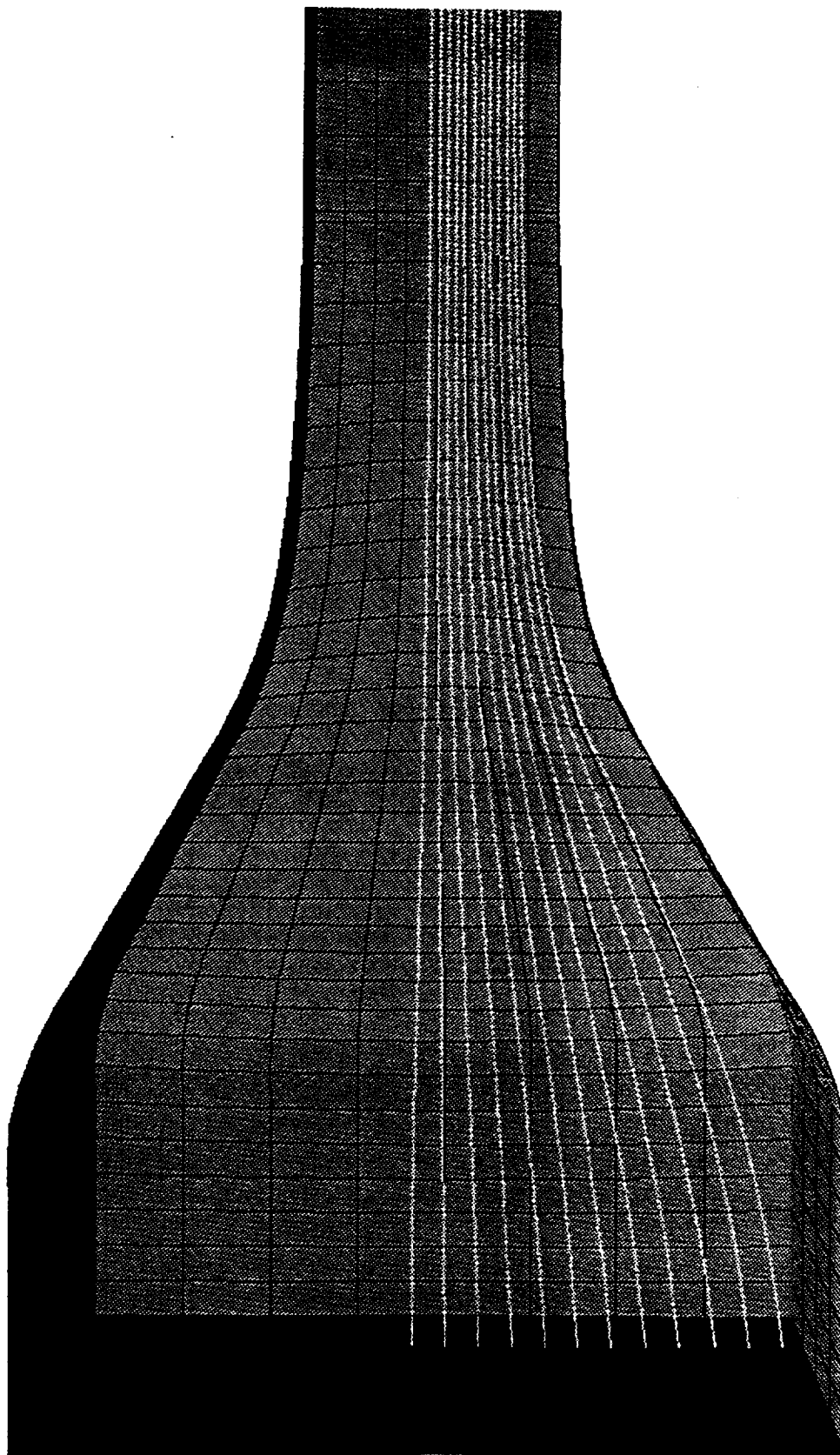
Figure 4.1 Water droplet trajectories computed from the IRT spray bar plane through the test section
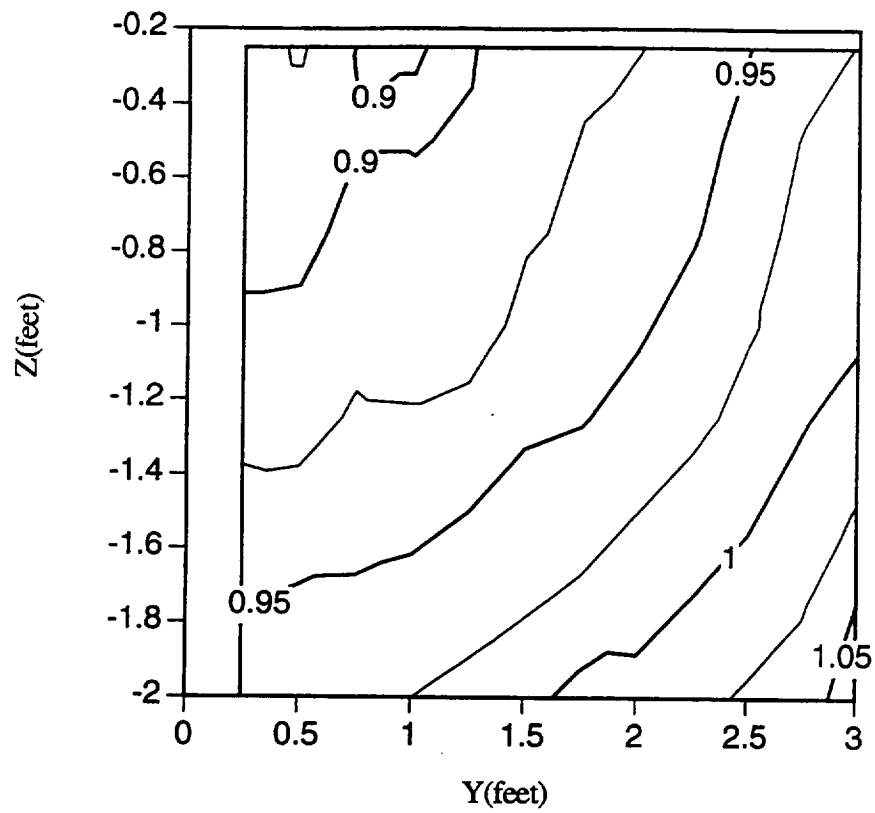
Figure 4.2   Computed relative LWC's in the test section of the IRT for test section velocity

of 150 mph and droplet size of 5.5 microns
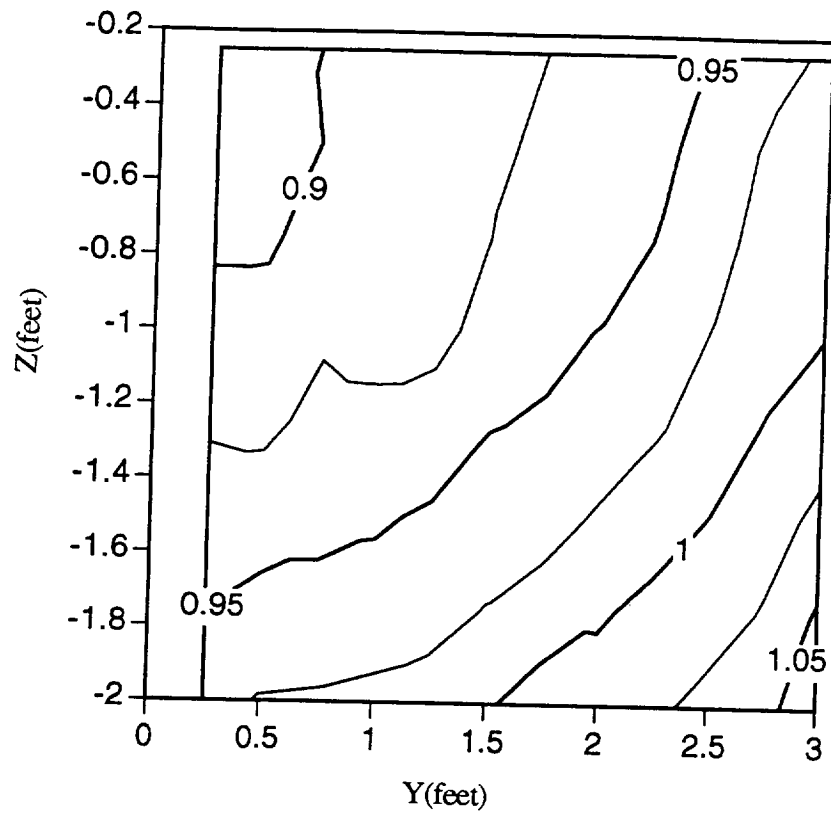
Figure 4.3 Computed relative LWC's in the test section of the IRT for test section velocity of 150 mph and droplet size of 8.9 microns
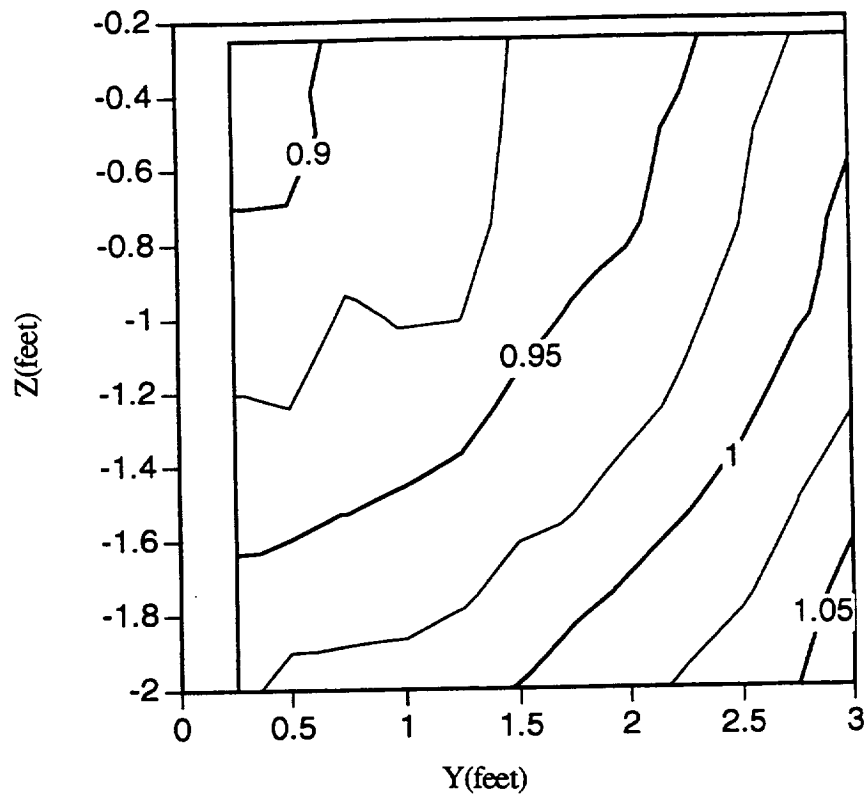
Figure 4.4 Computed relative LWC's in the test section of the IRT for test section velocity of 150 mph and droplet size of 13.2 microns
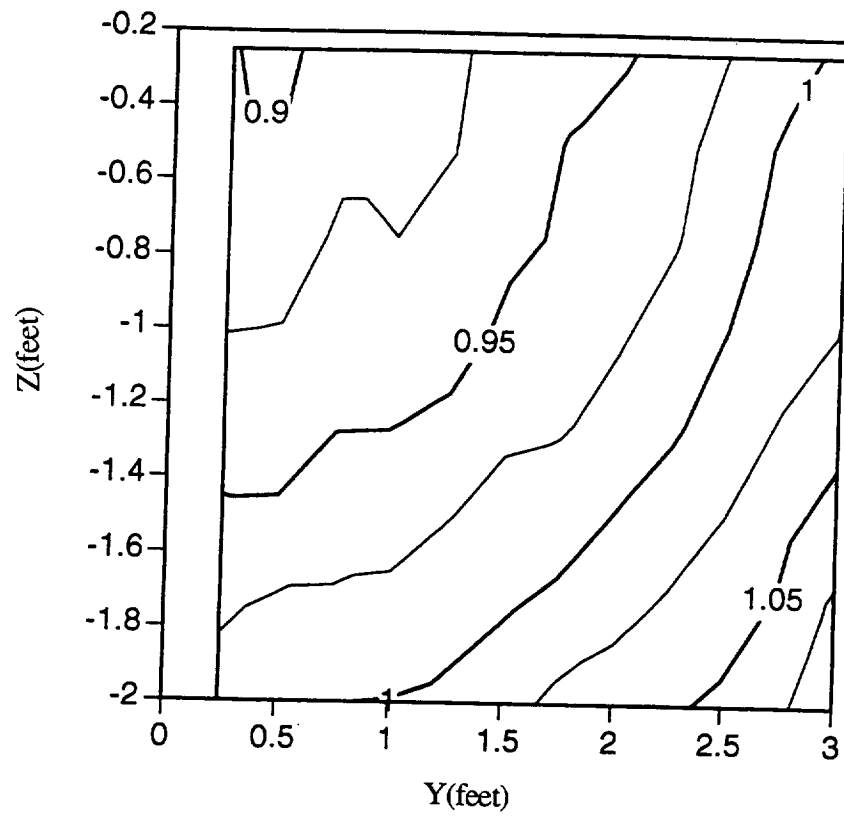
Figure 4.5   Computed relative LWC's in the test section of the IRT for test section velocity of 150 mph and droplet size of 20.0 microns
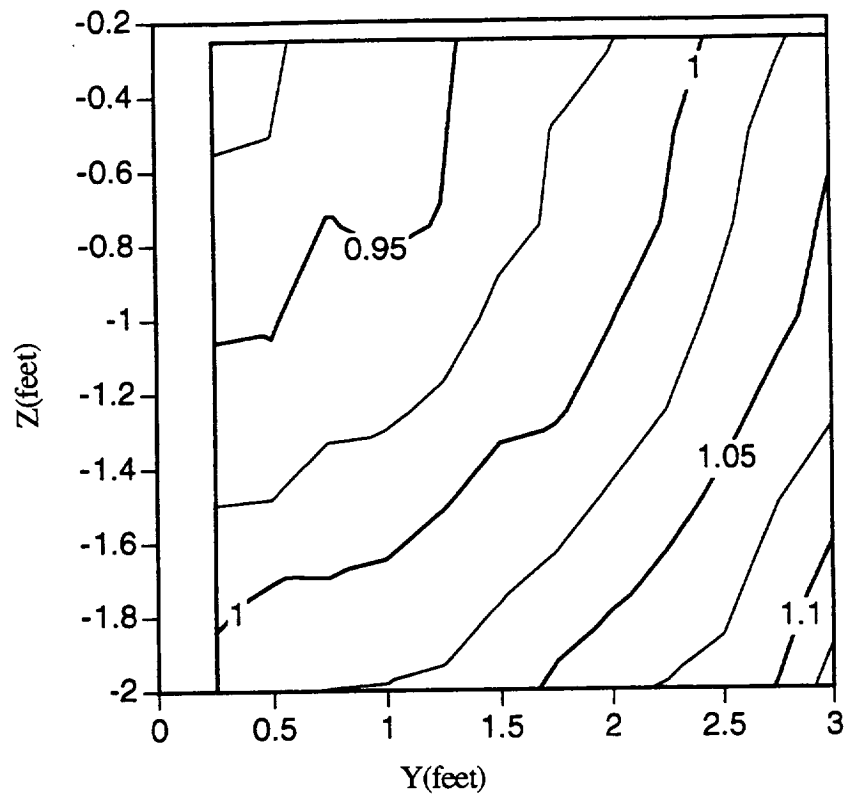
Figure 4.6 Computed relative LWC's in the test section of the IRT for test section velocity
of 150 mph and droplet size of 28.9 microns
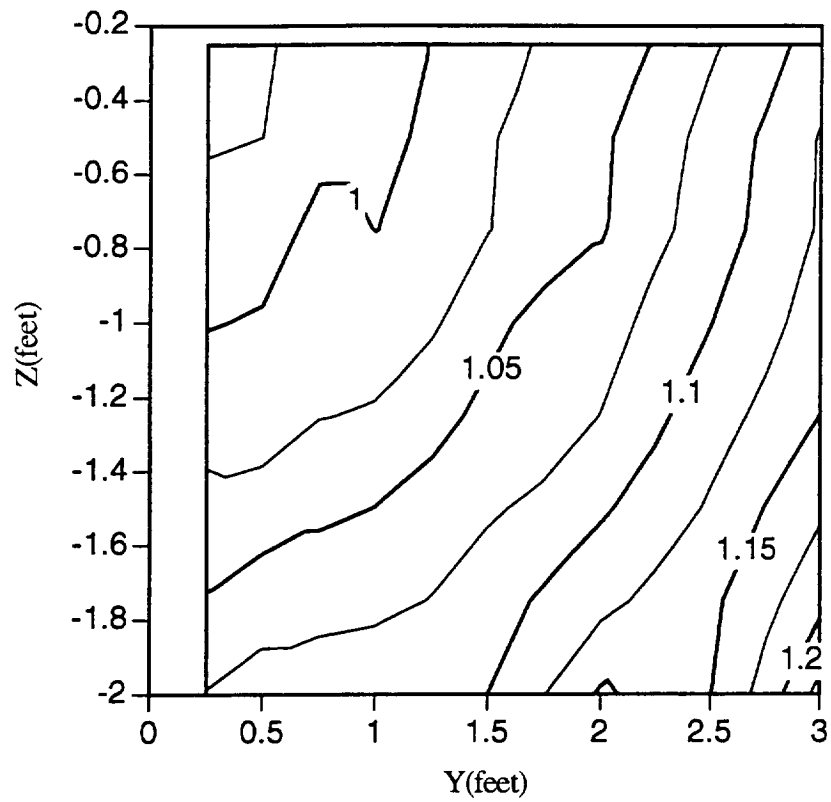
Figure 4.7 Computed relative LWC's in the test section of the IRT for test section velocity of 150 mph and droplet size of 45.9 microns
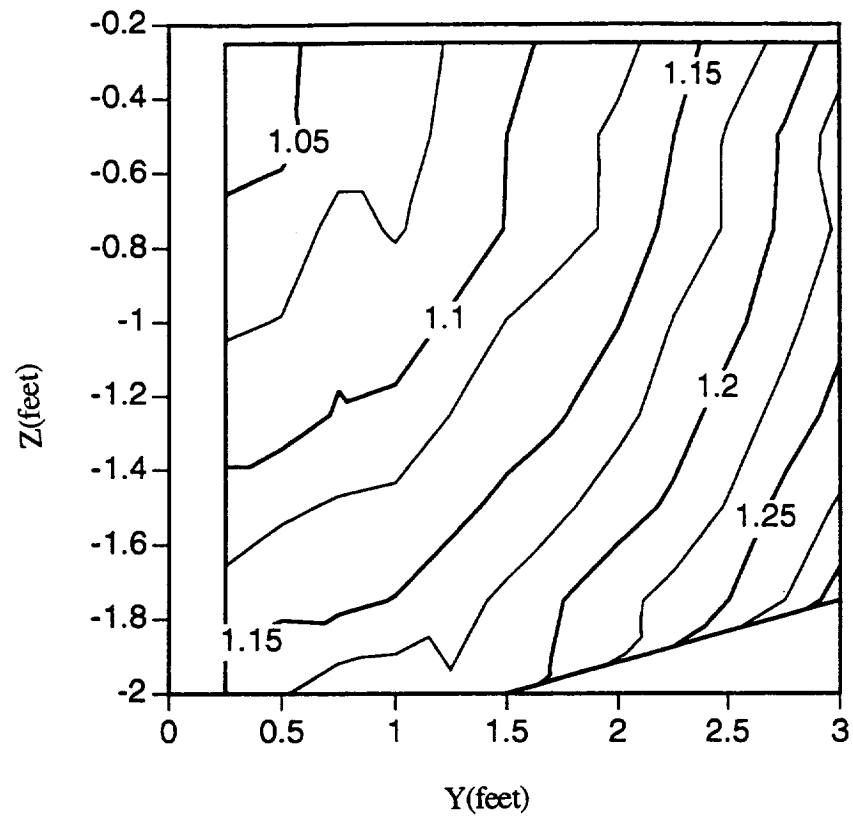
Figure 4.8   Computed relative LWC's in the test section of the IRT for test section velocity

of 150 mph and droplet size of 65.1 microns
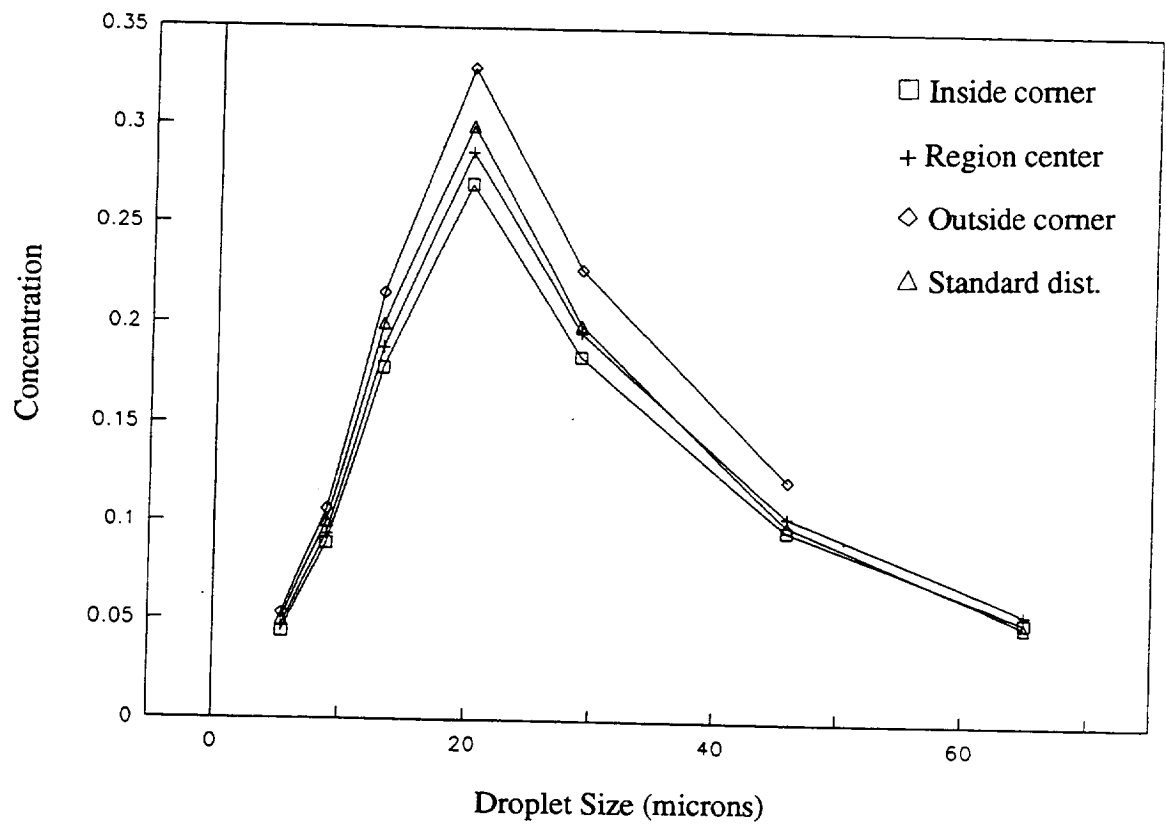
Figure 4.9 Water concentration versus droplet size in the test section of the IRT for test section velocity of 150 mph
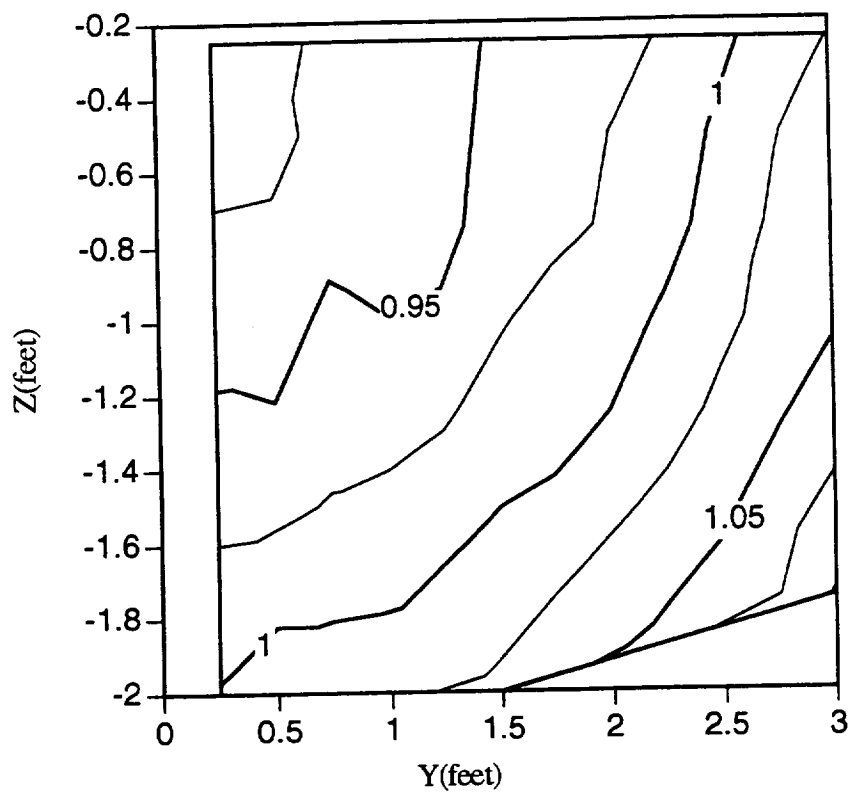
Figure 4.10 Effective LWC in test section of the IRT for test section velocity of 150 mph
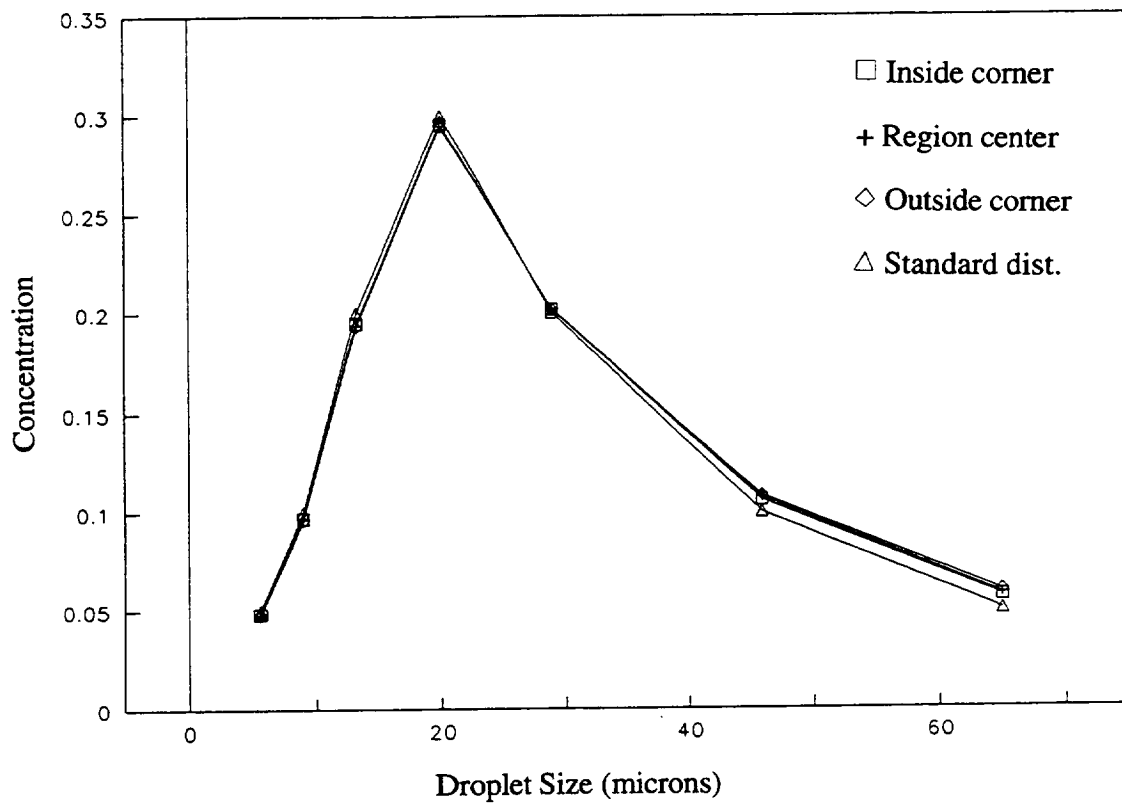
Figure 4.11 Non-dimensionalized water concentration versus droplet size in test section of the IRT for test section velocity of 150 mph
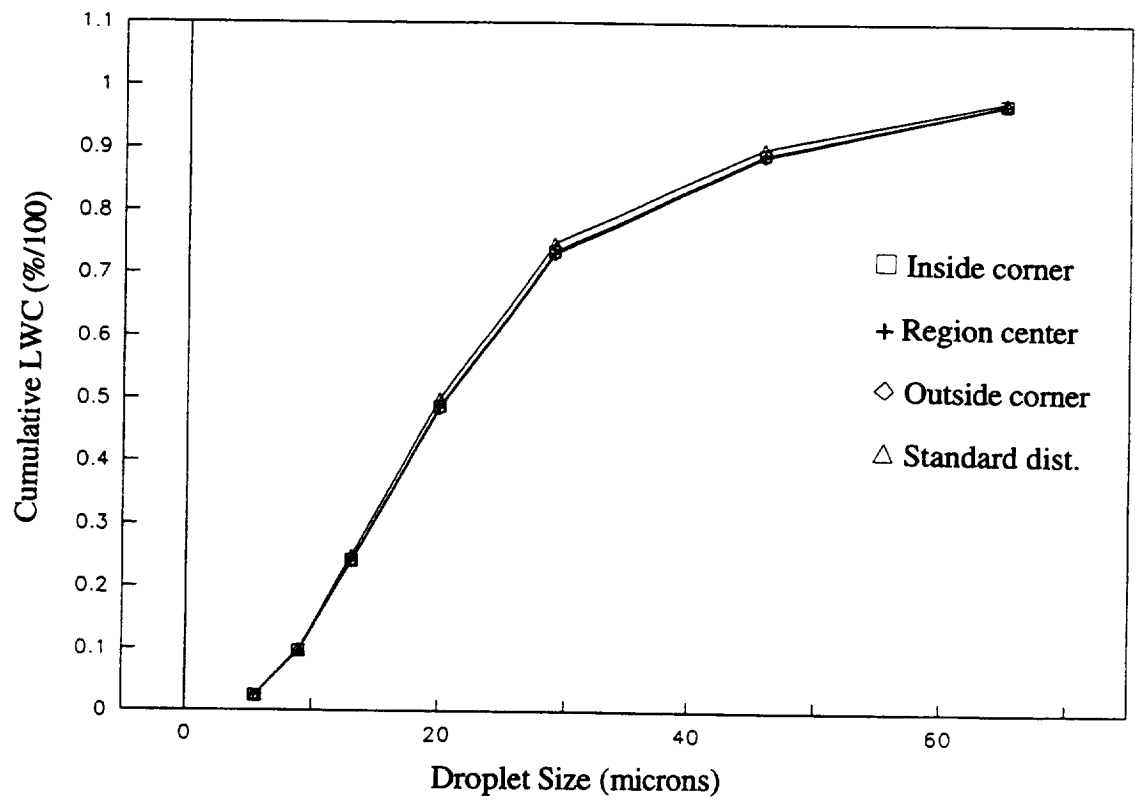
Figure 4.12 Cumulative LWC versus droplet size in test section of the IRT for test section velocity of 150 mph
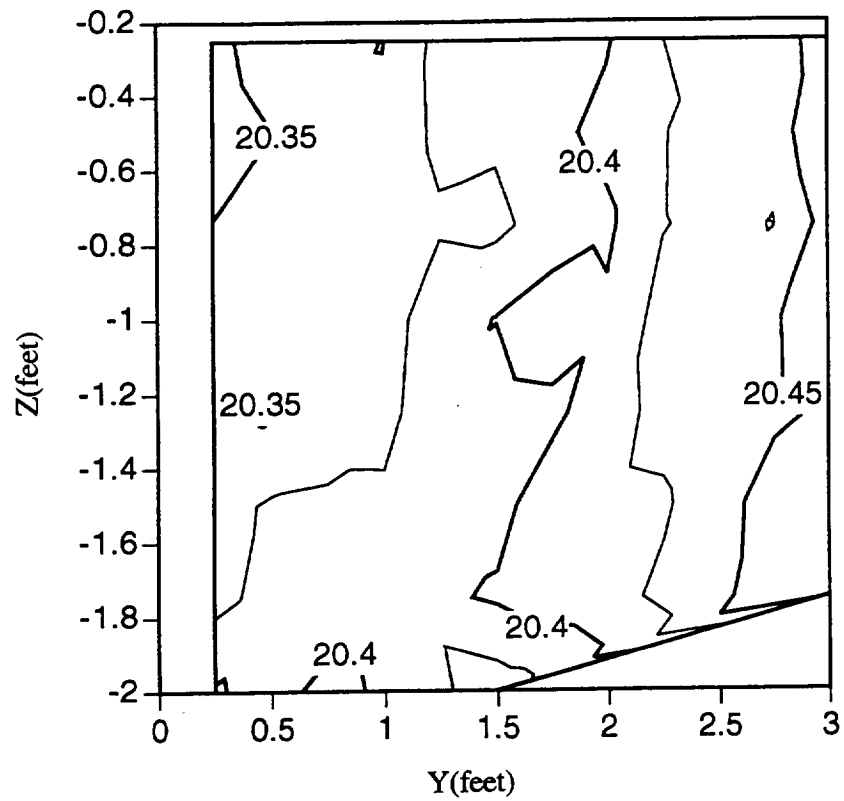
Figure 4.13 Effective MVD in test section of the IRT for test section velocity of 150 mph
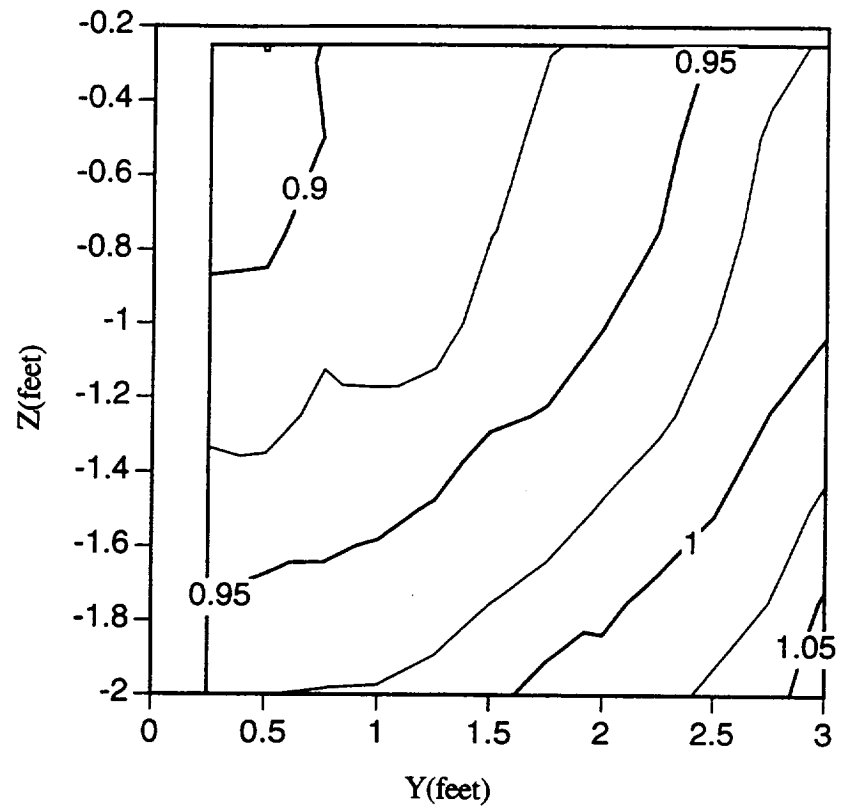
Figure 4.14 Computed relative LWC's in the test section of the IRT for test section velocity of 300 mph and droplet size of 5.5 microns
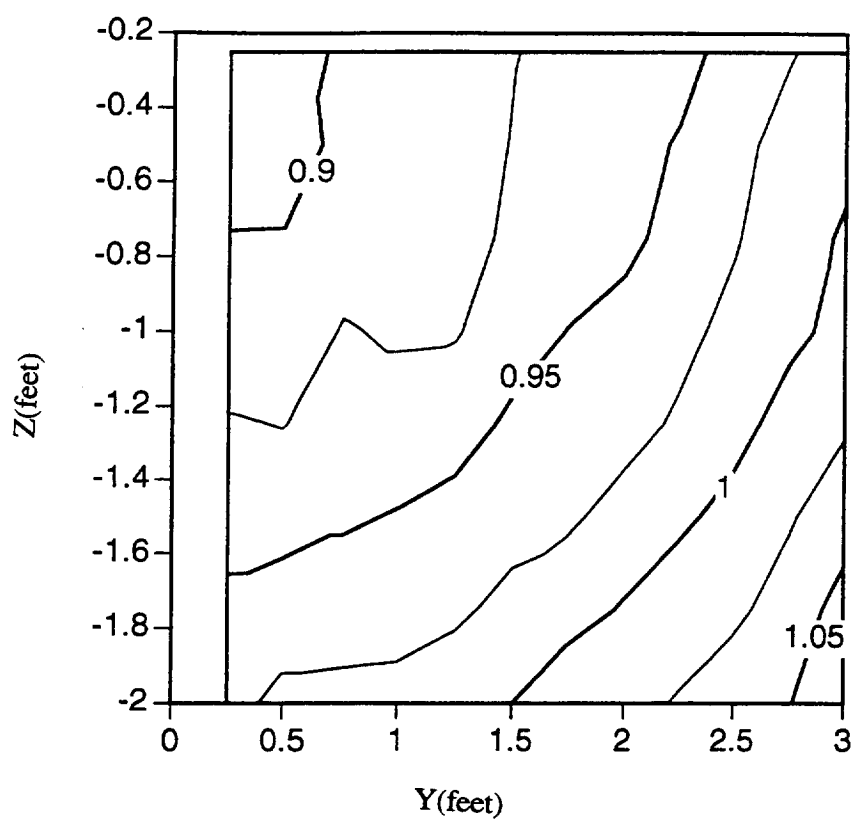
Figure 4.15 Computed relative LWC's in the test section of the IRT for test section velocity of 300 mph and droplet size of 8.9 microns
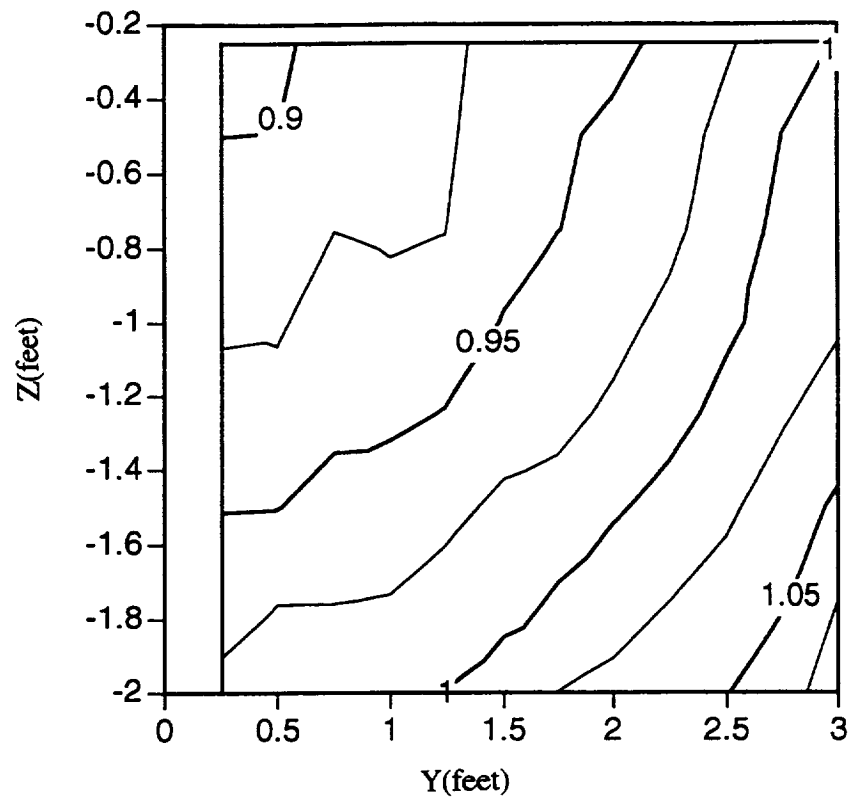
Figure 4.16 Computed relative LWC's in the test section of the IRT for test section

velocity of 300 mph and droplet size of 13.2 microns
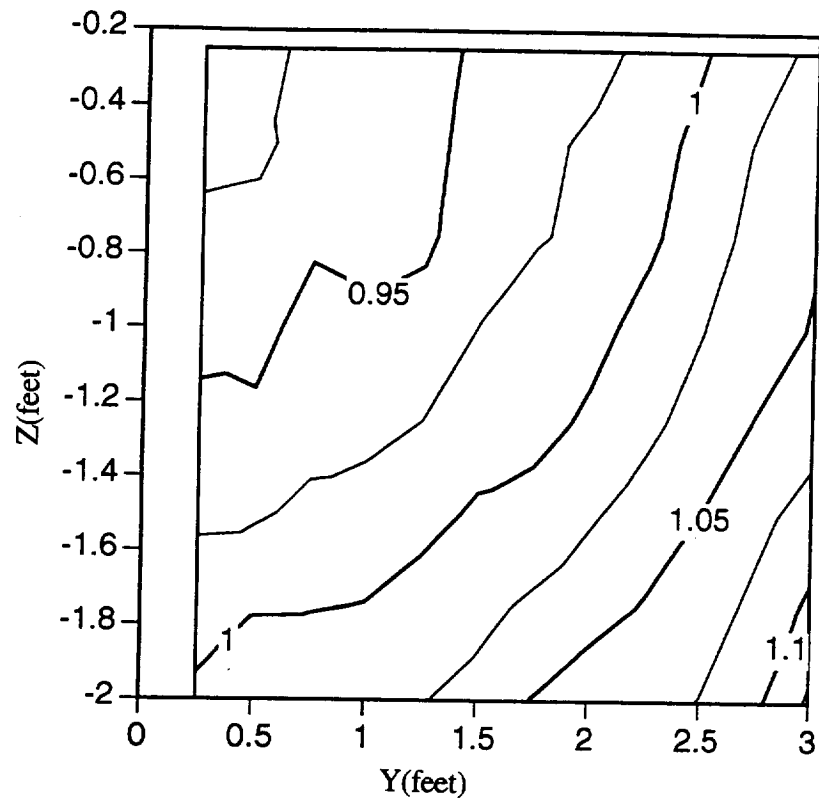
Figure 4.17 Computed relative LWC's in the test section of the IRT for test section velocity of 300 mph and droplet size of 20.0 microns
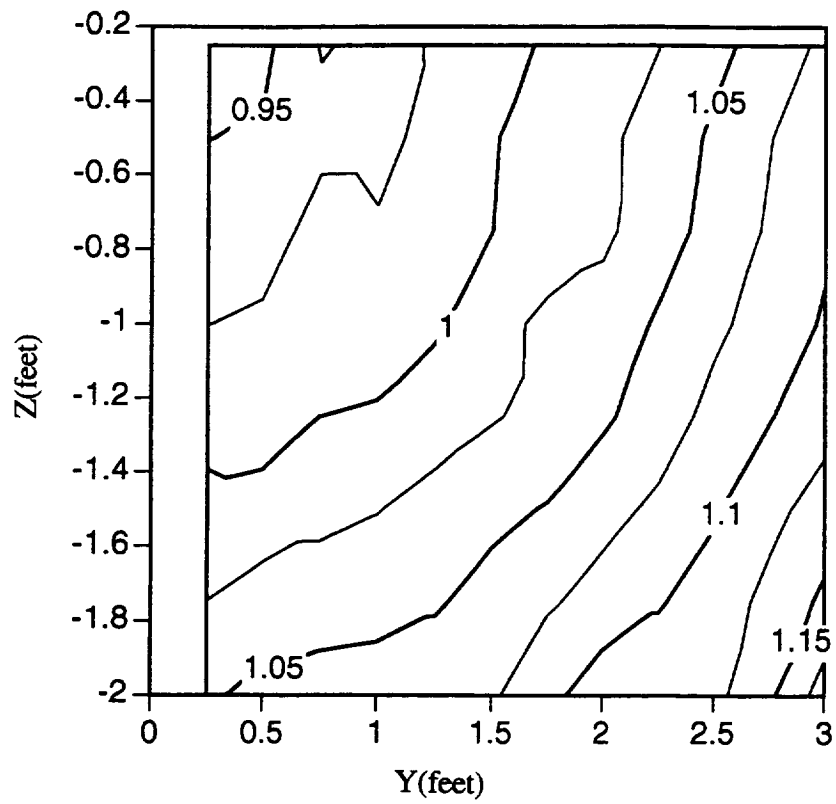
Figure 4.18 Computed relative LWC's in the test section of the IRT for test section

velocity of 300 mph and droplet size of 28.9 microns
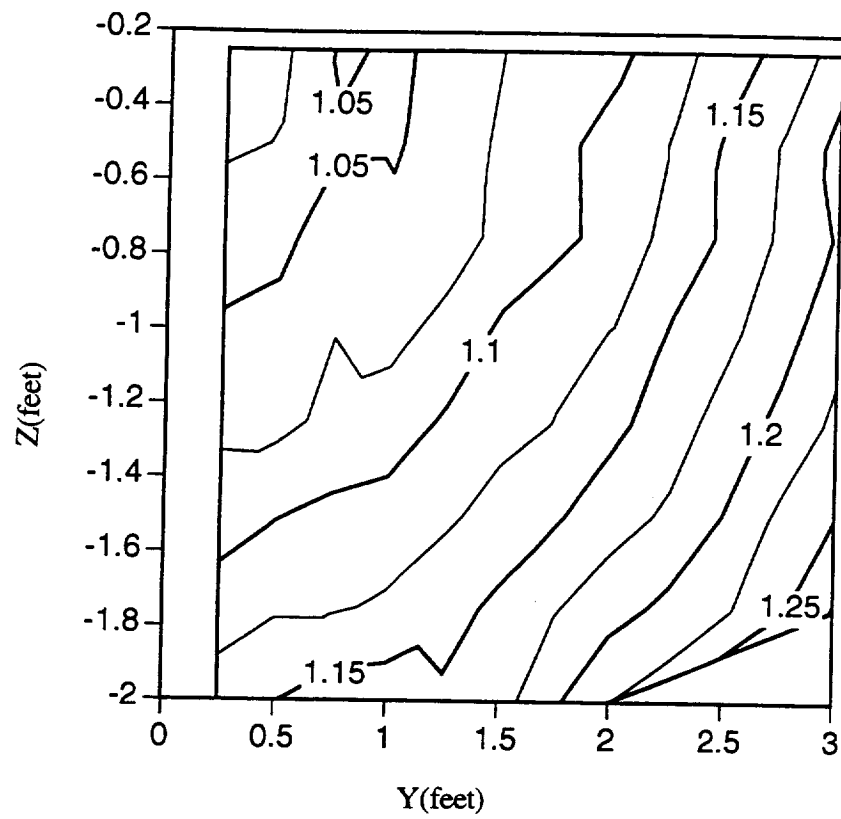
Figure 4.19 Computed relative LWC's in the test section of the IRT for test section

velocity of 300 mph and dropletsize of 45.9 microns
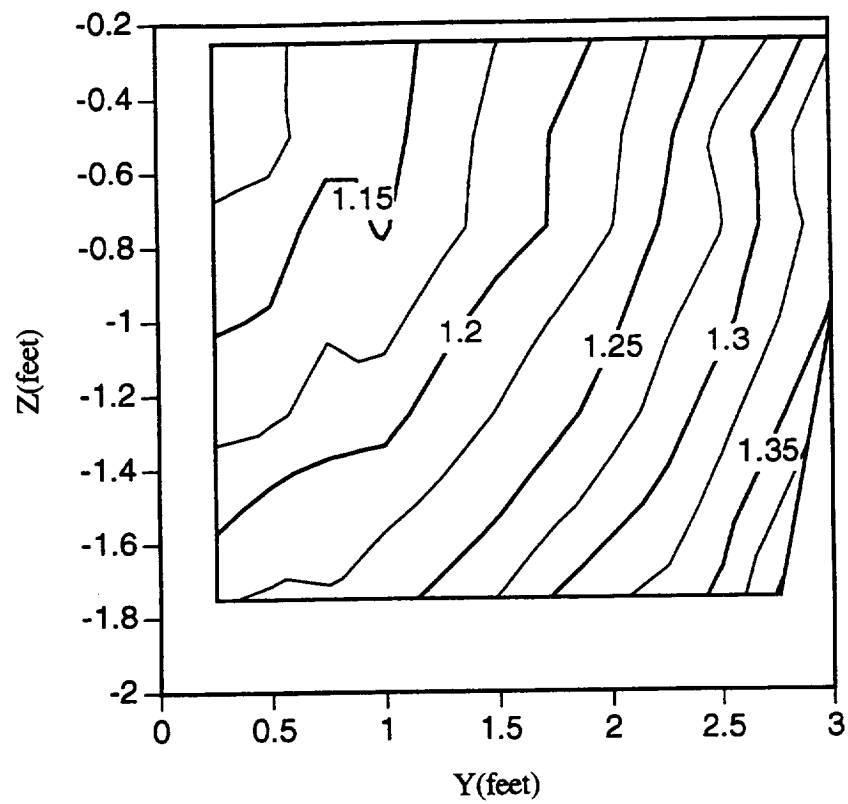
Figure 4.20 Computed relative LWC's in the test section of the IRT for test section

velocity of 300 mph and droplet size of 65.1 microns
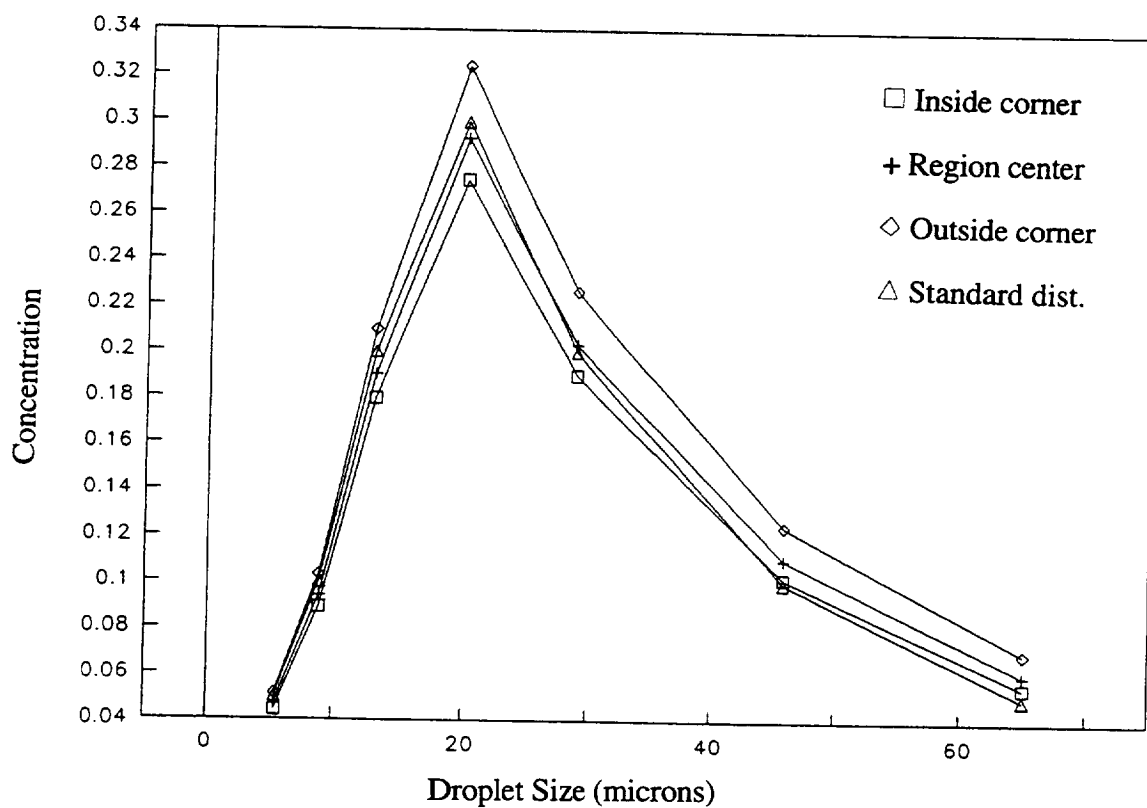
Figure 4.21 Water concentration versus droplet size in the test section of the IRT for test section velocity of 300 mph
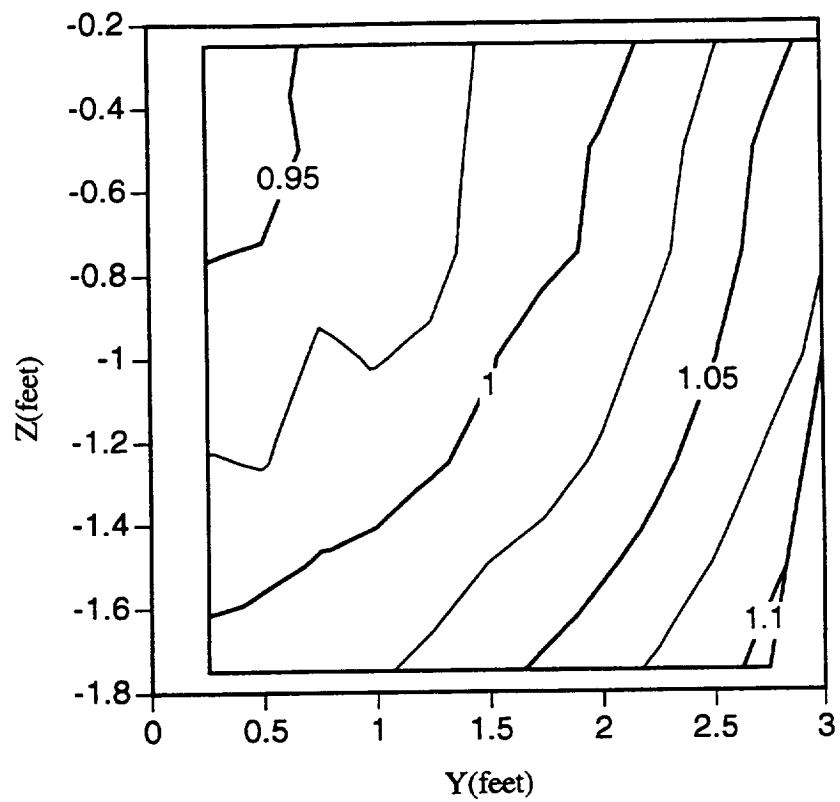
Figure 4.22 Effective LWC in test section of the IRT for test section velocity of 300 mph
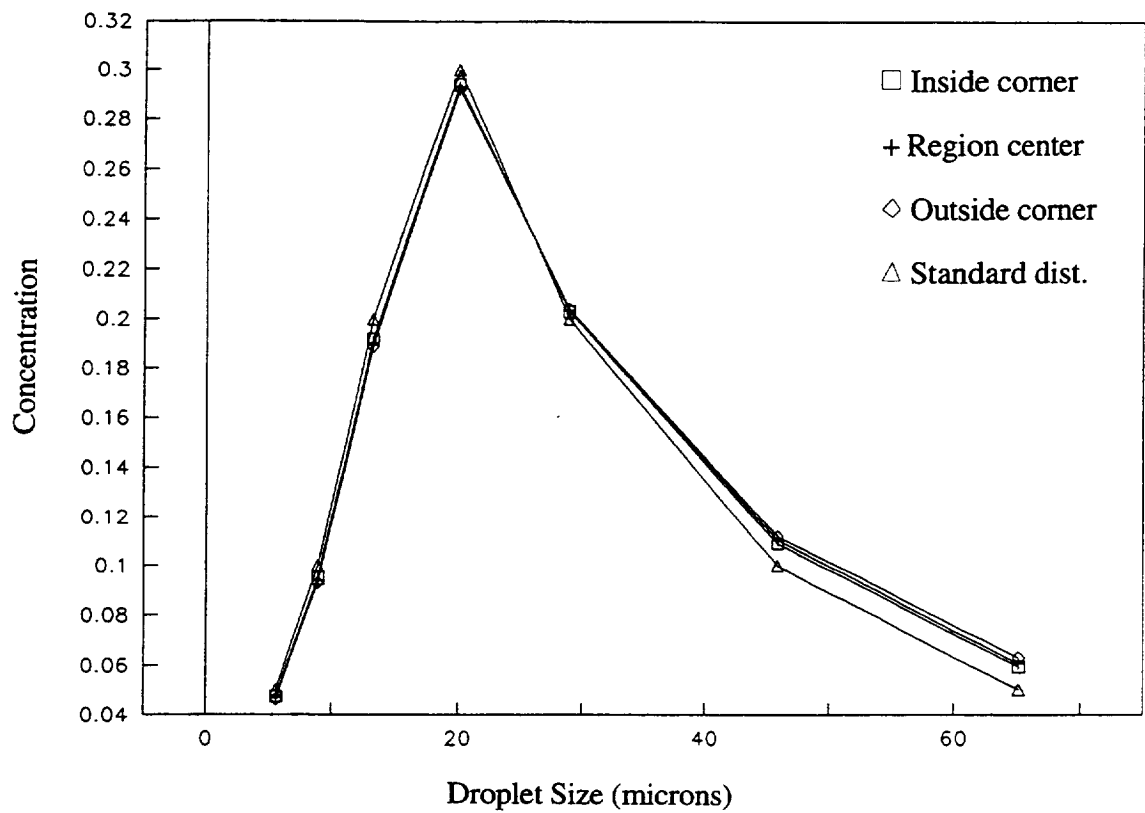
Figure 4.23 Non-dimensionalized water concentration versus droplet size in test section of the IRT for test section velocity of 300 mph
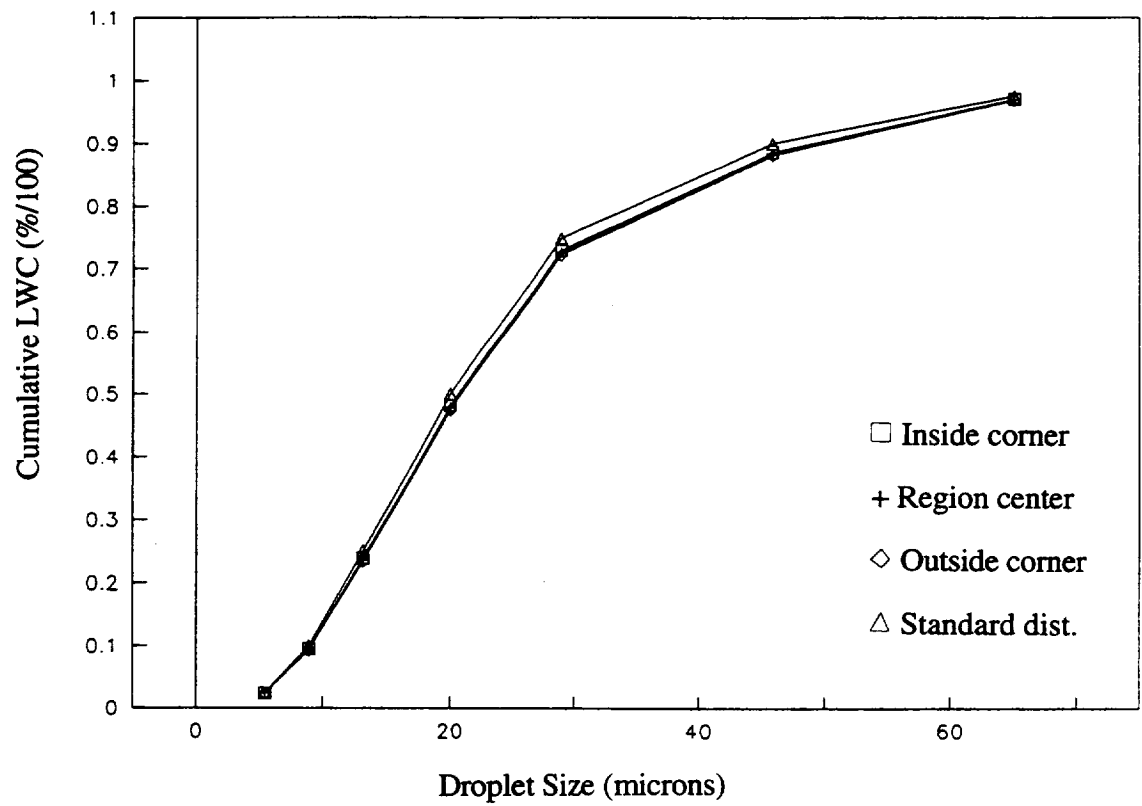
Figure 4.24 Cumulative LWC versus droplet size in test section of the IRT for test section velocity of 300 mph
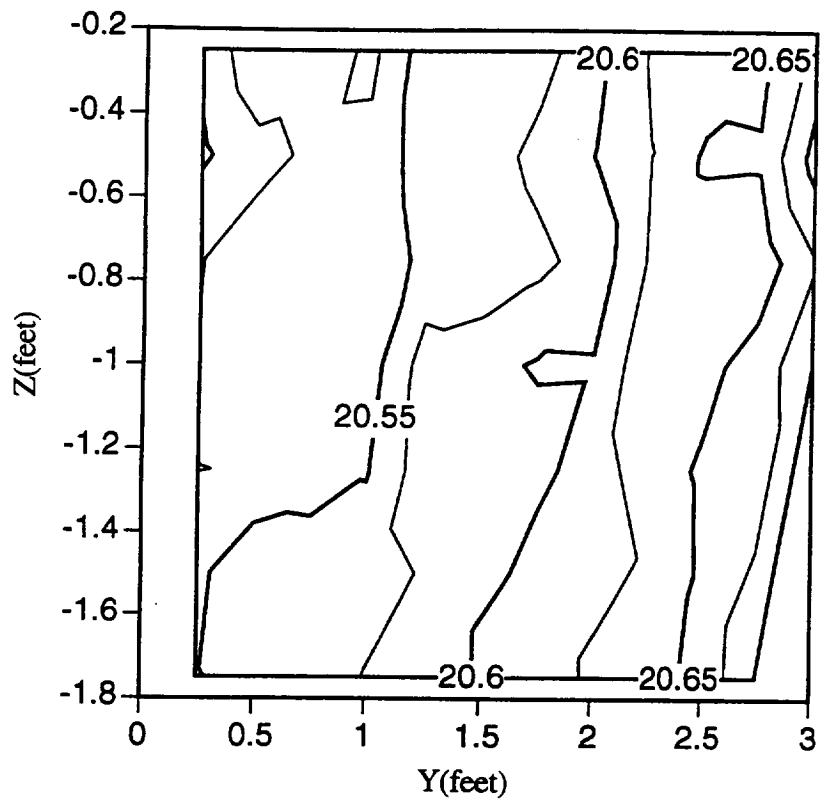
Figure 4.25 Effective MVD in test section of the IRT for test section velocity of 300 mph
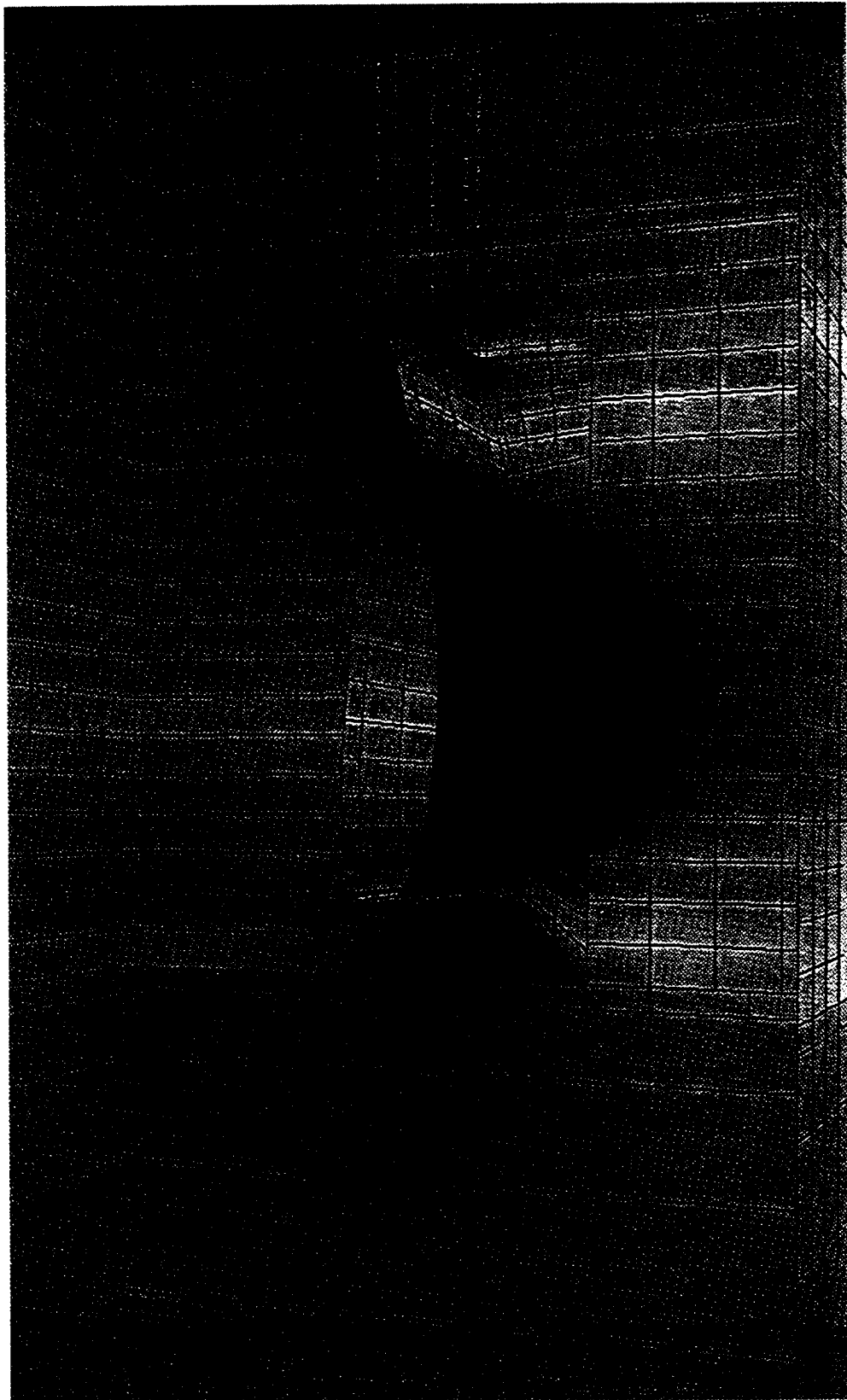
Figure 4.26 Pressure distribution on IRT and Twin Otter wing at 0 degrees angle of attack
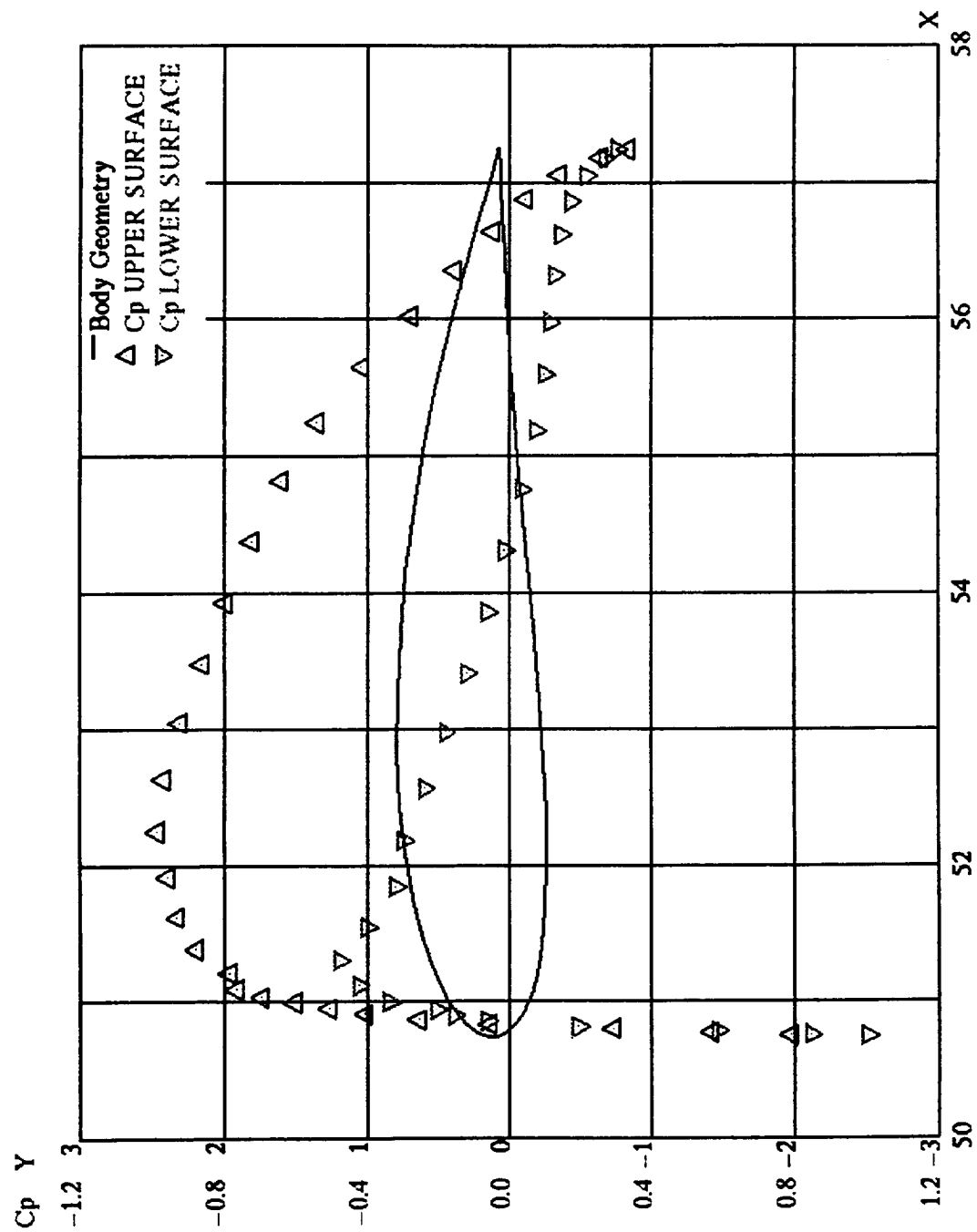
Figure 4.27 Pressure distribution on installed Twin Otter wing at 0 degrees angle of attack

141

Figure 4.28 Pressure distribution on IRT and Twin Otter wing at 4 degrees angle of attack
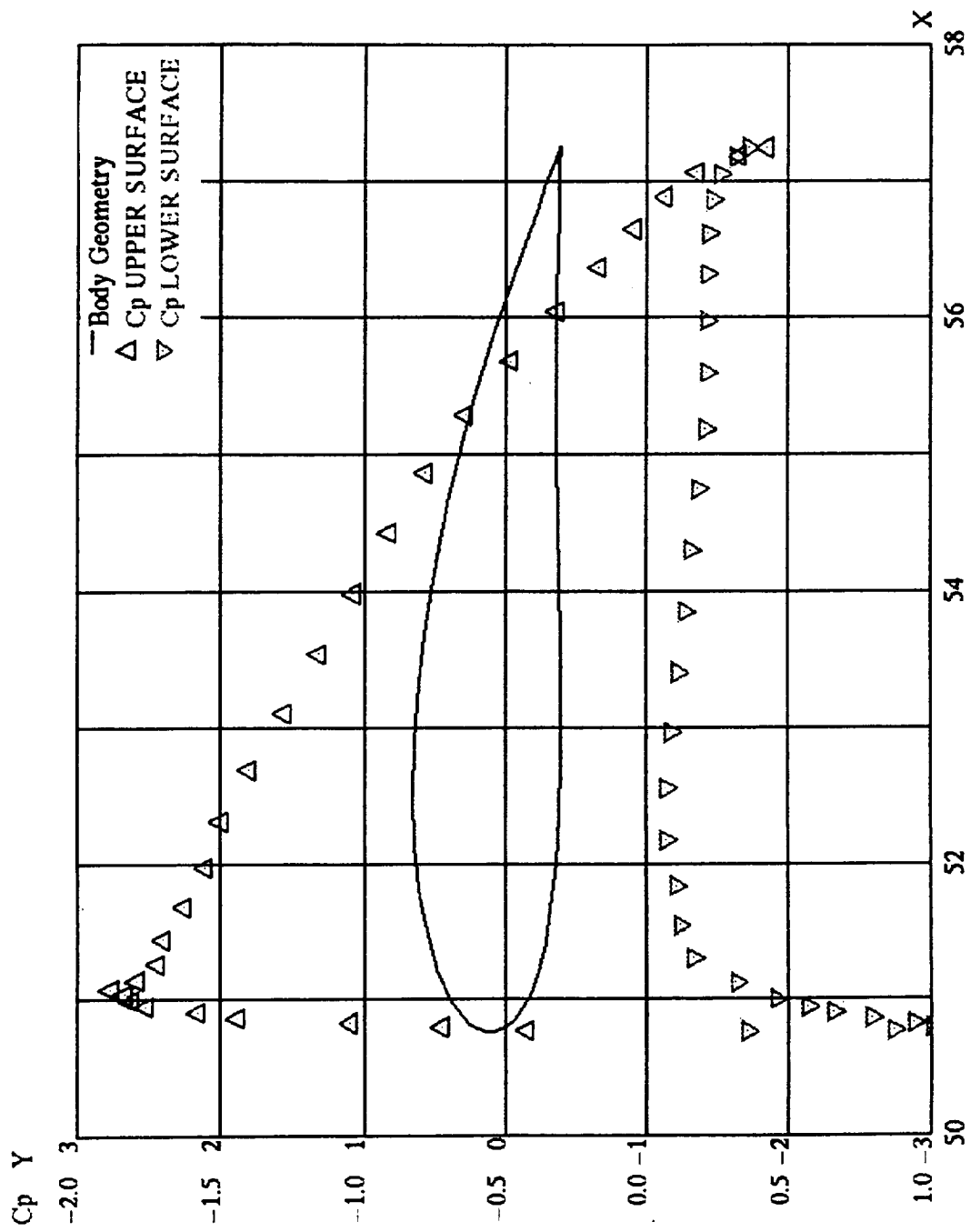
Figure 4.29 Pressure distribution on installed Twin Otter wing at 4 degrees angle of attack

143
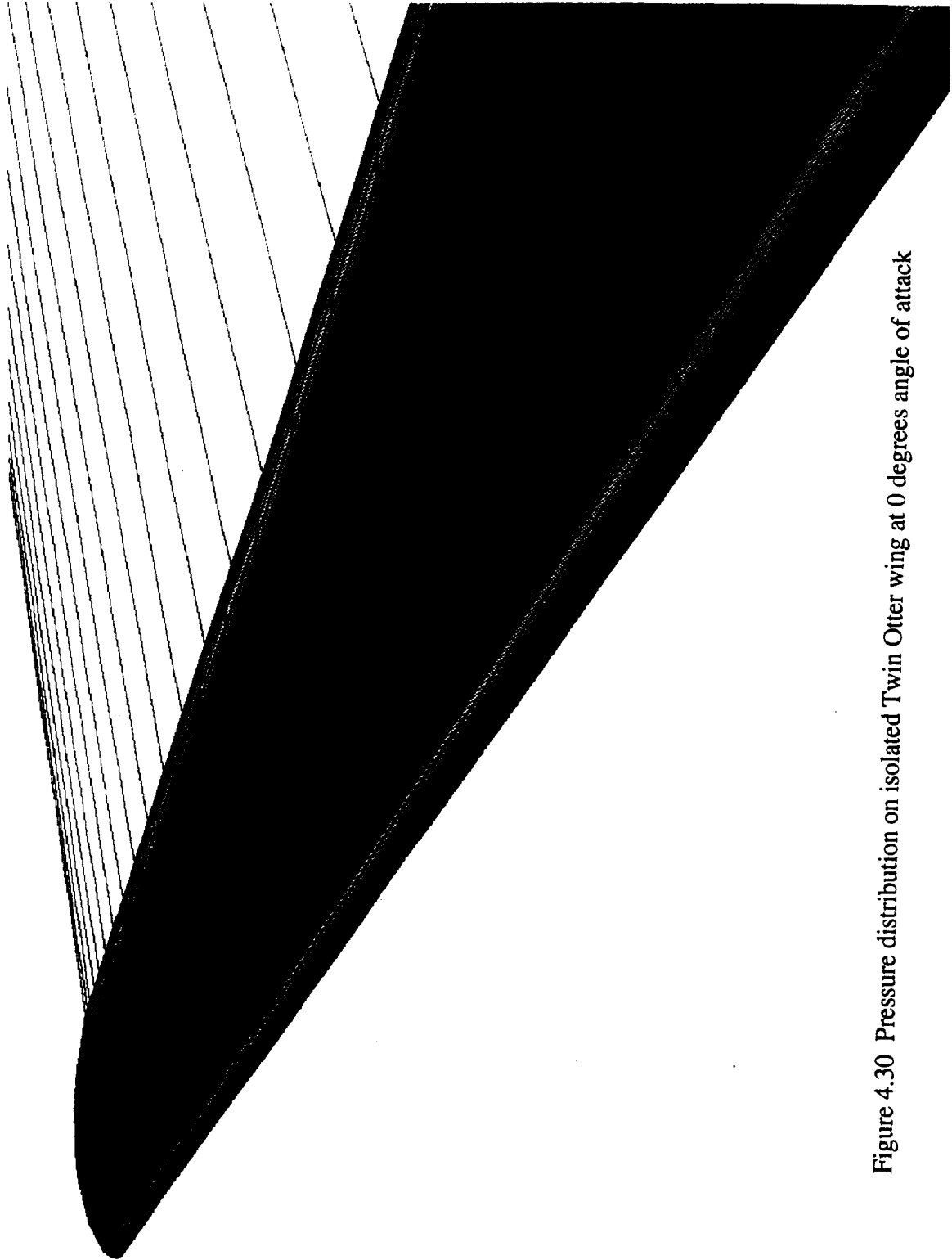
Figure 4.30 Pressure distribution on isolated Twin Otter wing at 0 degrees angle of attack
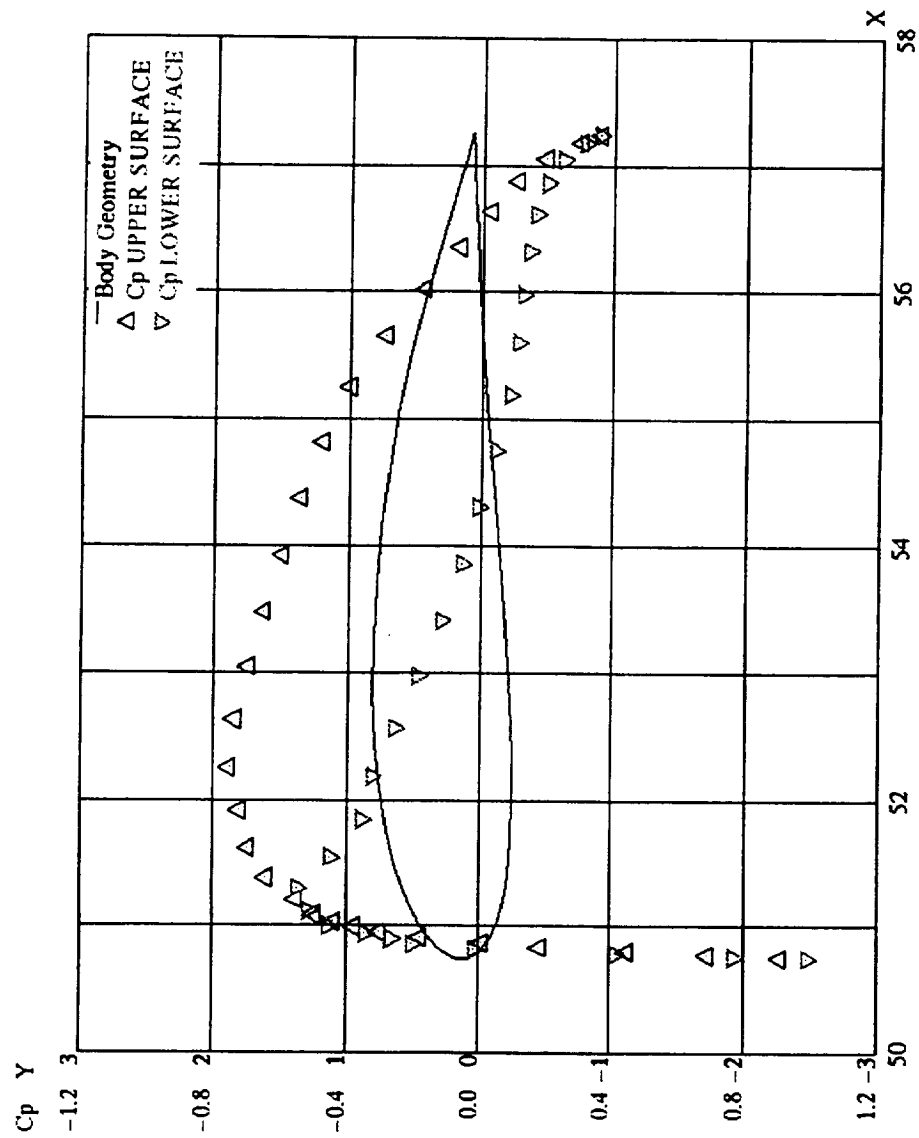
Figure 4.31 Pressure distribution on isolated Twin Otter wing at 0 degrees angle of attack
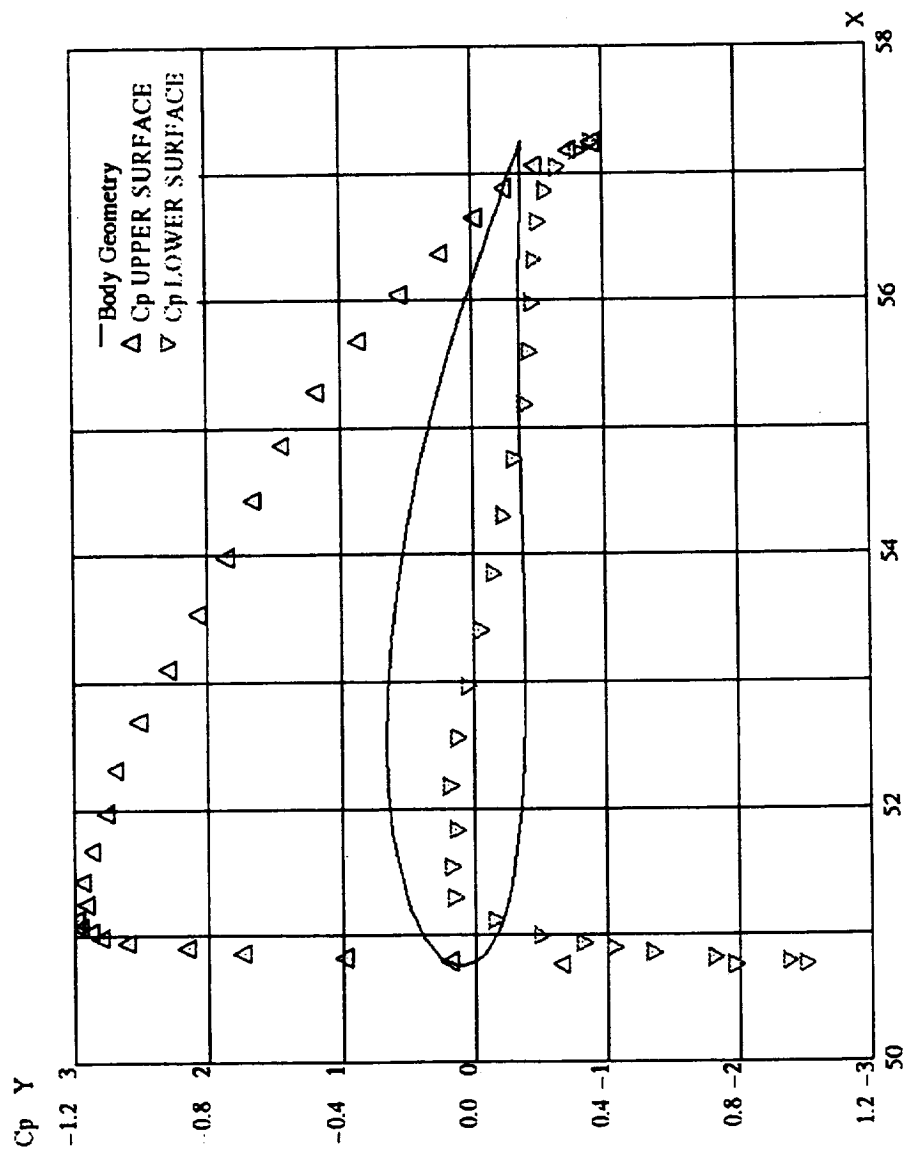
Figure 4.32 Pressure distribution on isolated Twin Otter wing at 4 degrees angle of attack
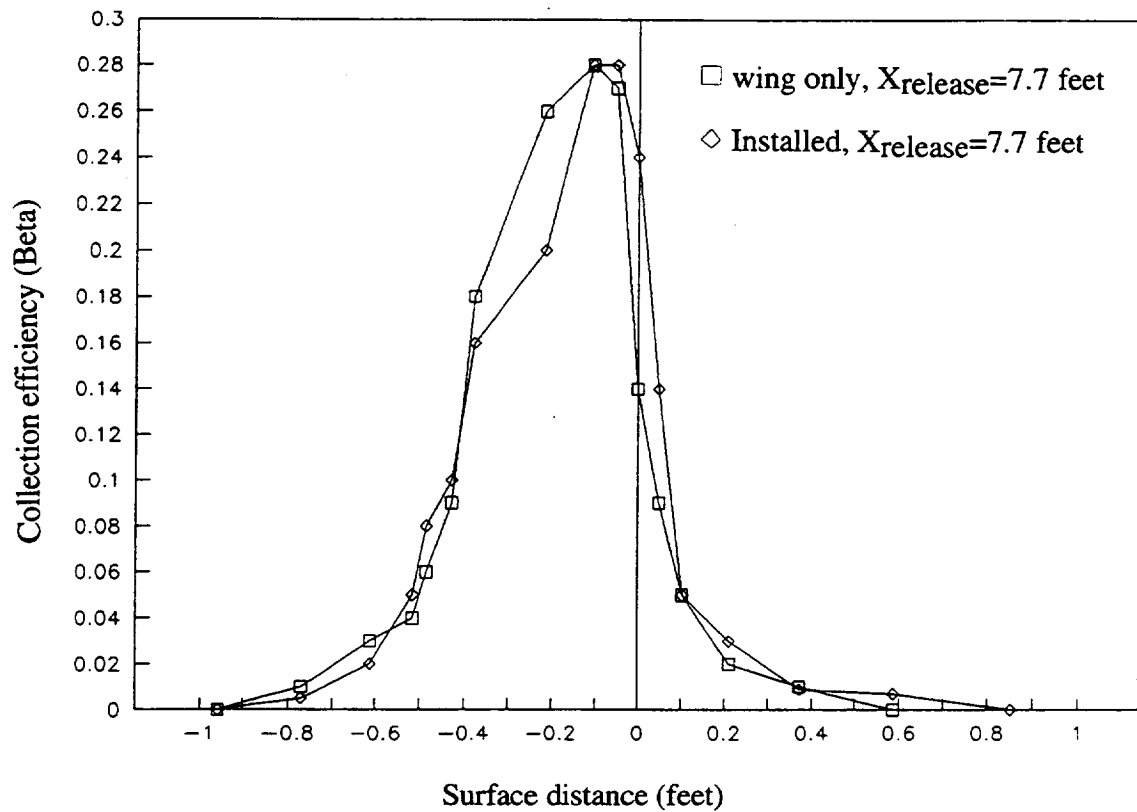
Figure 4.33 Water droplet collection efficiency on the Twin Otter wing both installed in the IRT and isolated at 4 degrees angle of attack for 20 micron MVD droplet distribution

147
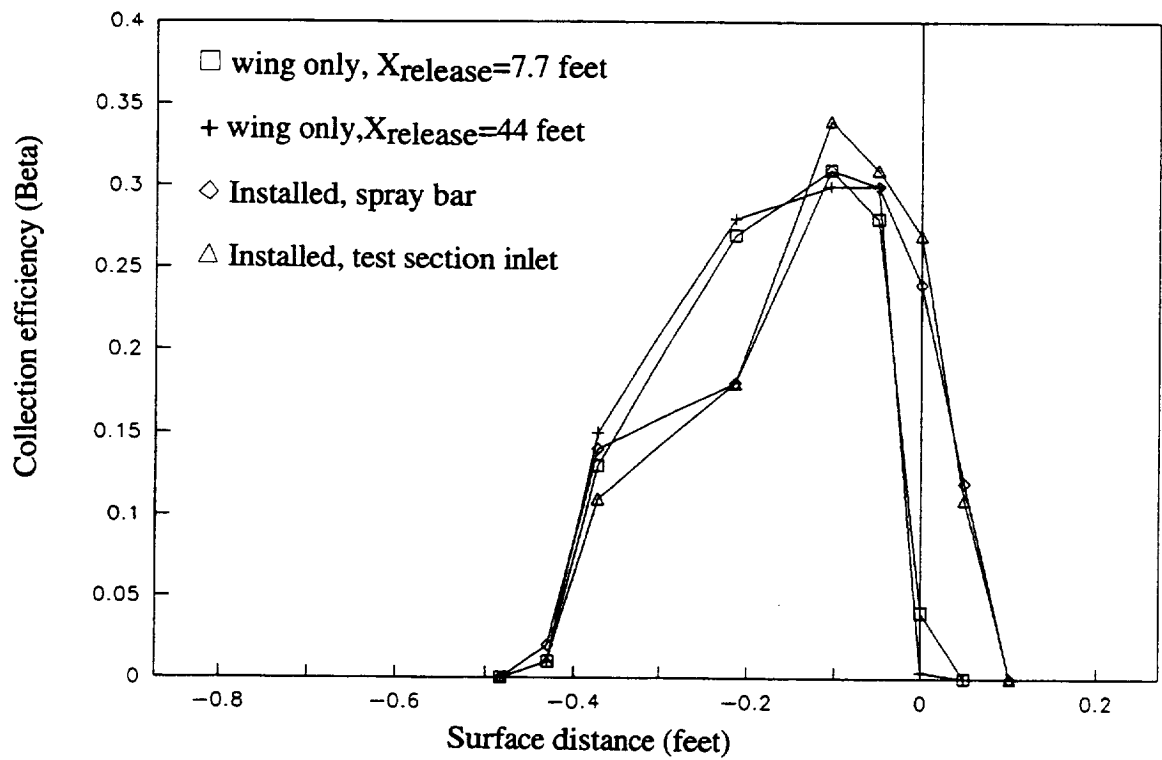
Figure 4.34 Water droplet collection efficiency on the Twin Otter wing both installed in the IRT and isolated with release points at 7.7 and 44.0 feet at 4 degrees angle of attack for 20 micron droplets
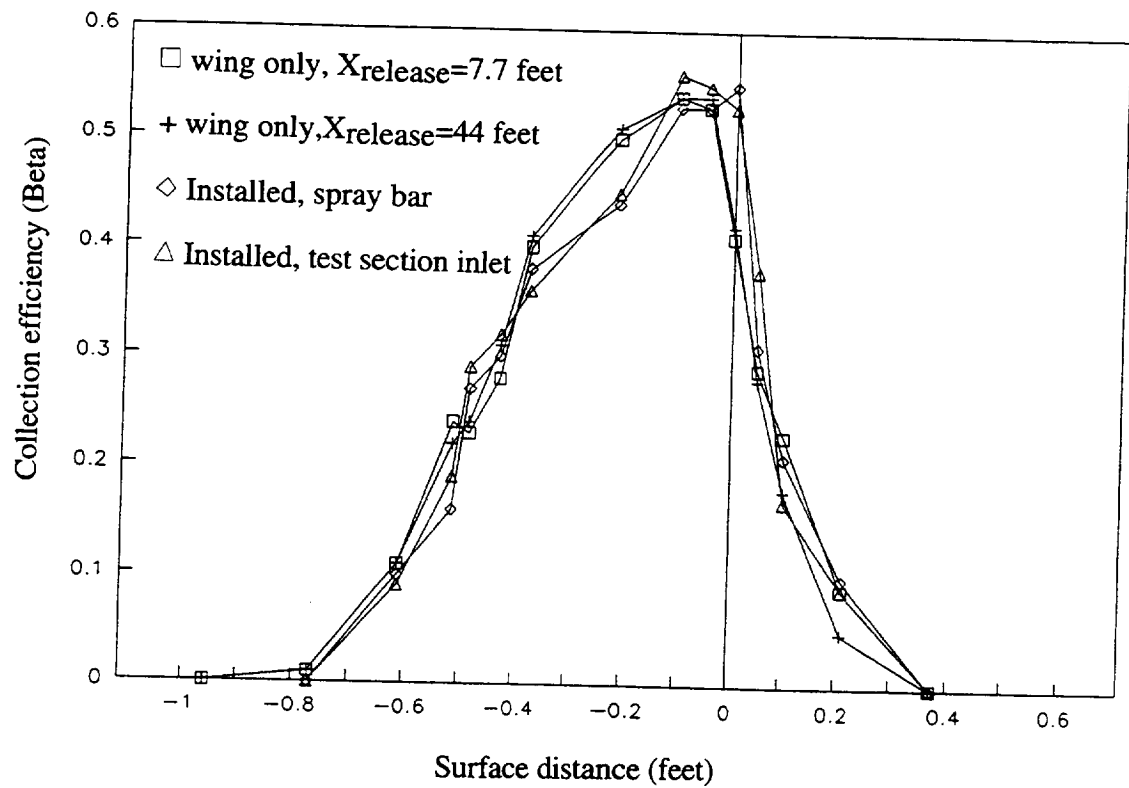
Figure 4.35 Water droplet collection efficiency on the Twin Otter wing both installed in the

IRT and isolated with release points at 7.7 and 44.0 feet at 4 degrees angle of attack for 40

micron droplets
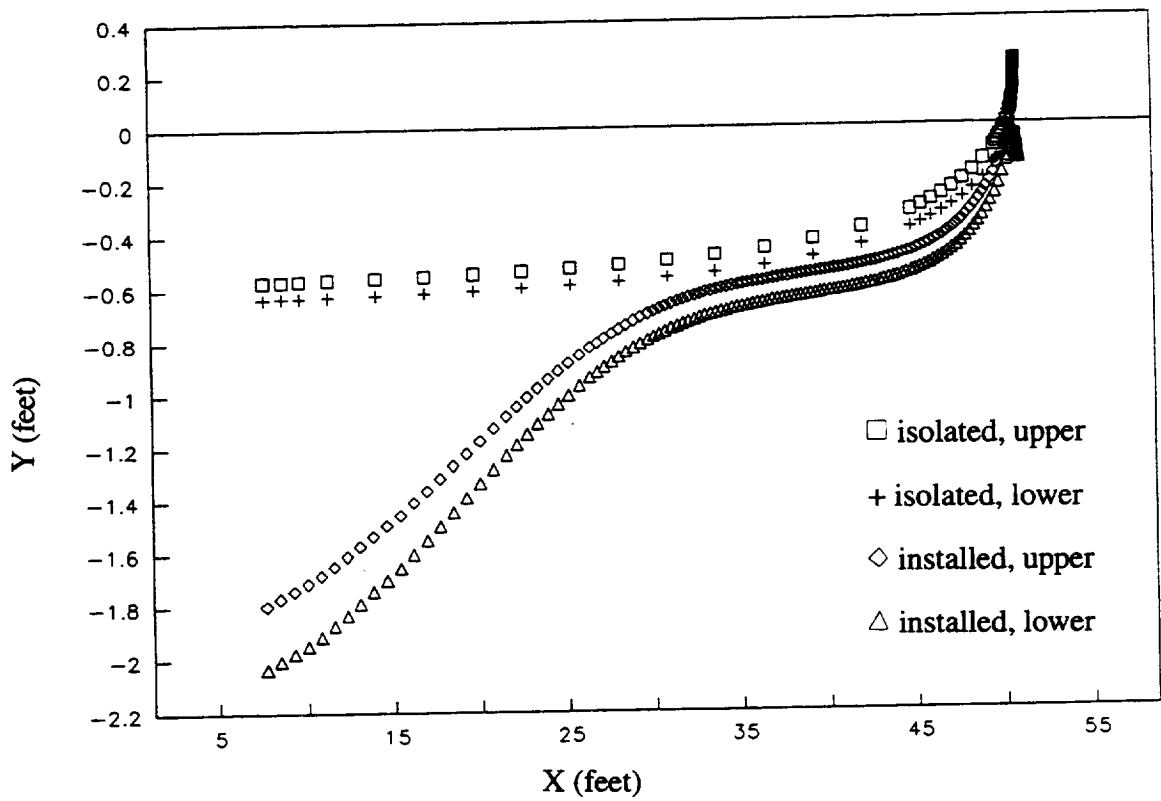
Figure 4.36 Impingement Trajectories for installed and isolated Twin Otter wing for 4 degrees angle of attack and 20 micron droplets
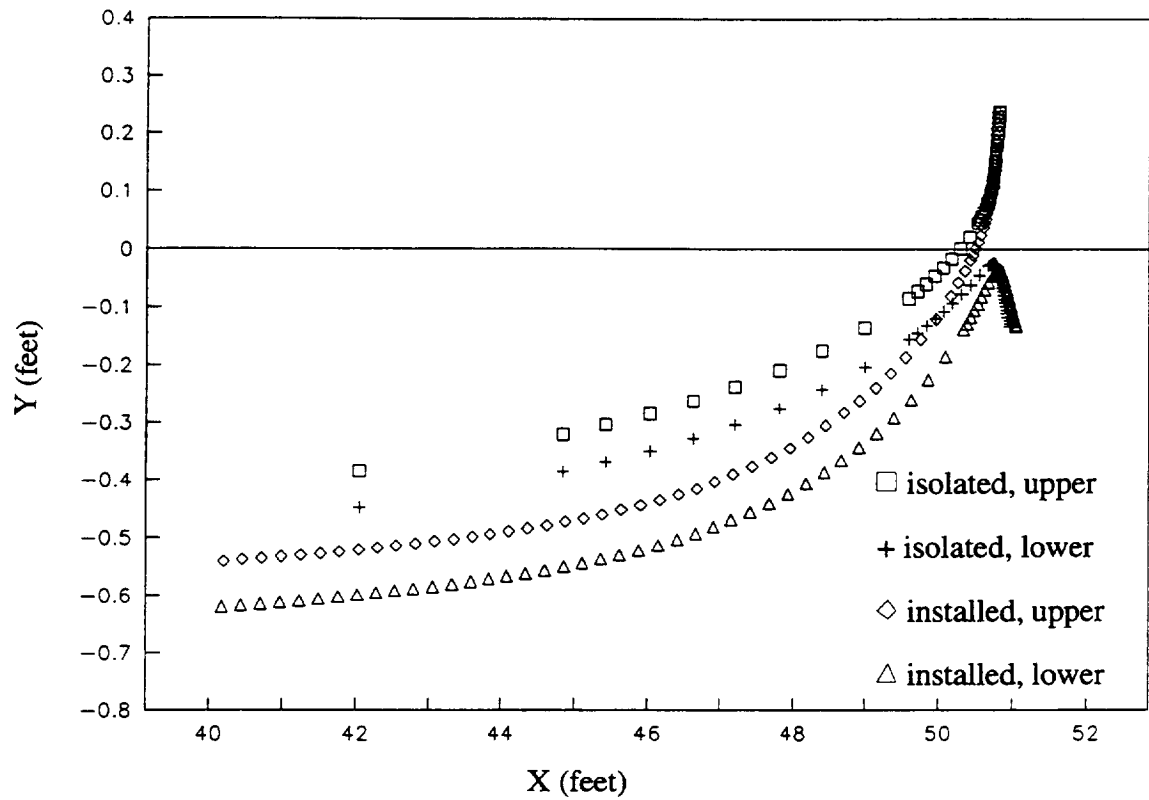
Figure 4.37 A close-up of Figure 4.36
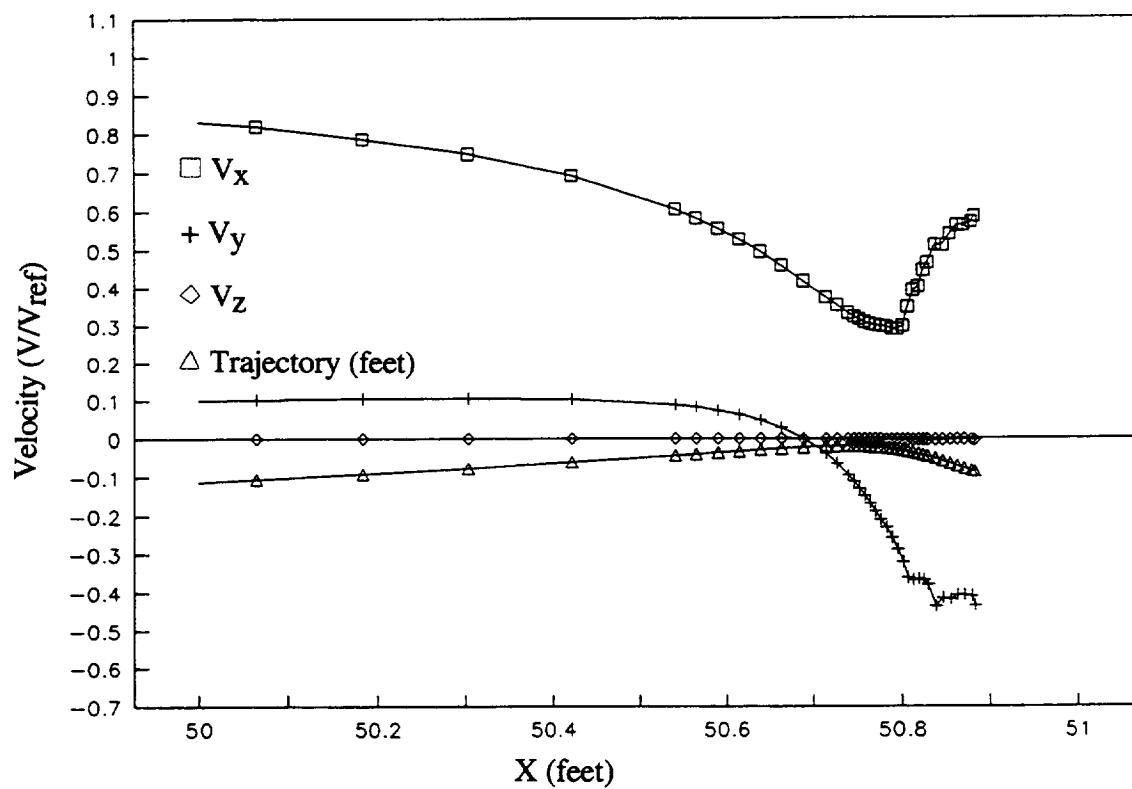
Figure 4.38 Flow velocities along a particle trajectory for the isolated Twin Otter wing
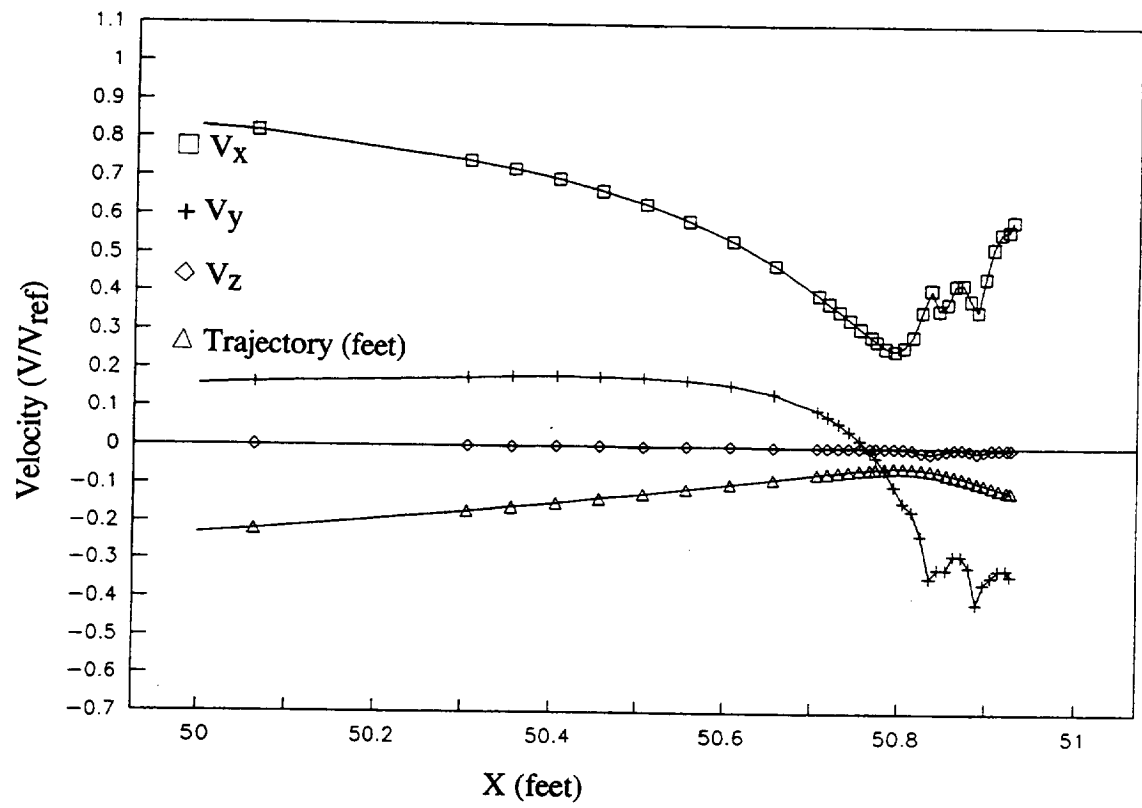
Figure 4.39 Flow velocities along a particle trajectory for the installed Twin Otter wing

153
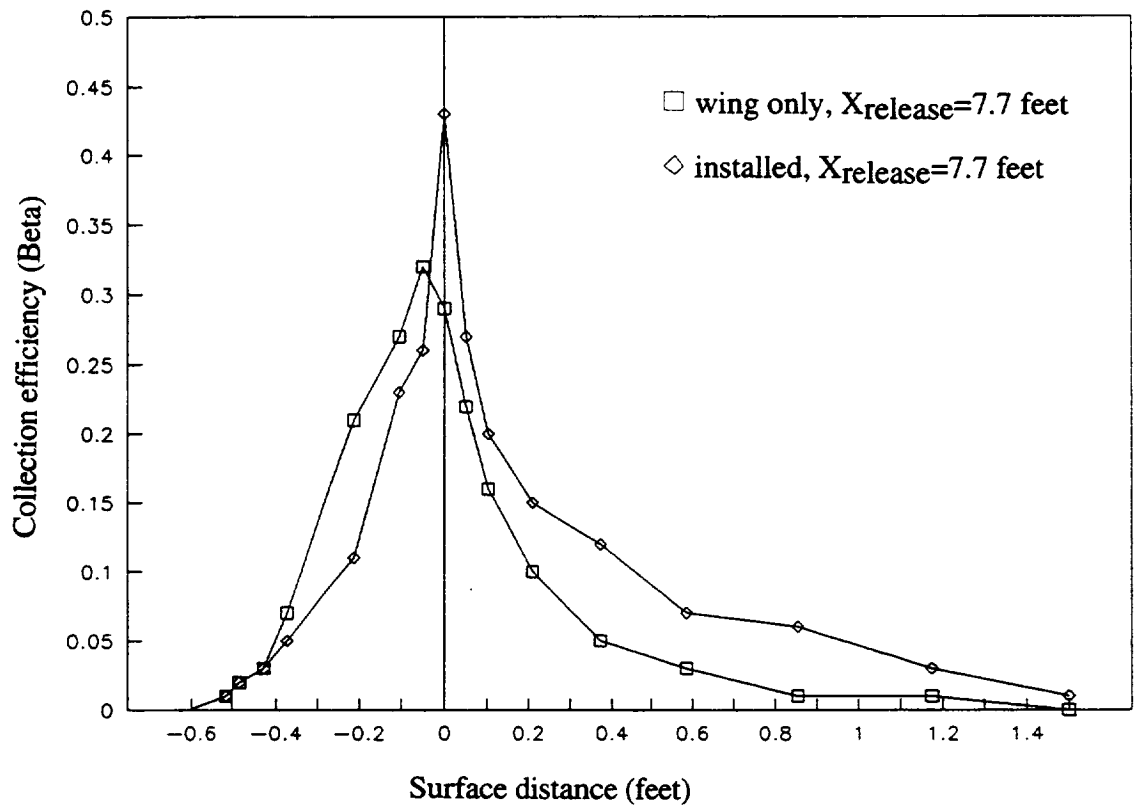
Figure 4.40 Water droplet collection efficiency on the Twin Otter wing both installed in the

IRT and isolated at 0 degrees angle of attack for 20 micron MVD droplet distribution
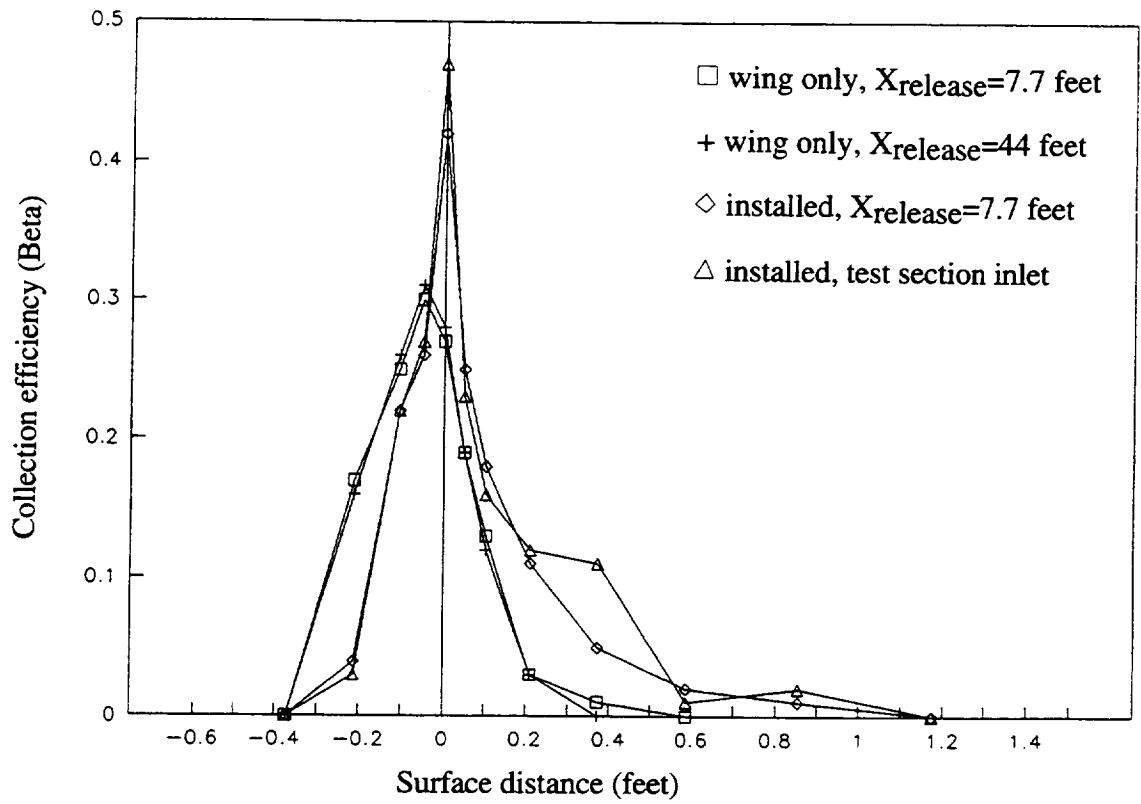
Figure 4.41 Water droplet collection efficiency on the Twin Otter wing both installed in the IRT and isolated with release points at 7.7 and 44.0 feet at 0 degrees angle of attack for 20 micron droplets
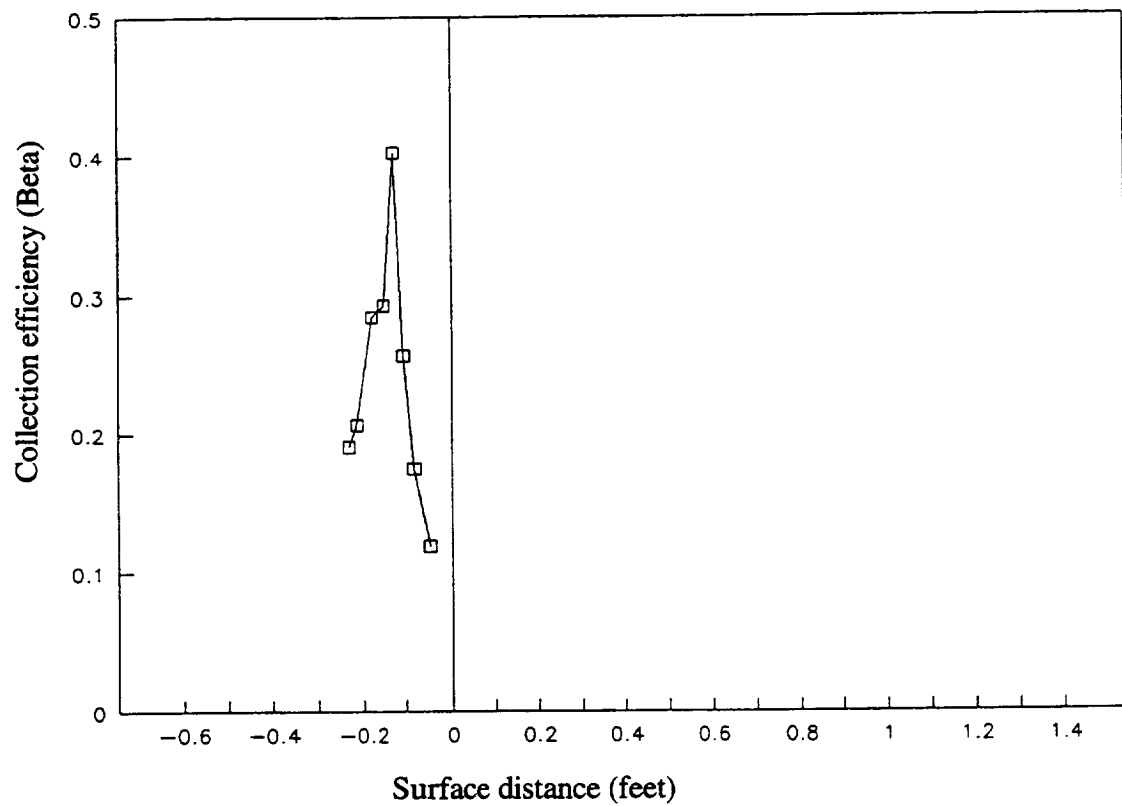
Figure 4.42 Water droplet collection efficiency on the Twin Otter wing installed in the IRT

at 0 degrees angle of attack for 20 micron droplets, based upon LEWICE calculation

technique
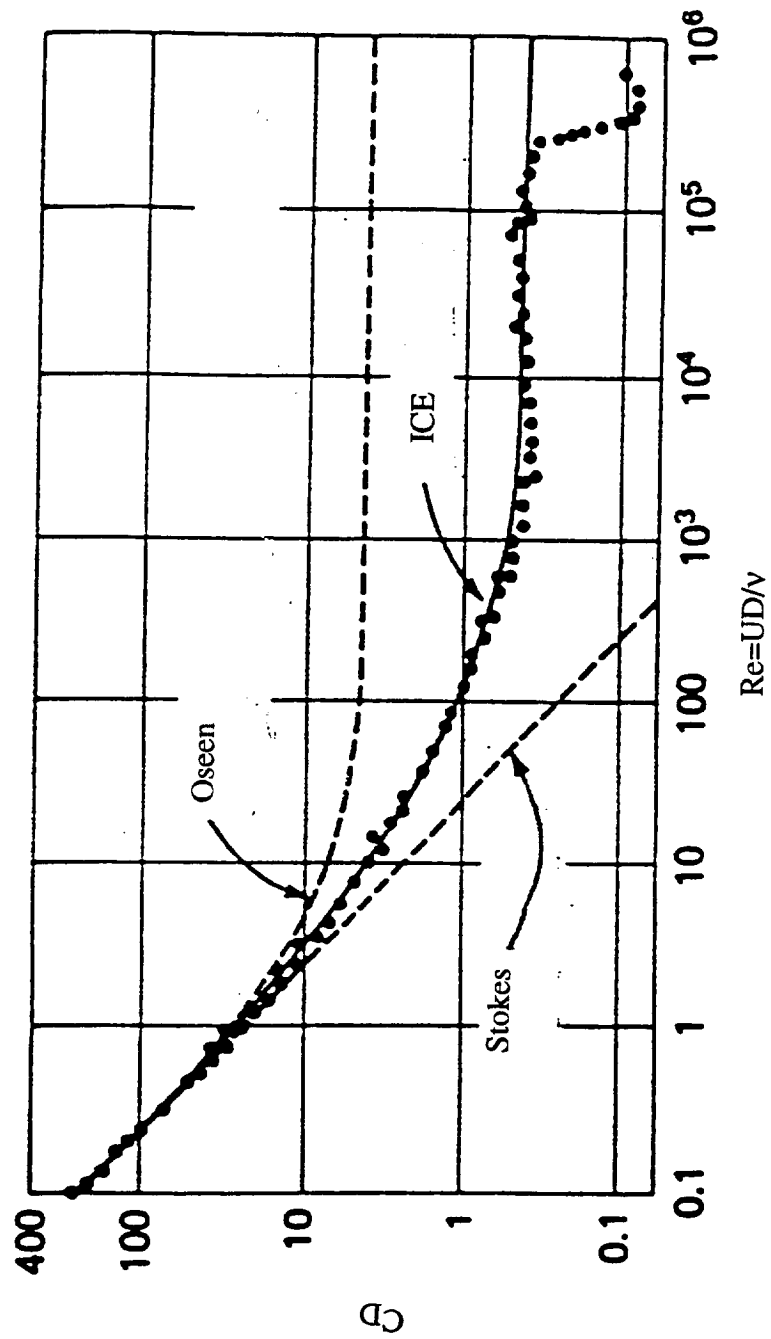
Figure A.1   The drag coefficient of spheres

Figure B.1 Trajectories about a NACA 0012 airfoil
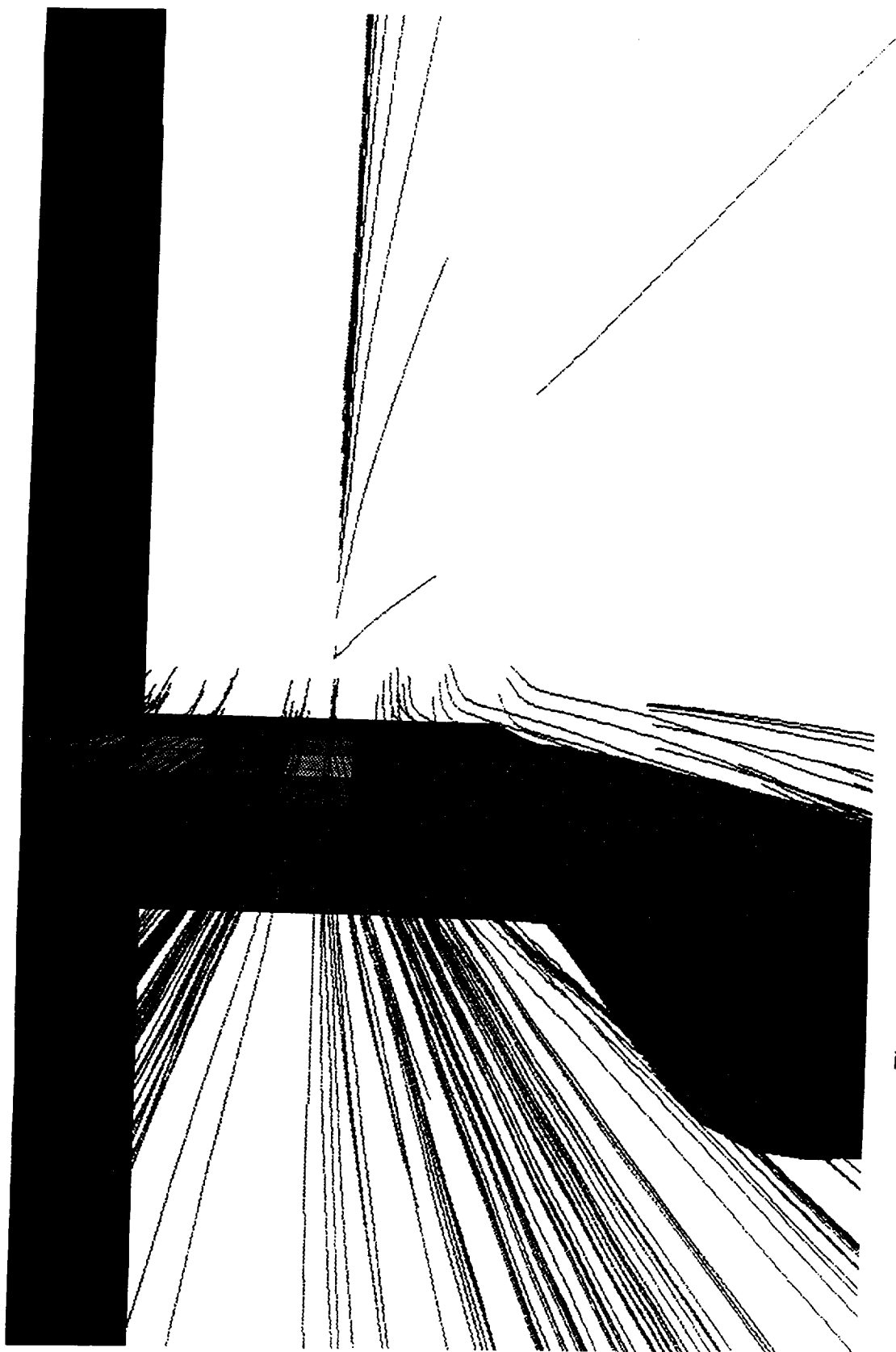
Figure B.2 Trajectories calculated with the Newton-Raphson UPDATE routine

159
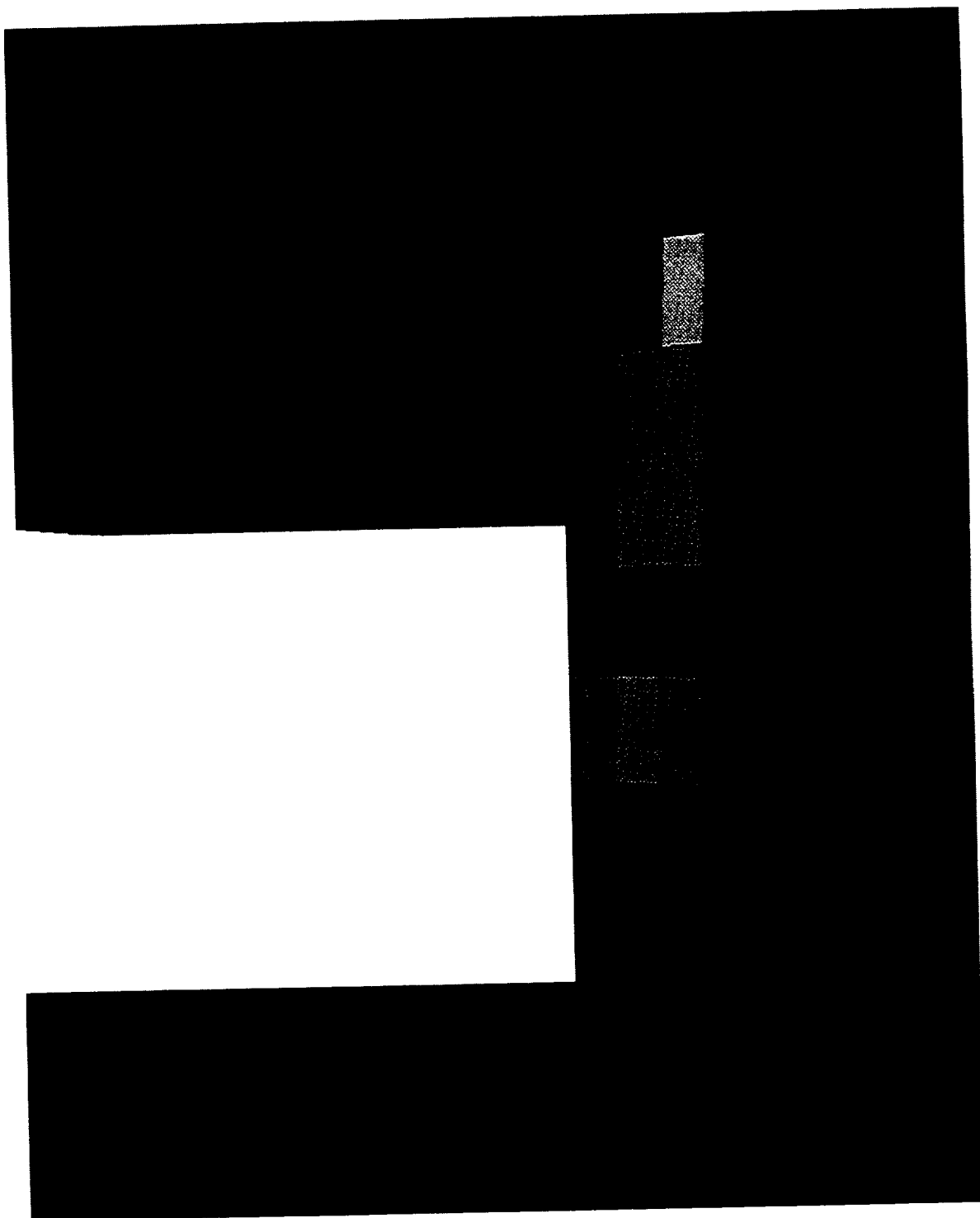
Figure B.3   Betas calculated with the Newton-Raphson UPDATE routine
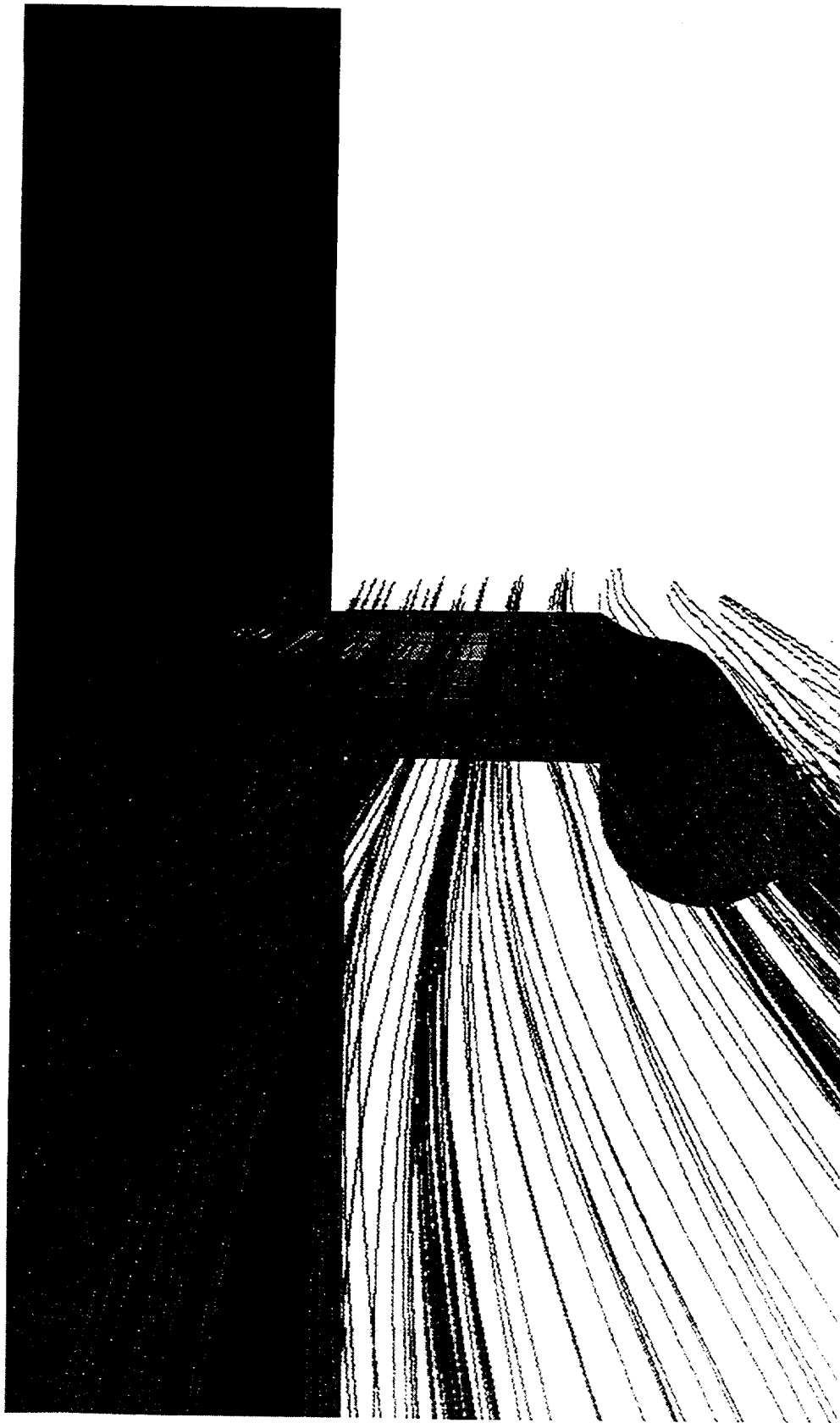
Figure B.4 Trajectories calculated with the bisection UPDATE routine
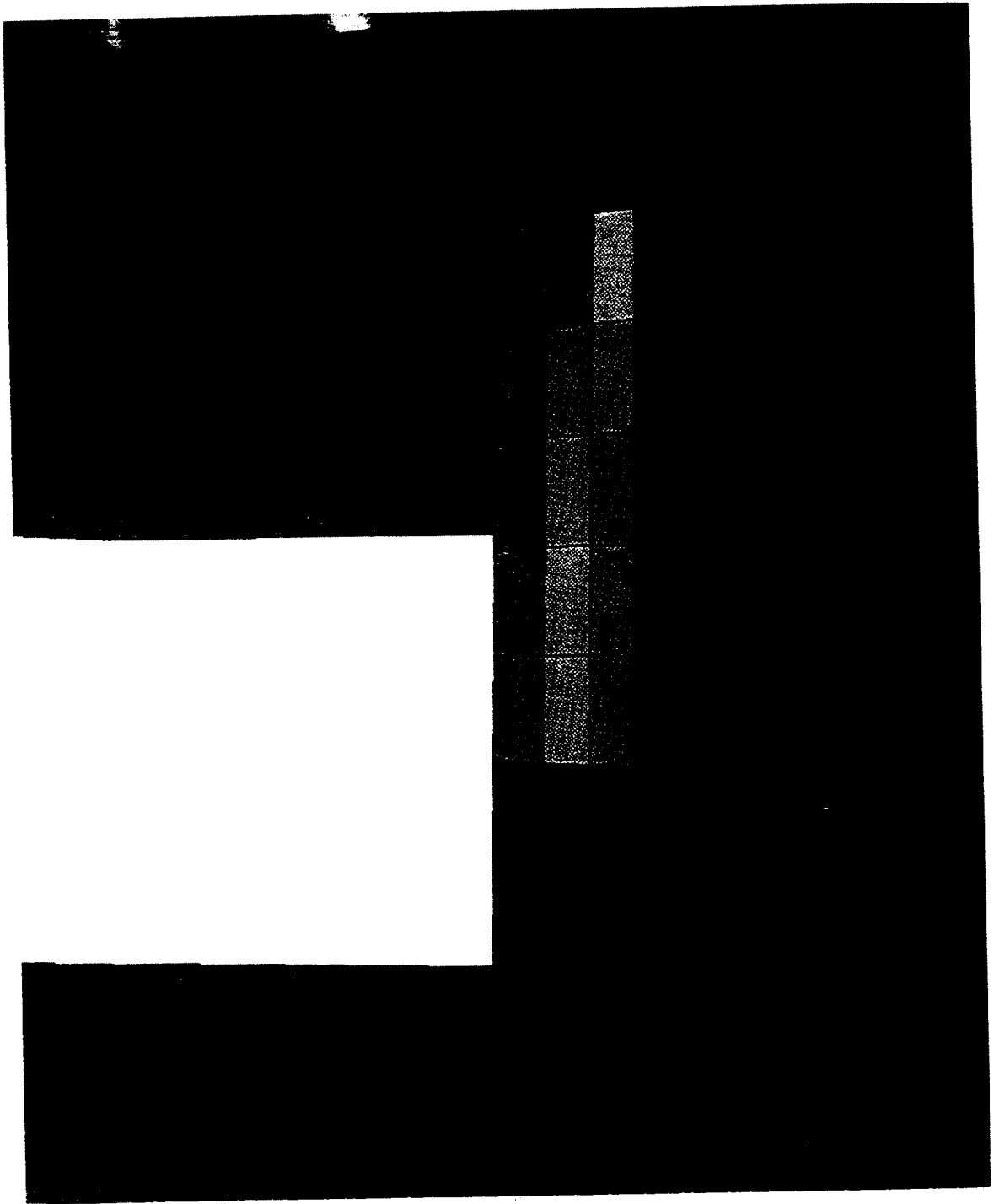
Figure B.5   Betas calculated with the bisection UPDATE routine
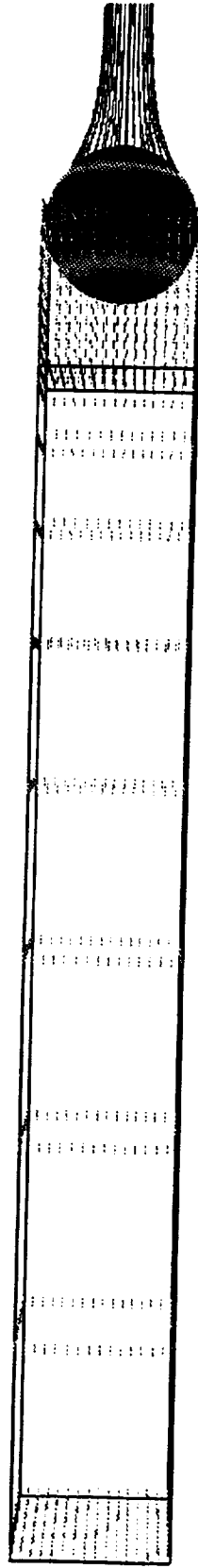
Figure C.1 VSAERO model of sphere showing on-body pressure distribution, off-body grid and wakes
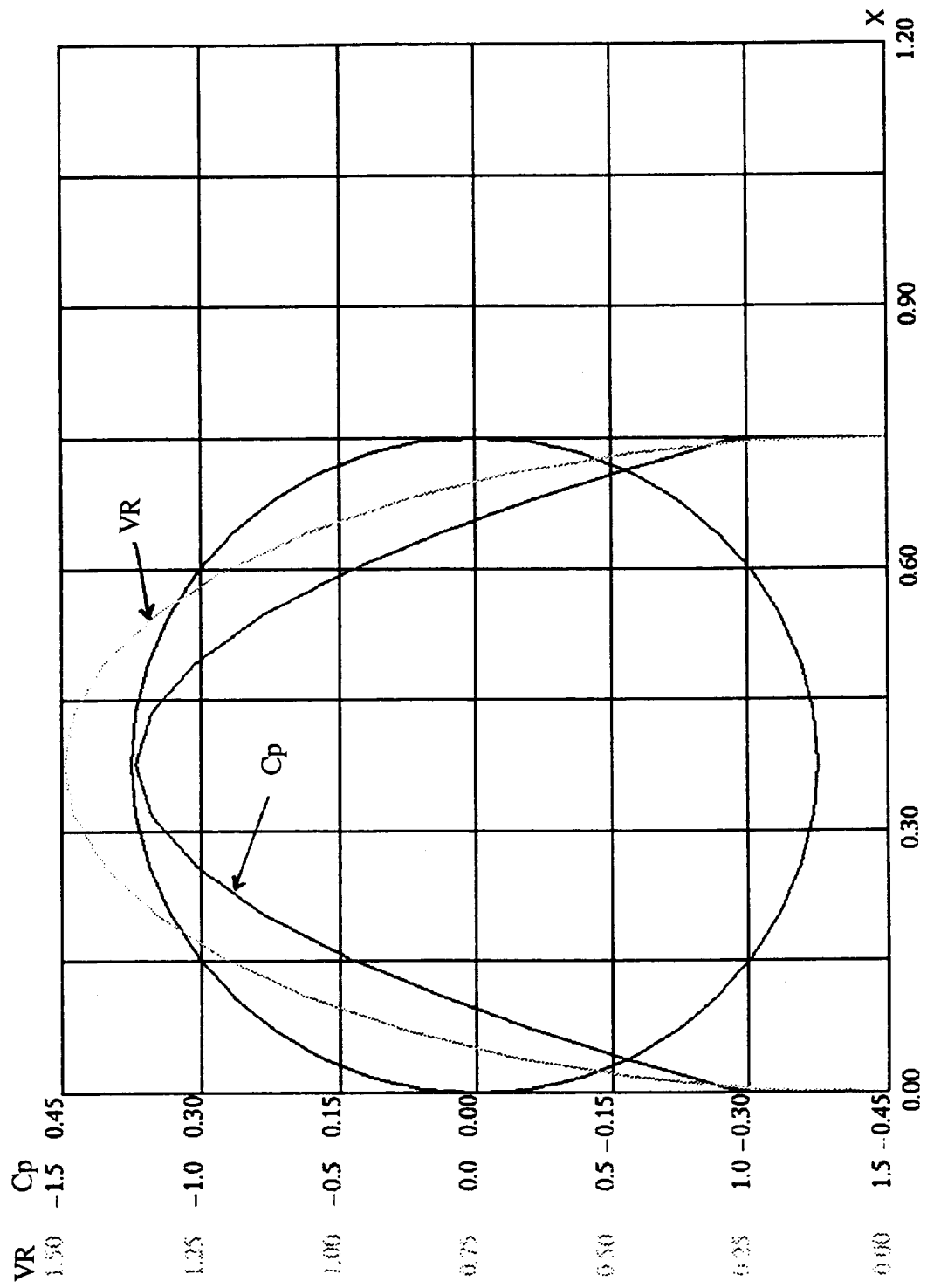
Figure C.2 Pressure and velocity distribution on sphere in pure potential flow
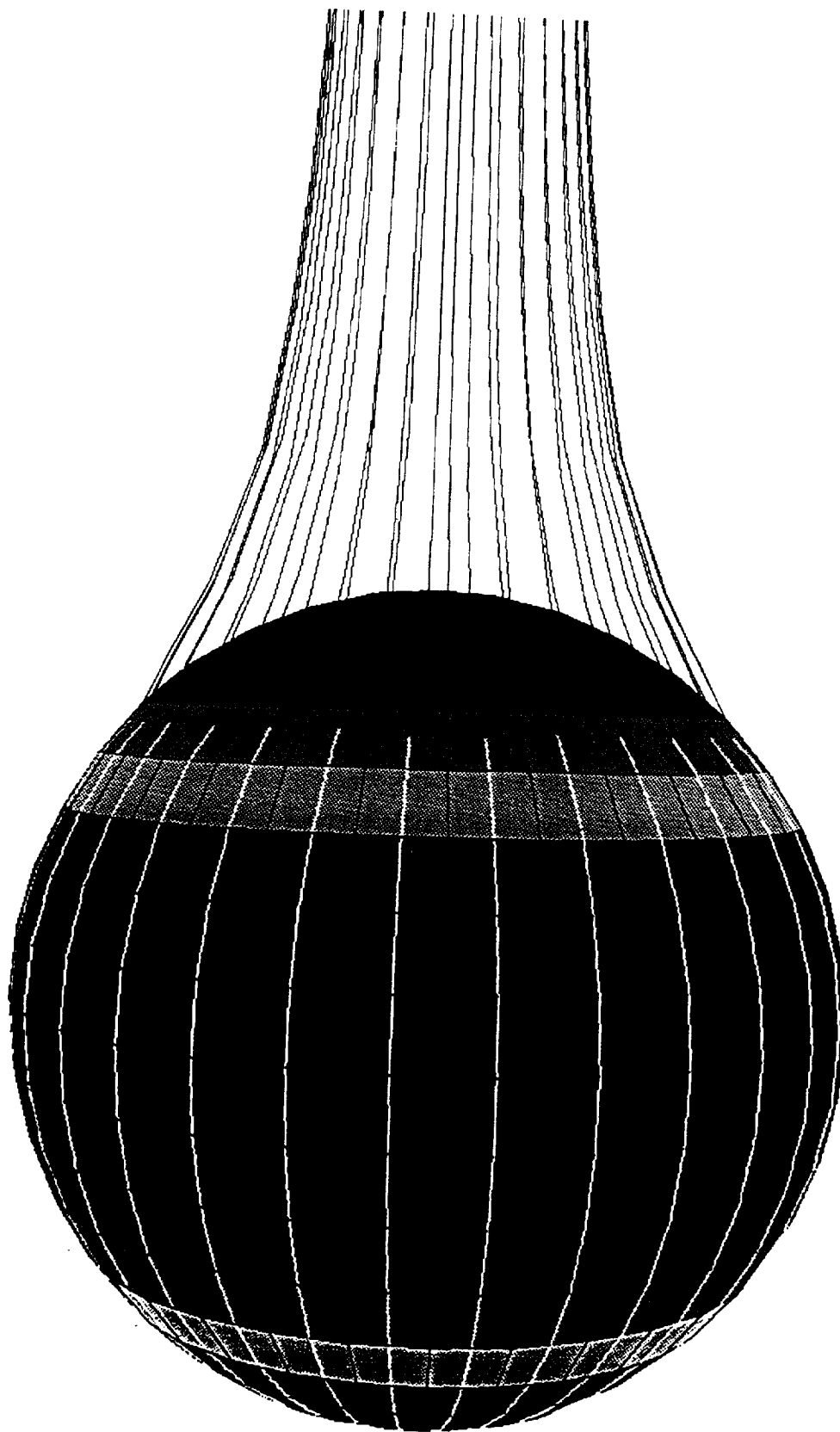
Figure C.3 Close-up of sphere showing pressure distribution and wakes after 3 wake iterations and 3 boundary layer iterations
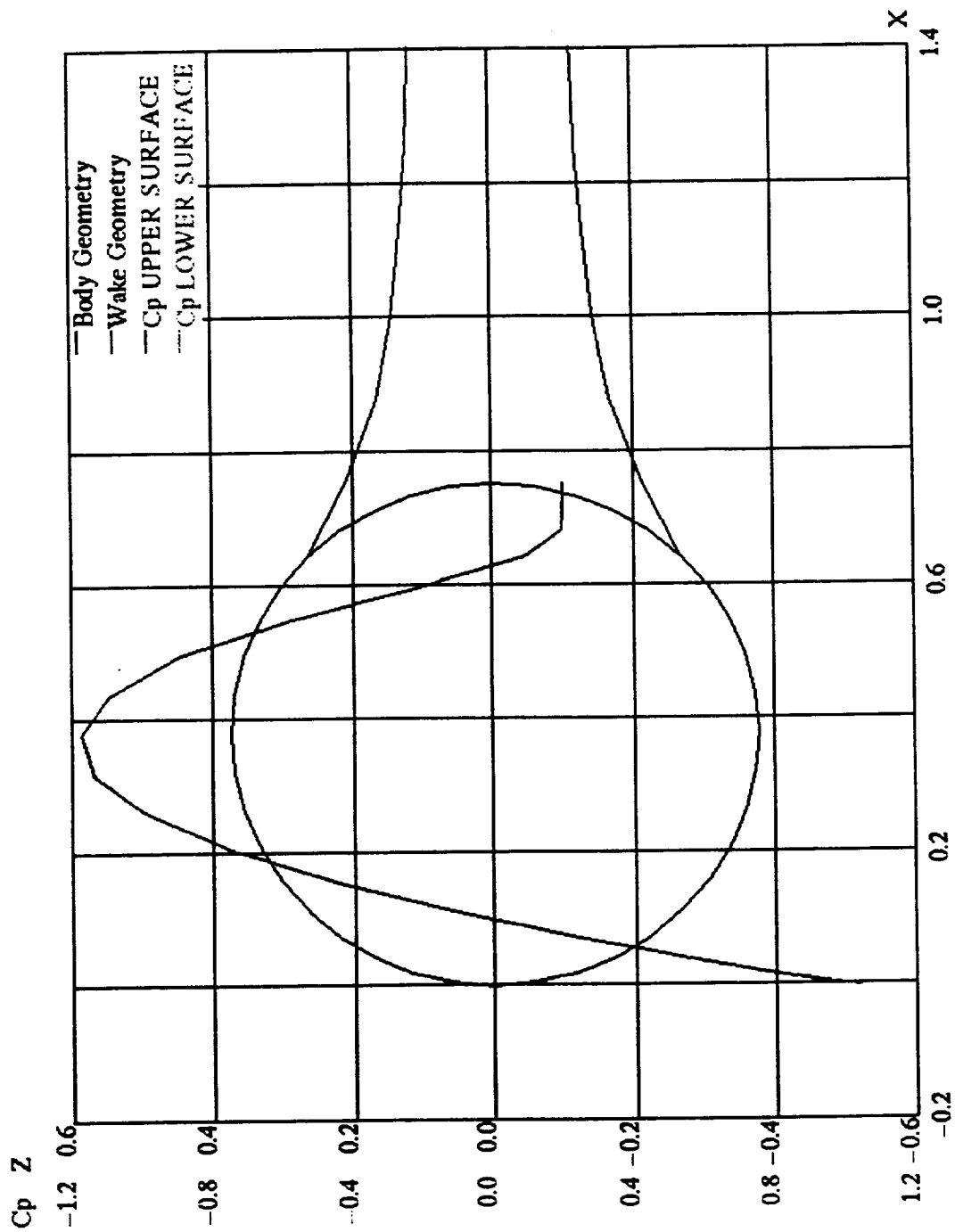
Figure C.4   Pressure distribution on sphere after 3 wake iterations and 3 boundary layer
iterations
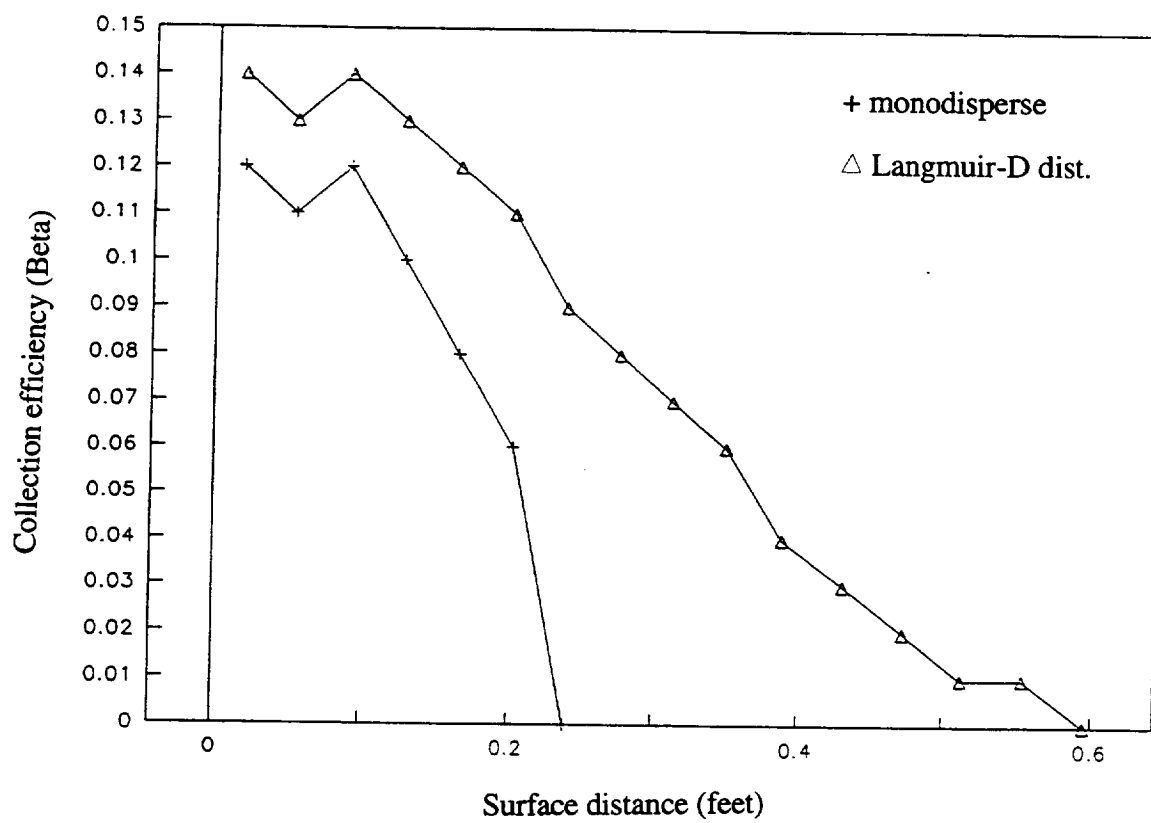
Figure C.5 Collection efficiency curves for monodispersion and Langmuir-D droplet size distributions
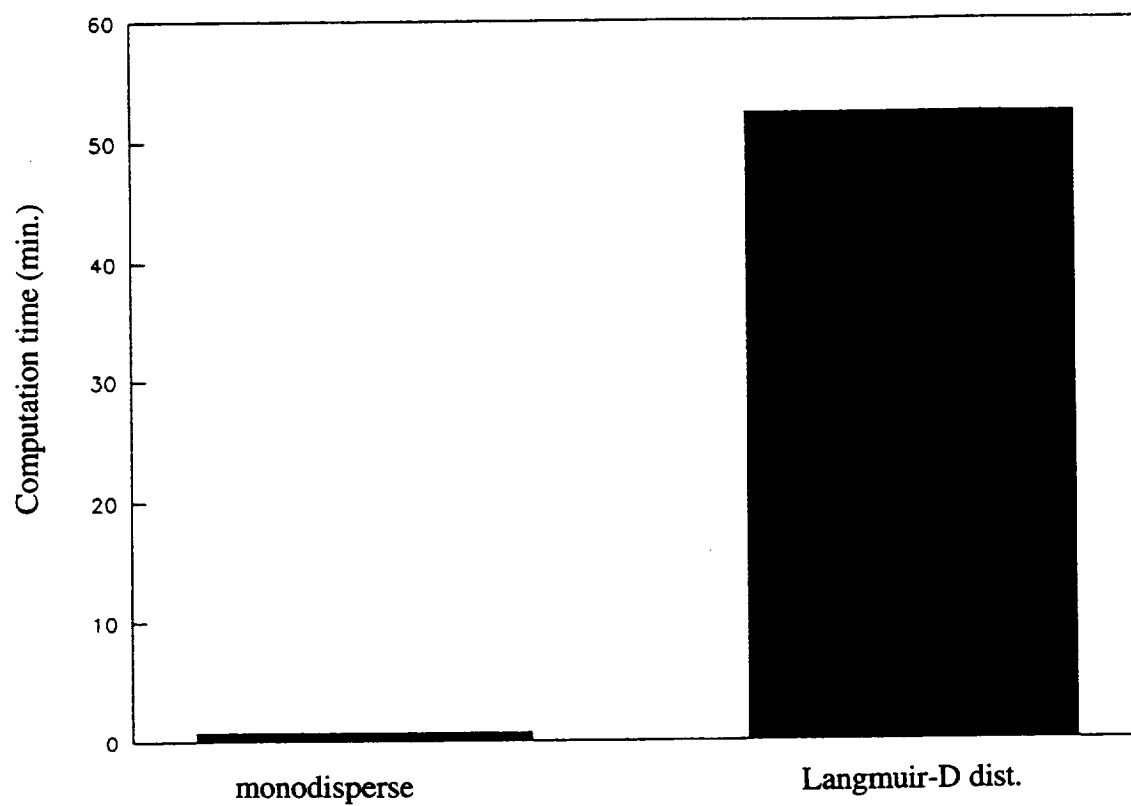
Figure C.6 Computation times of collection efficiency calculations for monodispersion and Langmuir-D droplet size distributions
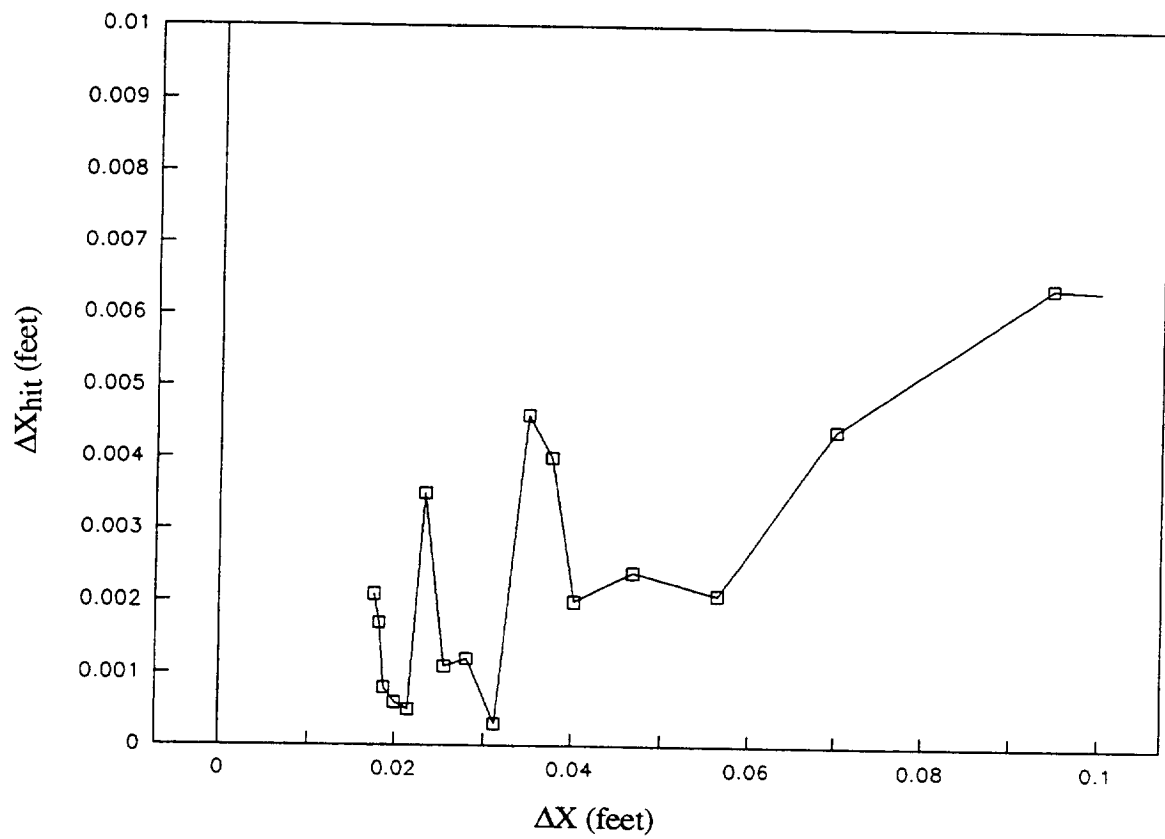
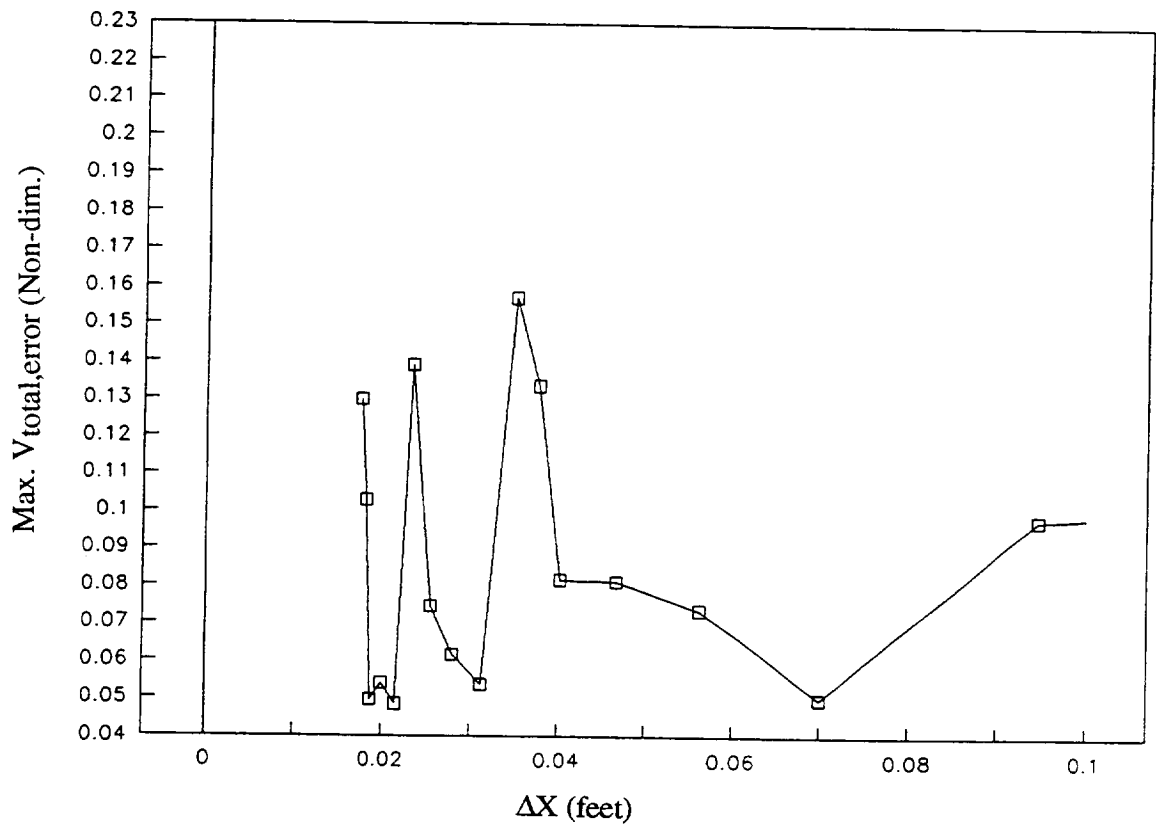Figure C.7   Grid resolution study, ?x25x25 grid, D=14.7 microns, x-direction accuracy vs. x-grid spacing
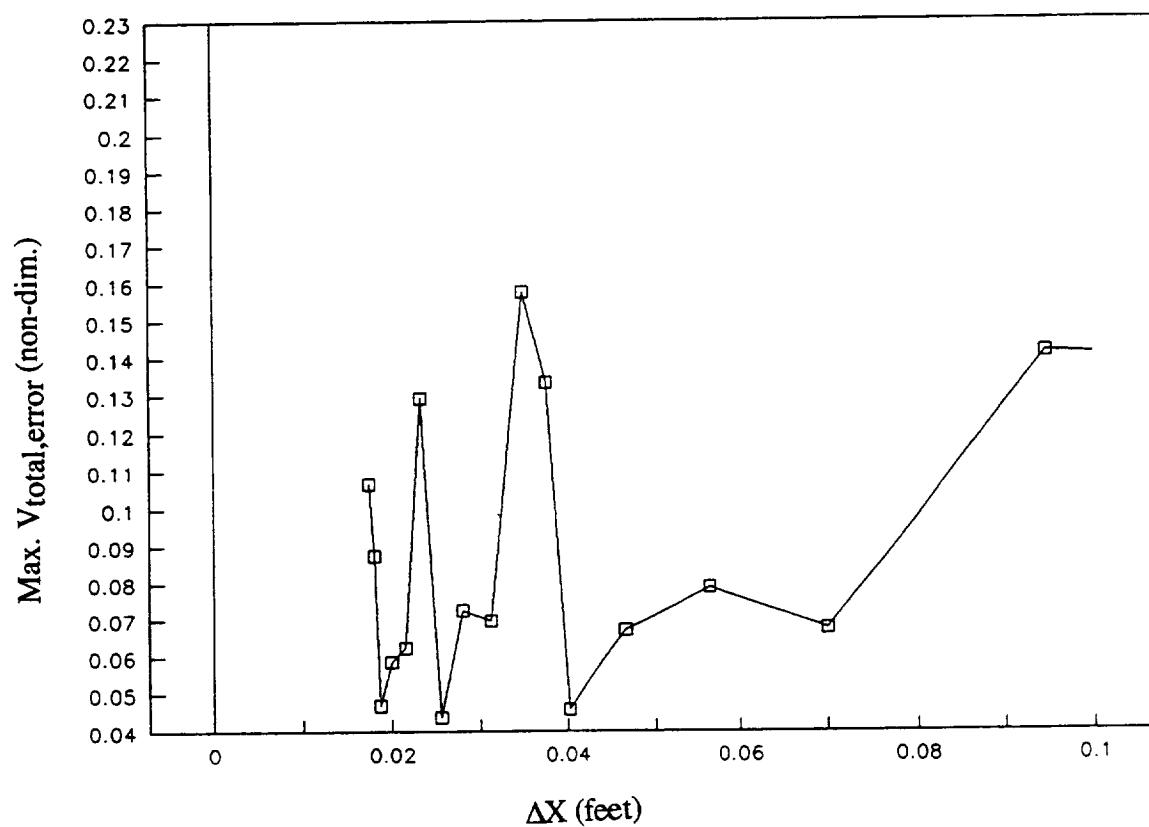
Figure C.8   Grid resolution study, ?x25x25 grid, D=14.7 microns, maximum $V_{total,error}$
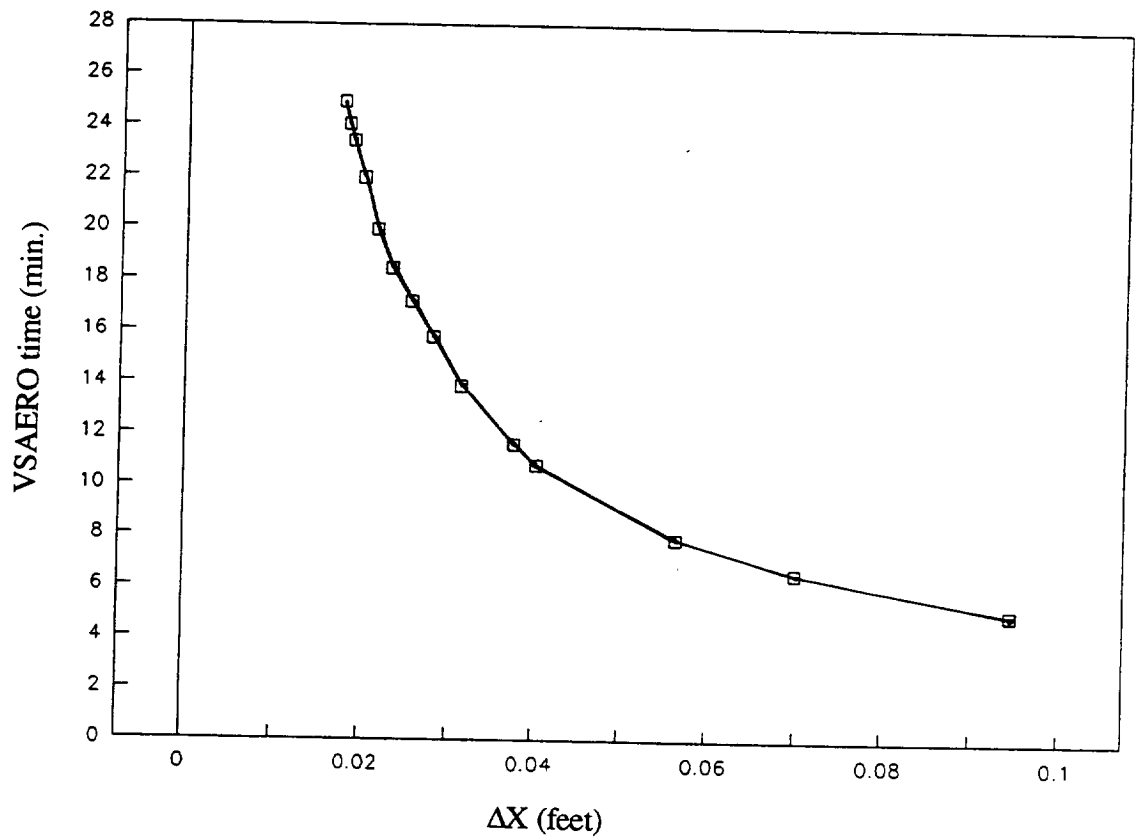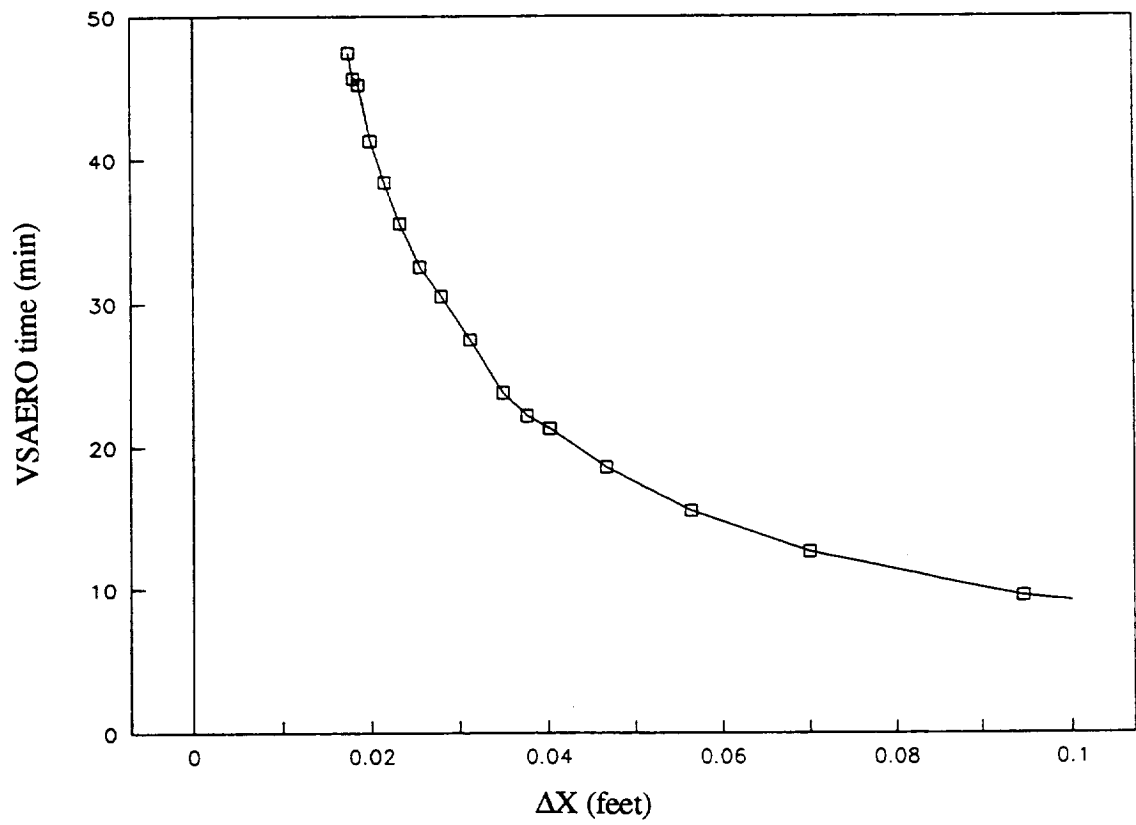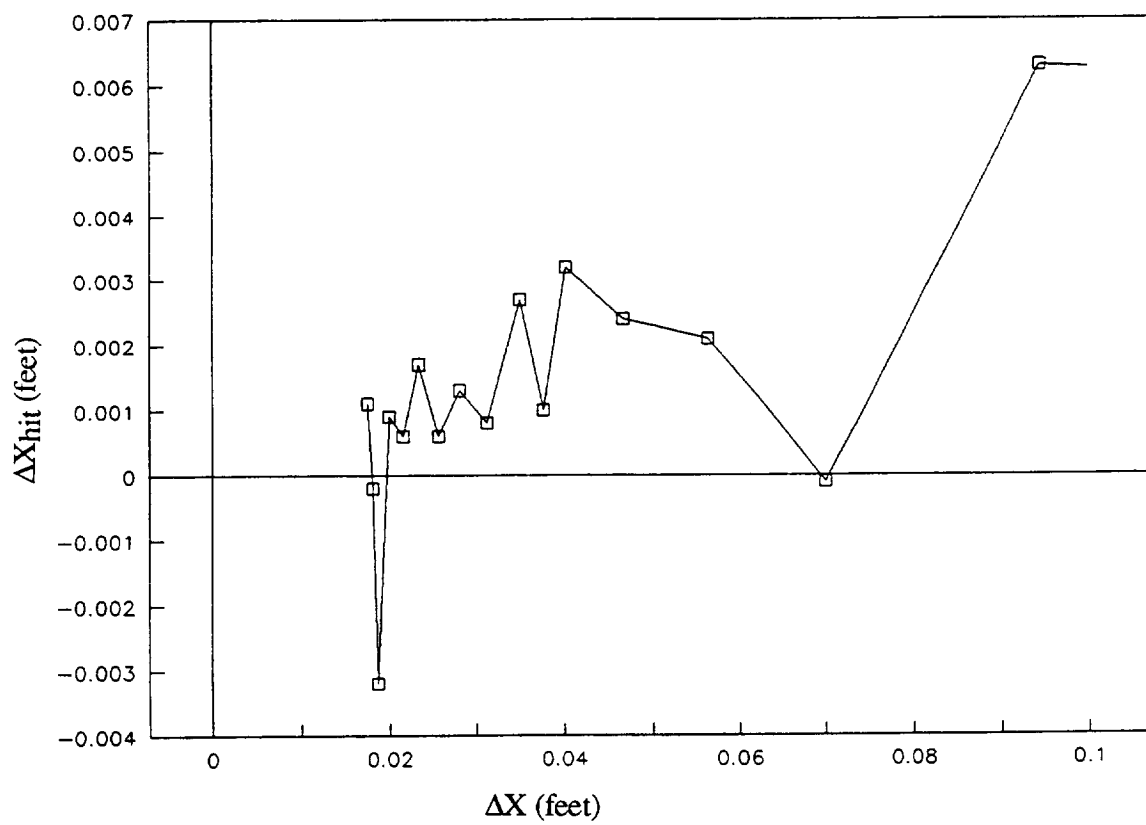
vs. x-grid spacing

Figure C.9 Grid resolution study, ?x25x25 grid, D=14.7 microns, VSAERO time vs. x-grid spacing
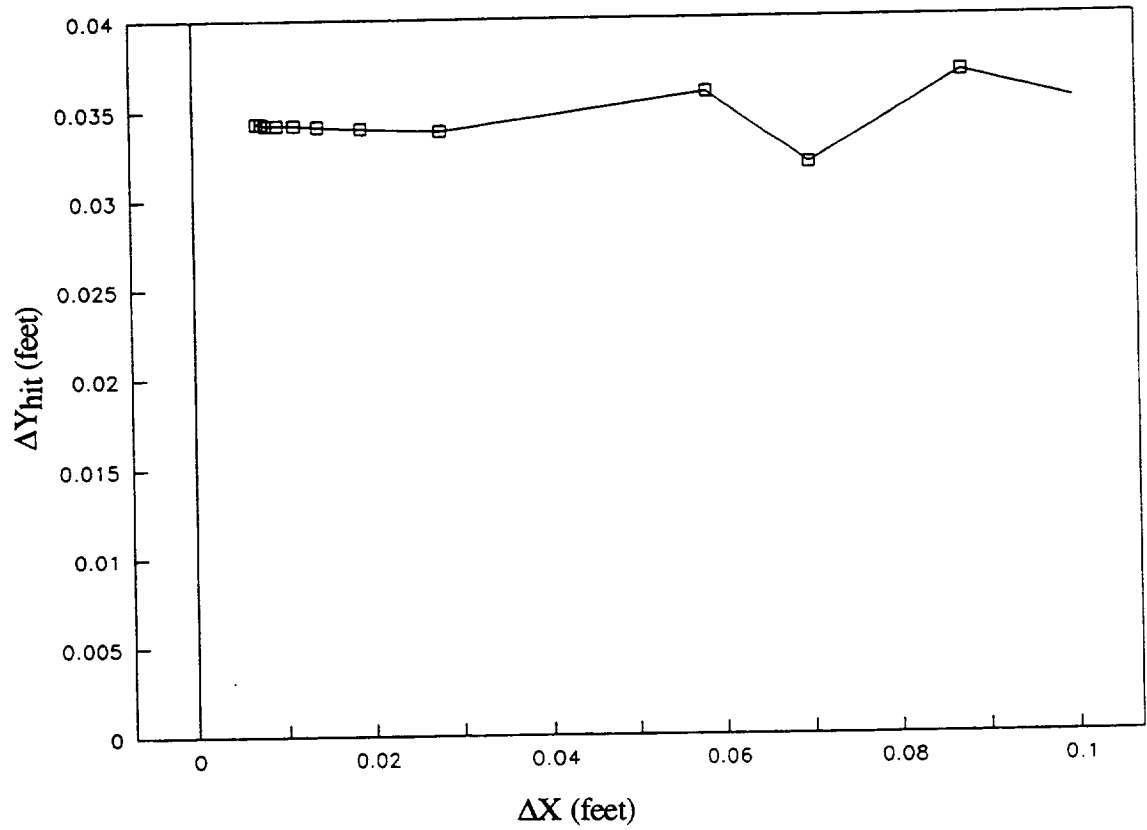
Figure C.10 Grid resolution study, 25x?x25 grid, D=14.7 microns, y-direction accuracy vs. y-grid spacing
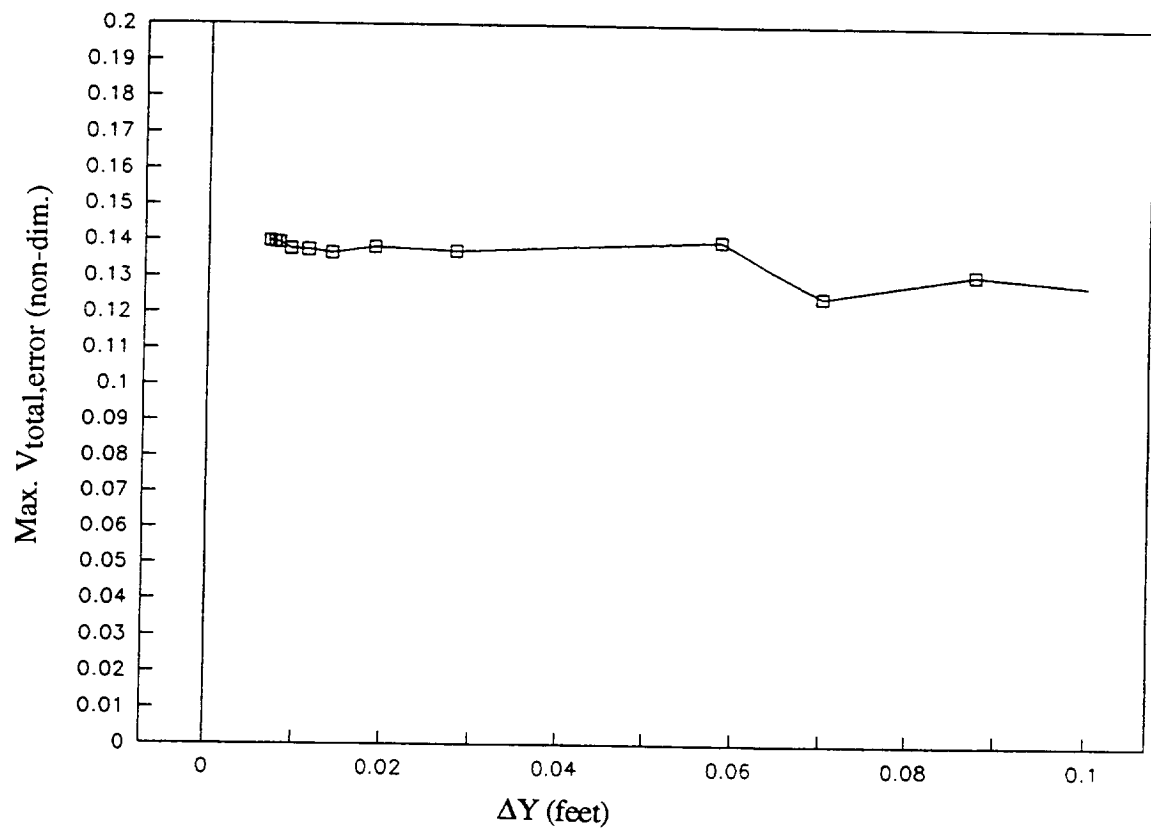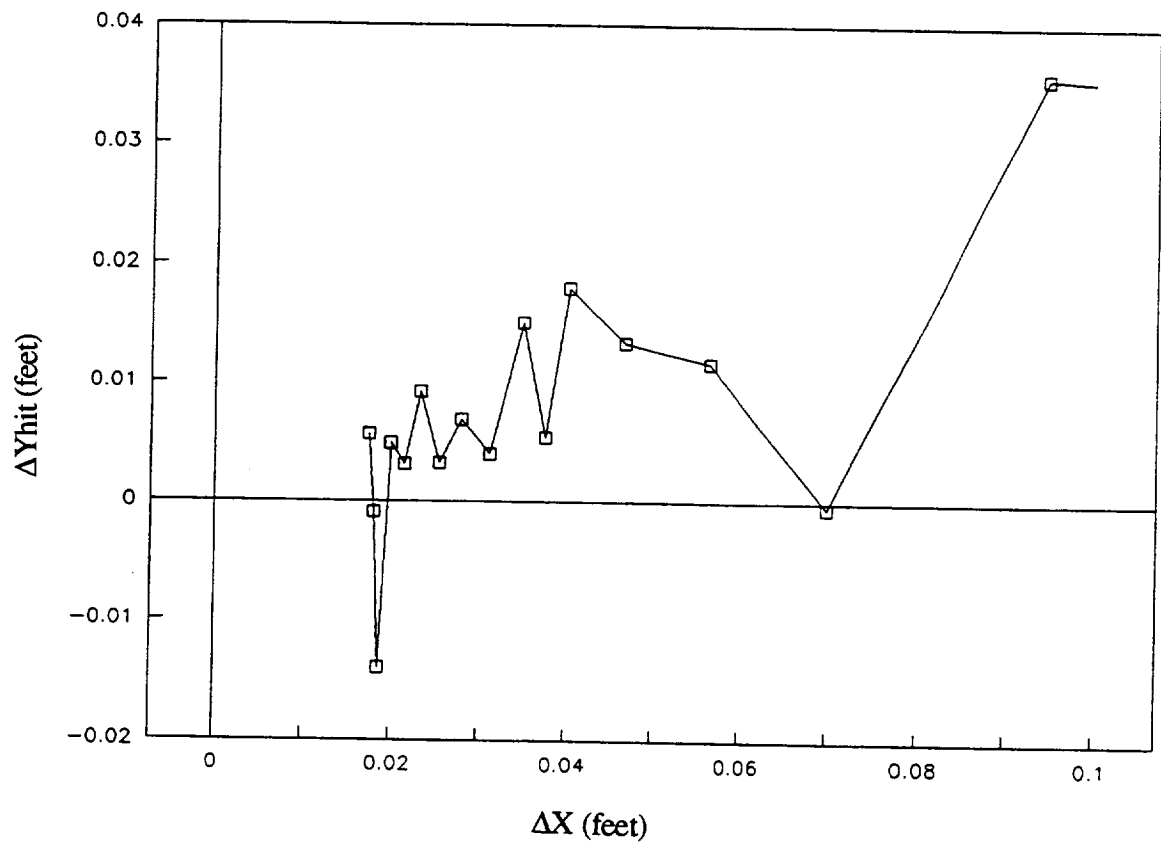
Figure C.11 Grid resolution study, 25x?x25 grid, D=14.7 microns, maximum $V_{total,error}$ vs. y-grid spacing
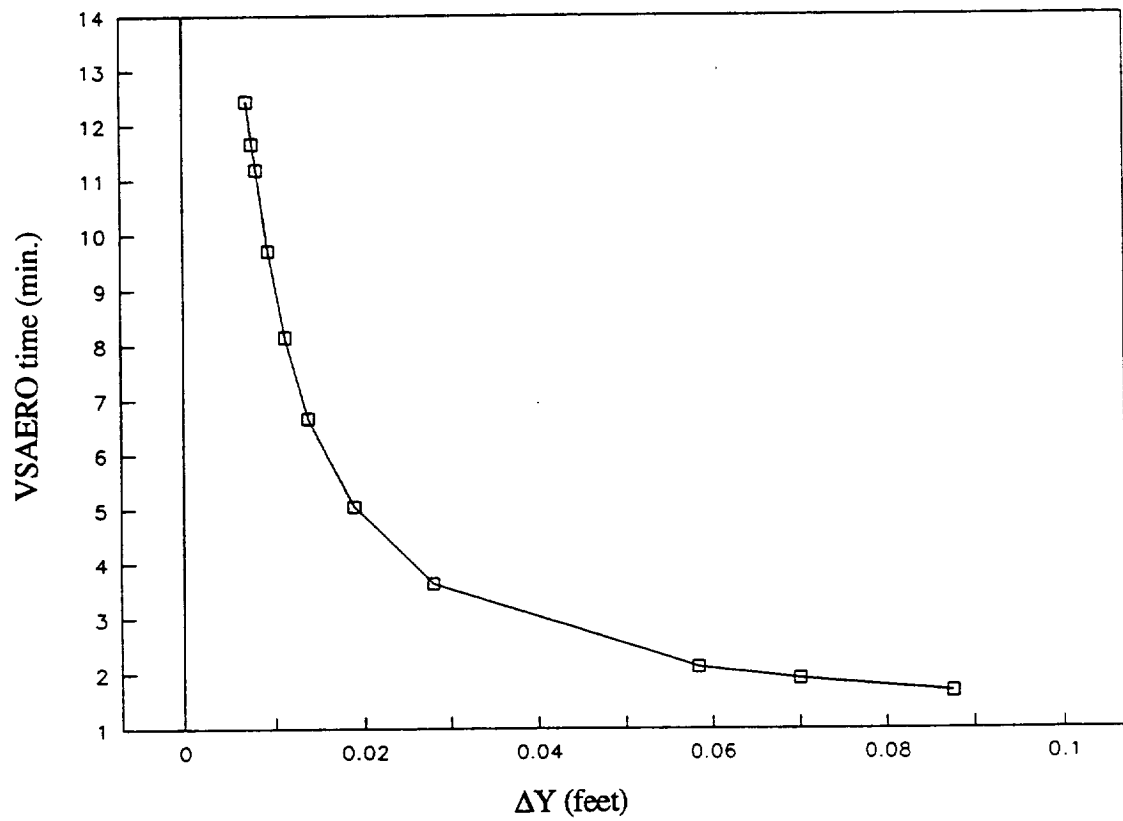
Figure C.12 Grid resolution study, 25x?x25 grid, D=14.7 microns, VSAERO time vs. y-grid spacing
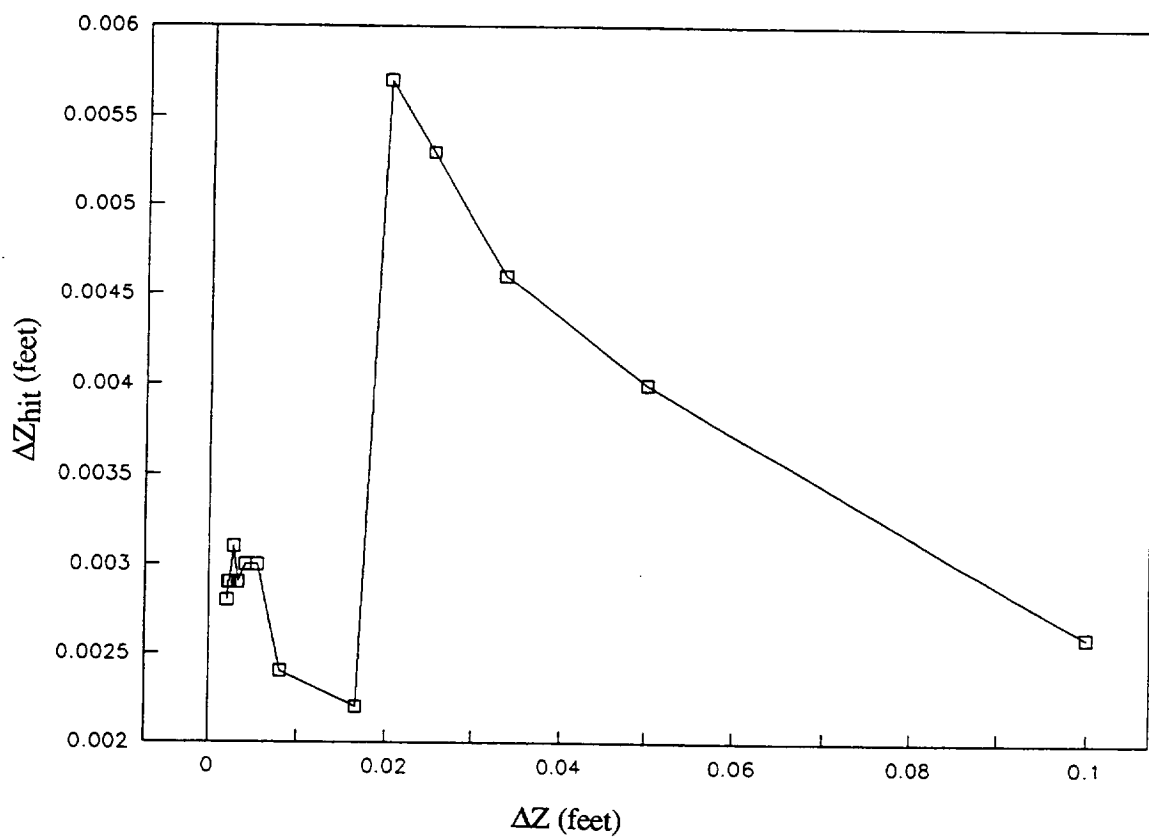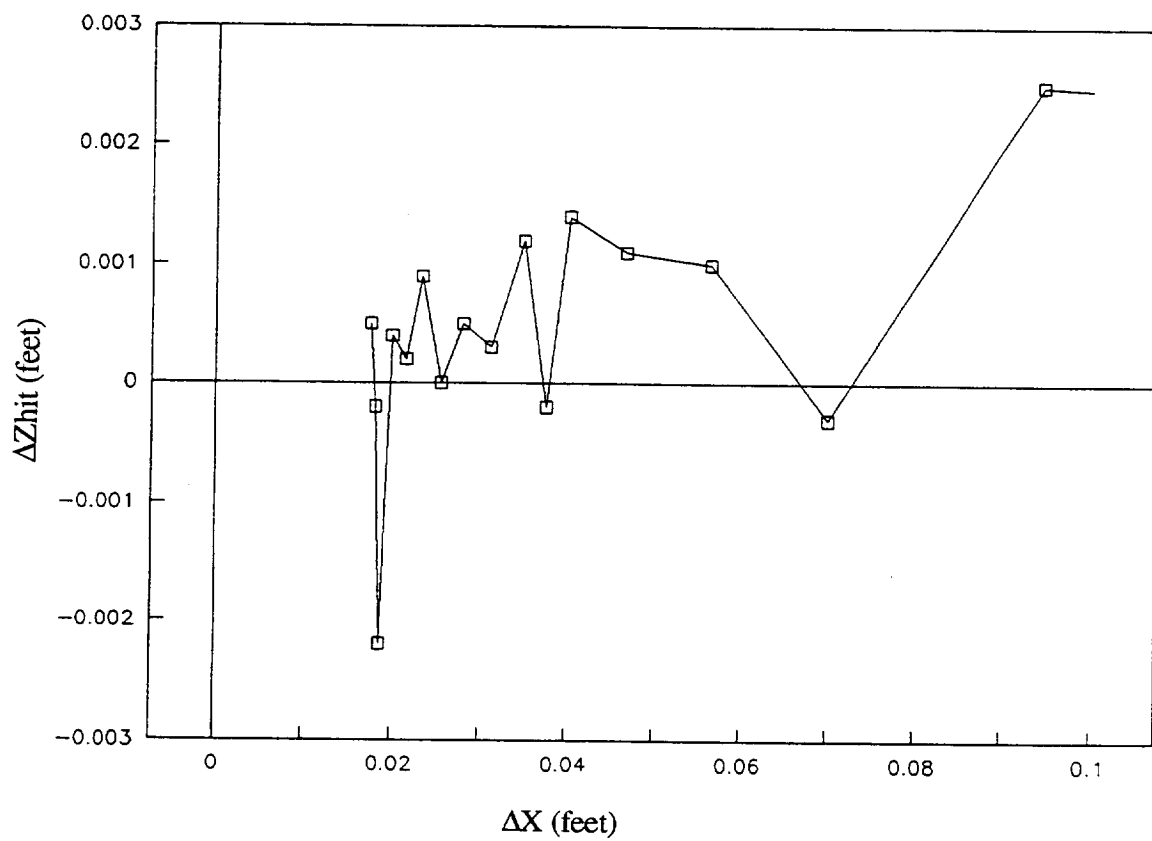
Figure C.13 Grid resolution study, 25x25x? grid, D=14.7 microns, z-direction accuracy vs. z-grid spacing
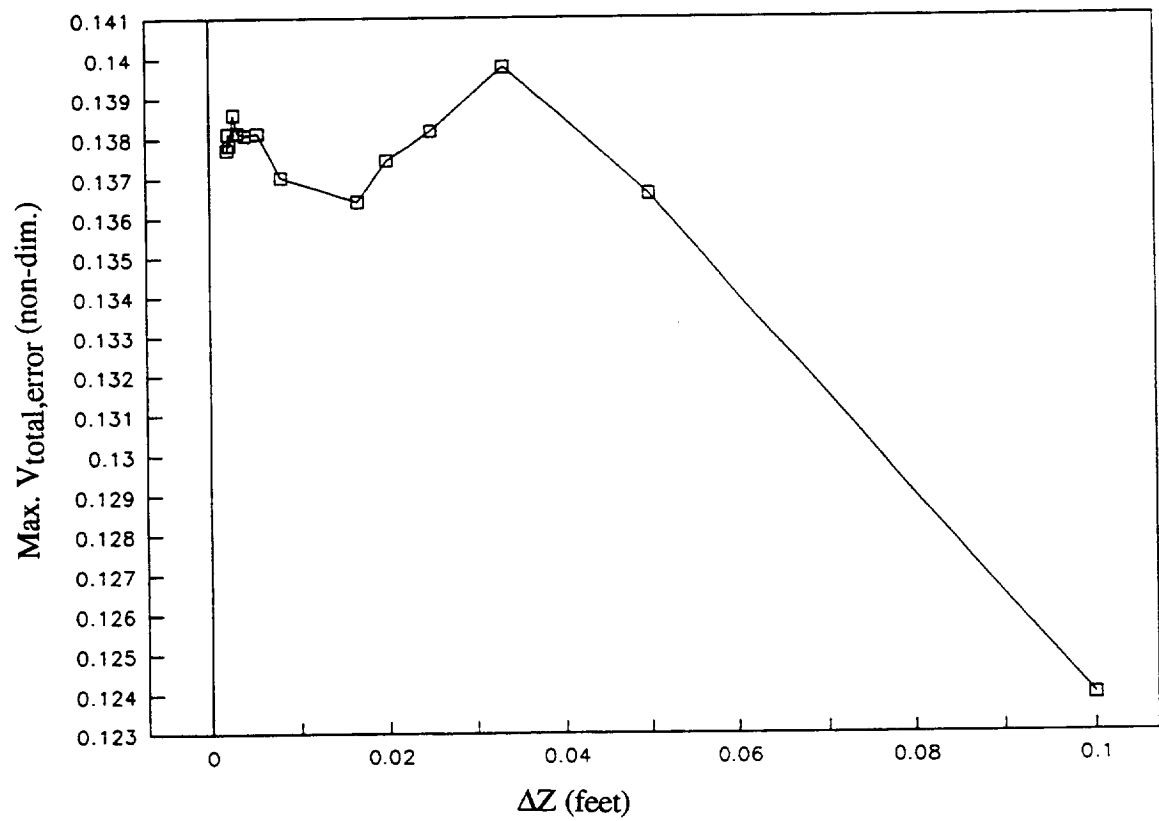
Figure C.14 Grid resolution study, 25x25x? grid, D=14.7 microns, maximum $V_{total,error}$

vs. z-grid spacing
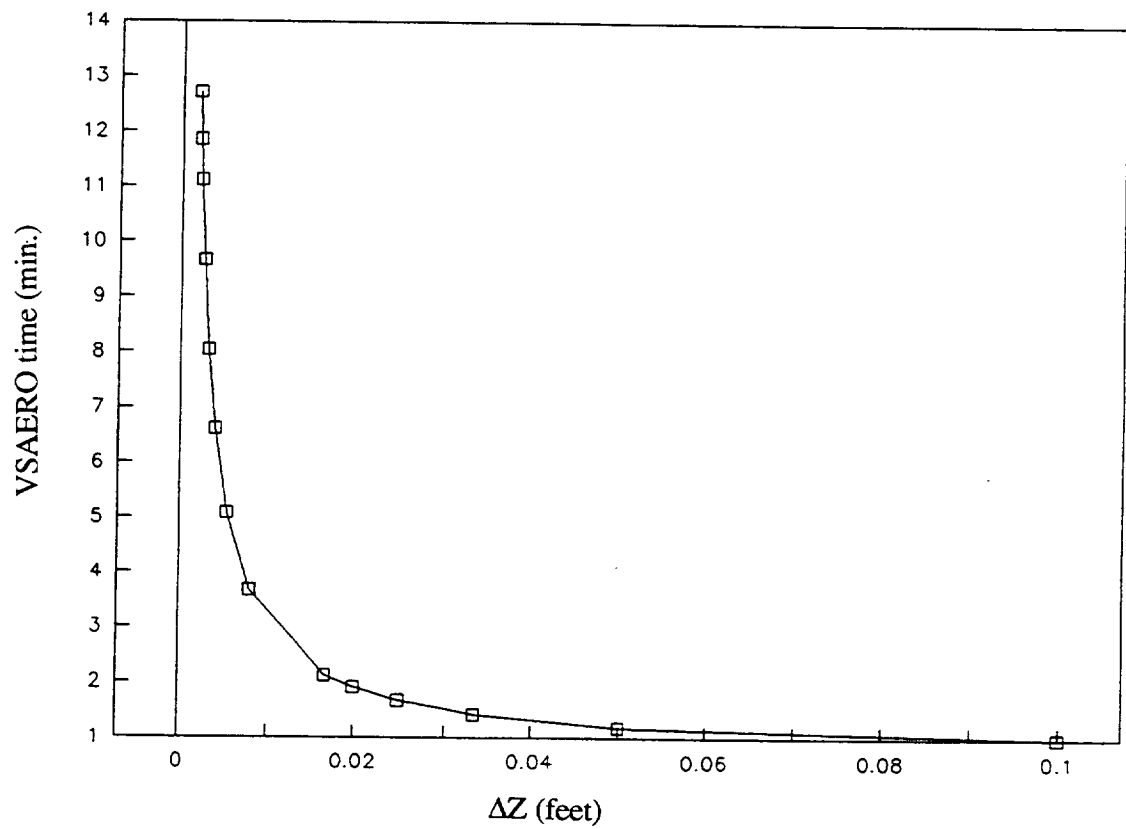
Figure C.15 Grid resolution study, 25x25x? grid, D=14.7 microns, VSAERO time vs. z-grid spacing
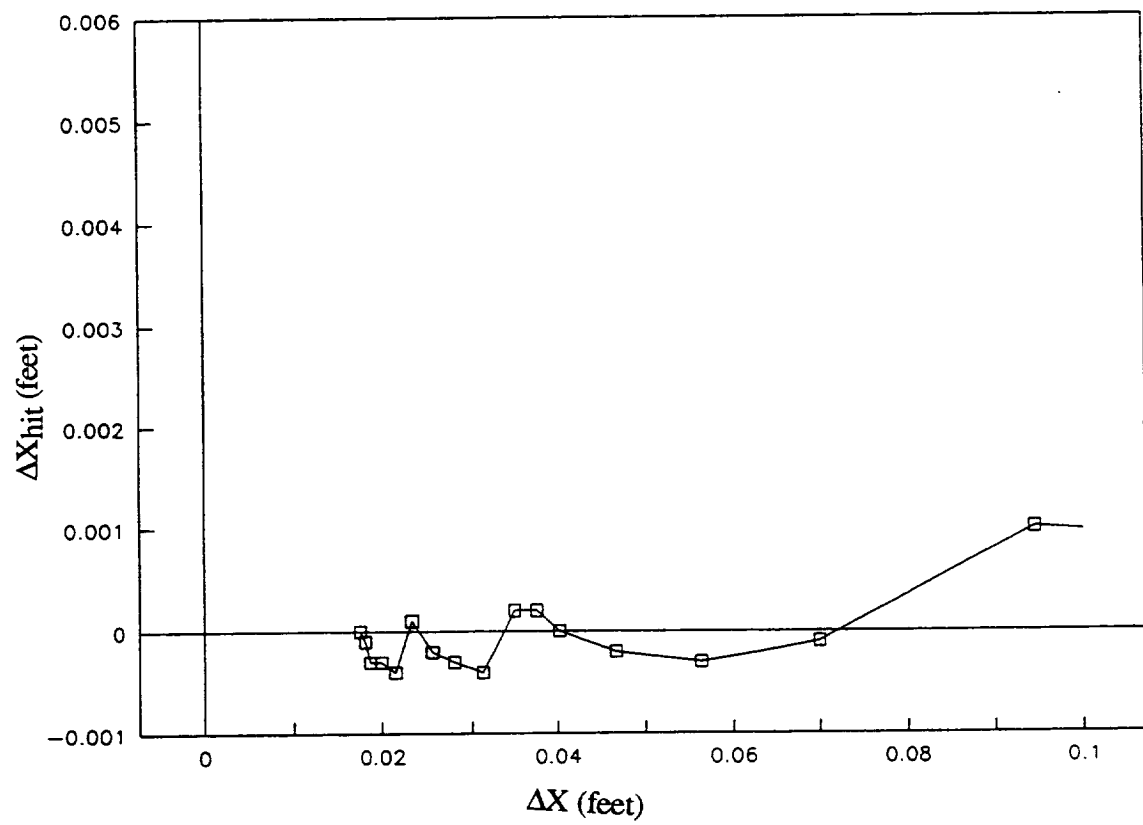
Figure C.16 Grid resolution study, ?x50x25 grid, D=18.6 microns, x-direction accuracy vs. x-grid spacing
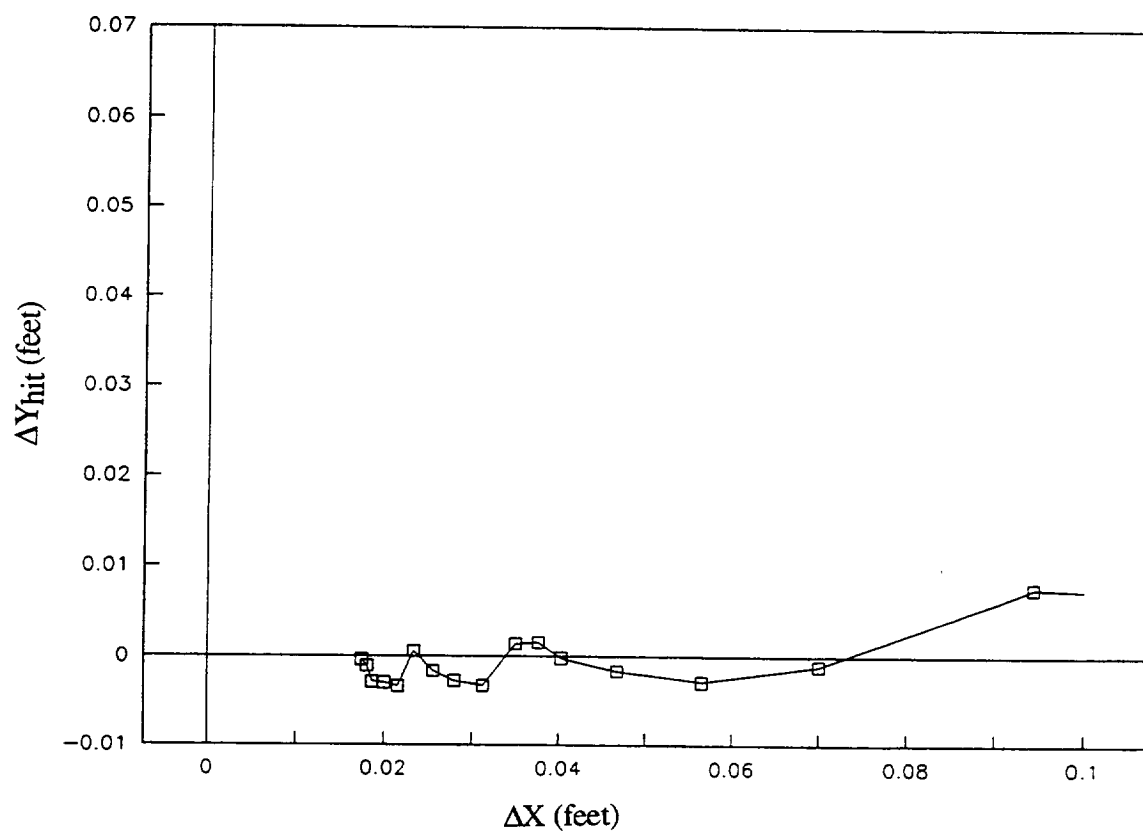
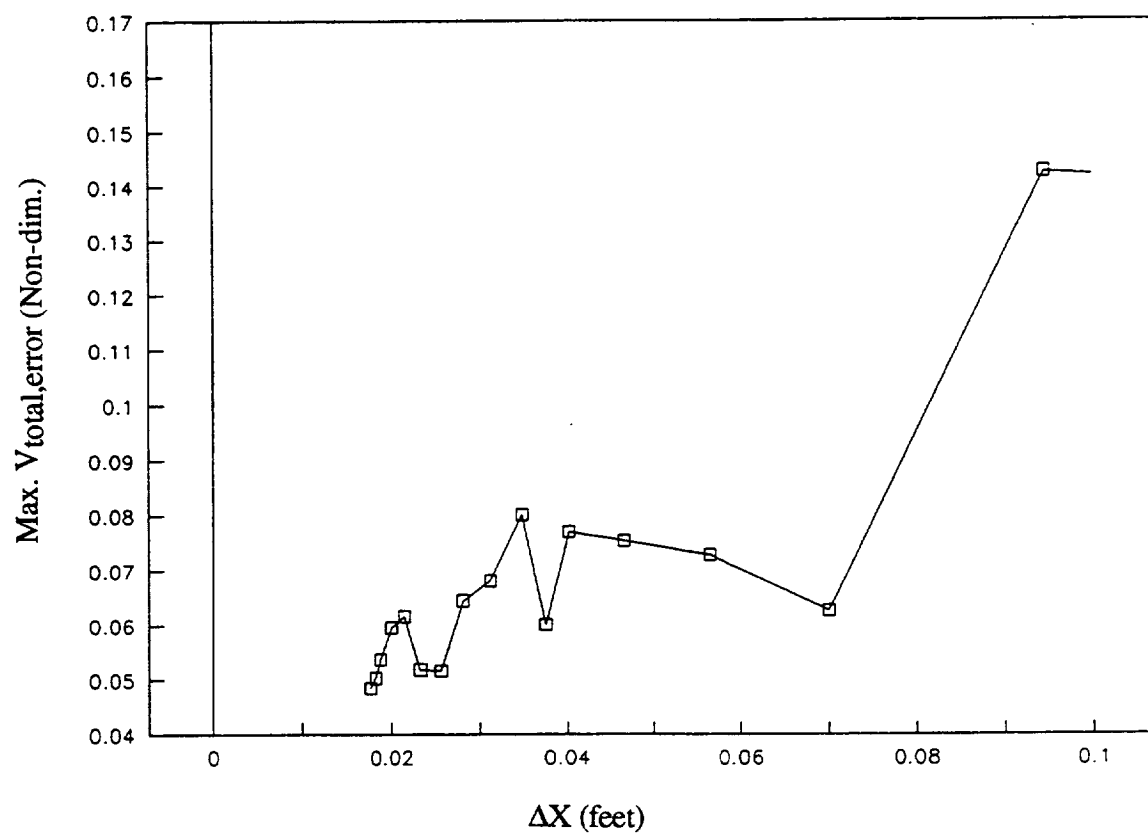Figure C.17 Grid resolution study, ?x50x25 grid, D=18.6 microns, y-direction accuracy vs. x-grid spacing
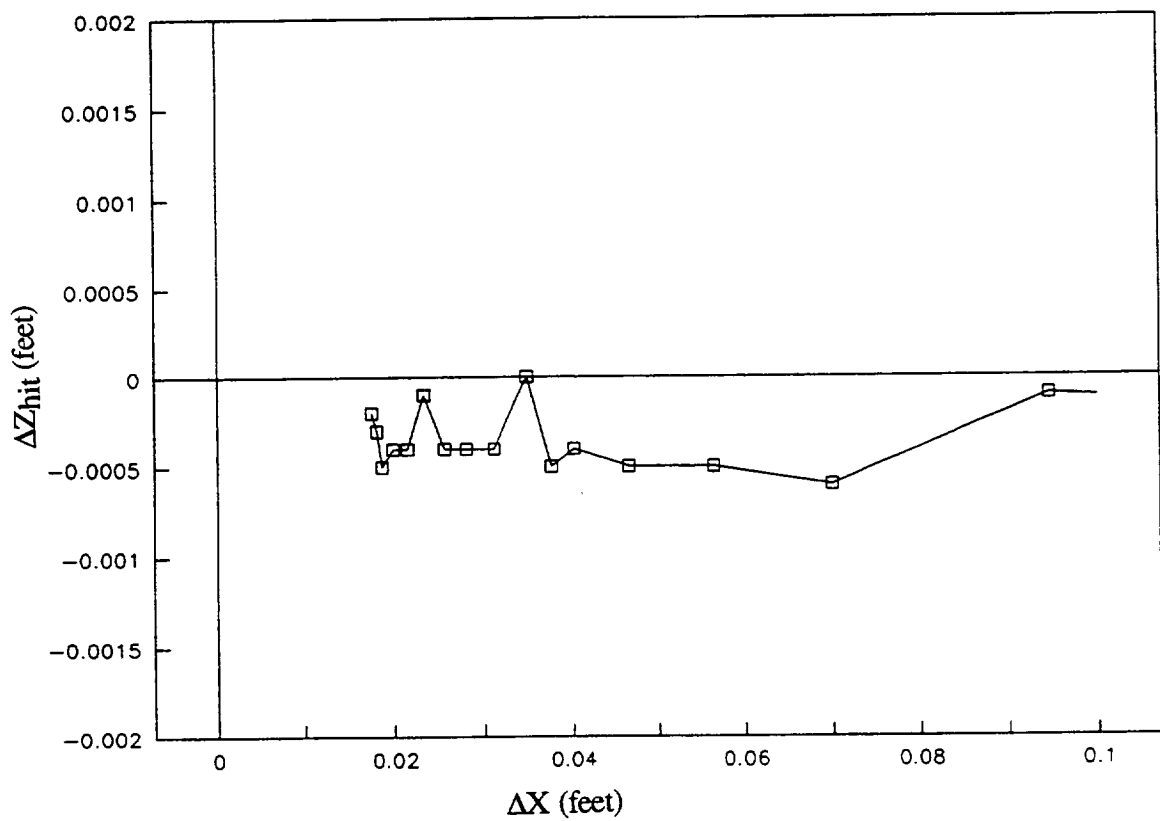
Figure C.18 Grid resolution study, ?x50x25 grid, D=18.6 microns, z-direction accuracy vs. x-grid spacing

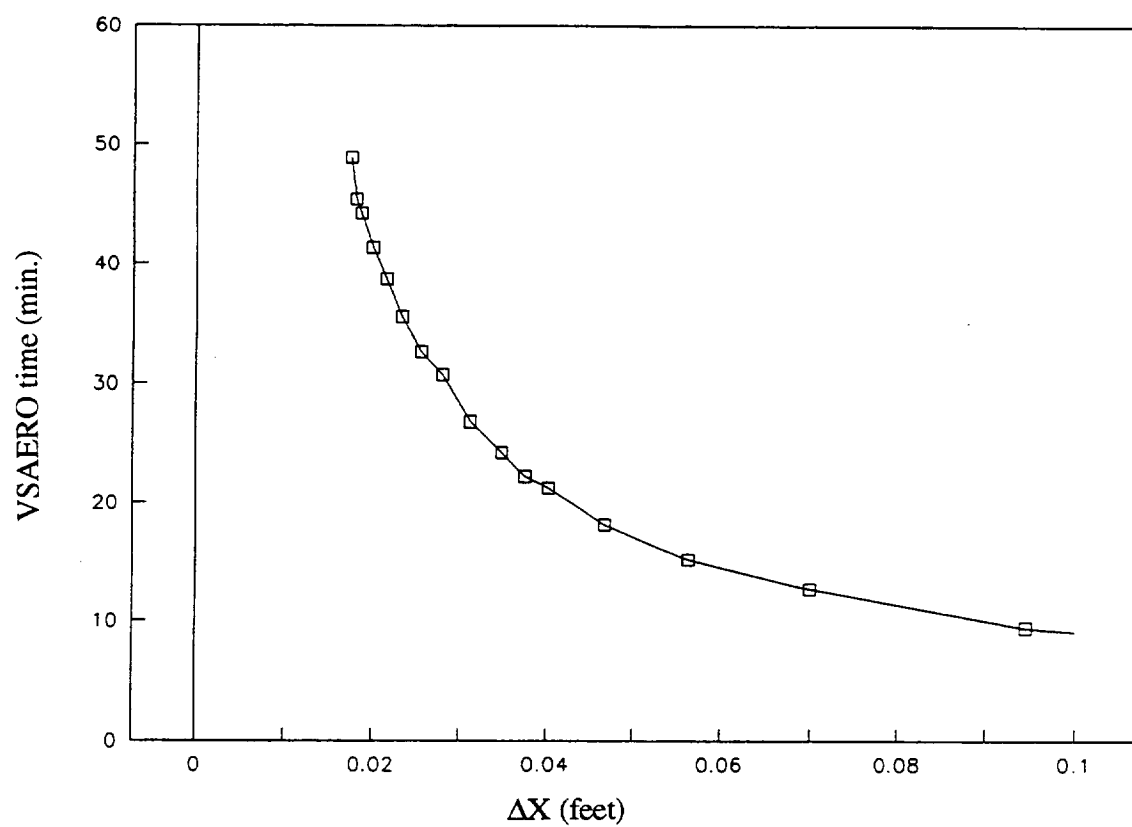Figure C.19 Grid resolution study, ?x50x25 grid, D=18.6 microns, maximum $V_{total,error}$ vs. x-grid spacing

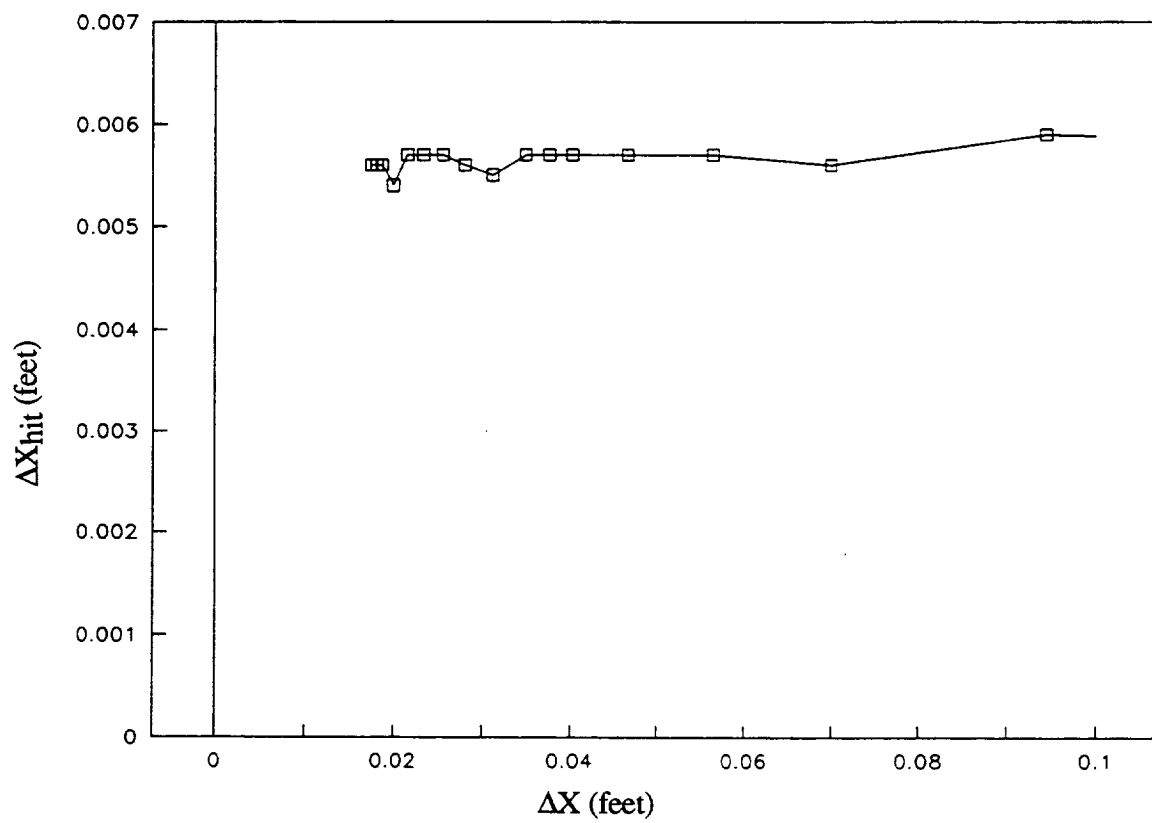Figure C.20 Grid resolution study, ?x50x25 grid, D=18.6 microns, VSAERO time vs. x-grid spacing

Figure C.21 Grid resolution study, ?x50x25 grid, D=14.7 microns, x-direction accuracy vs. x-grid spacing

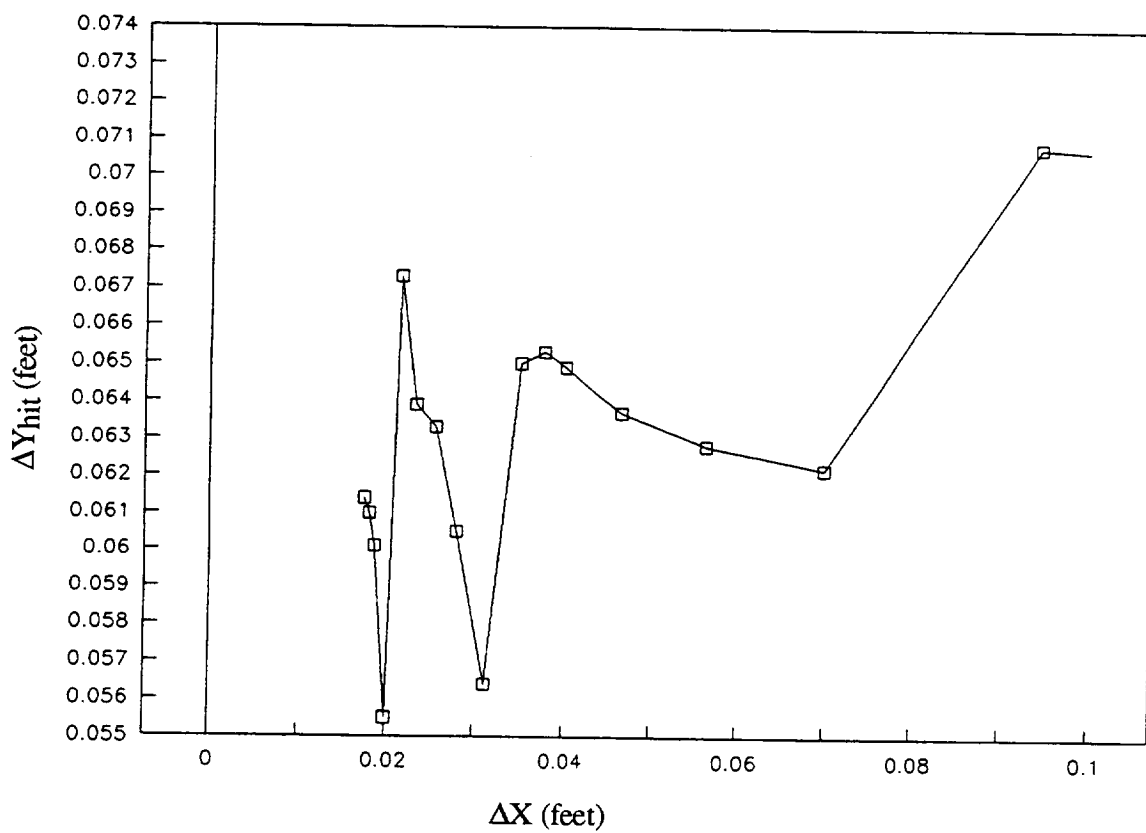Figure C.22 Grid resolution study, ?x50x25 grid, D=14.7 microns, y-direction accuracy vs. x-grid spacing
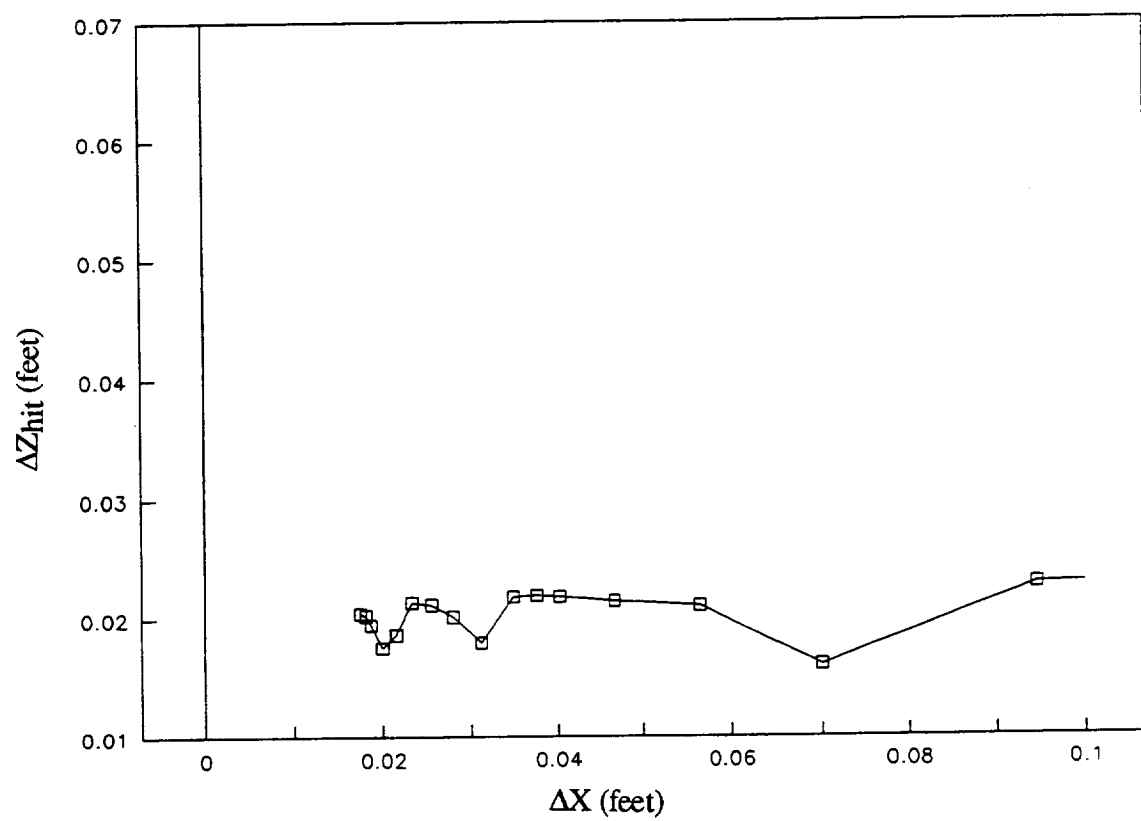
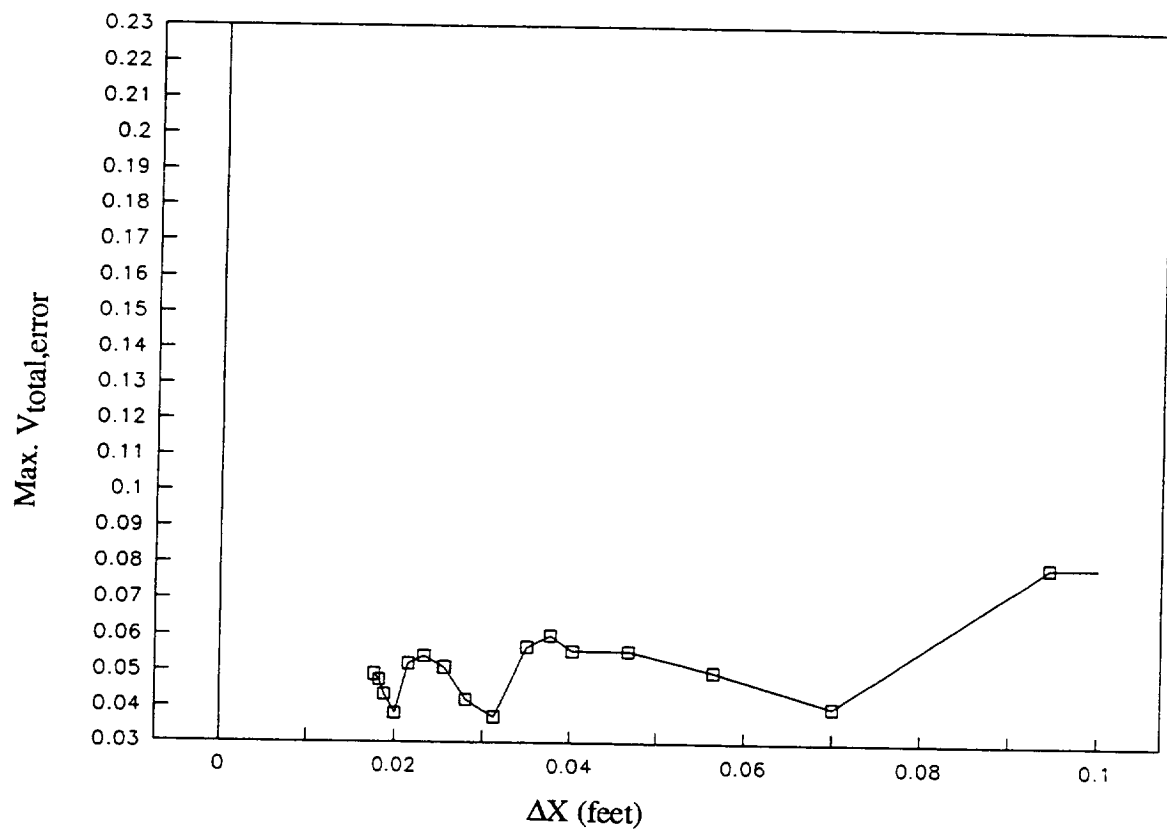Figure C.23 Grid resolution study, ?x50x25 grid, D=14.7 microns, z-direction accuracy vs. x-grid spacing

Figure C.24 Grid resolution study, ?x50x25 grid, D=14.7 microns, maximum $V_{total,error}$ vs. x-grid spacing
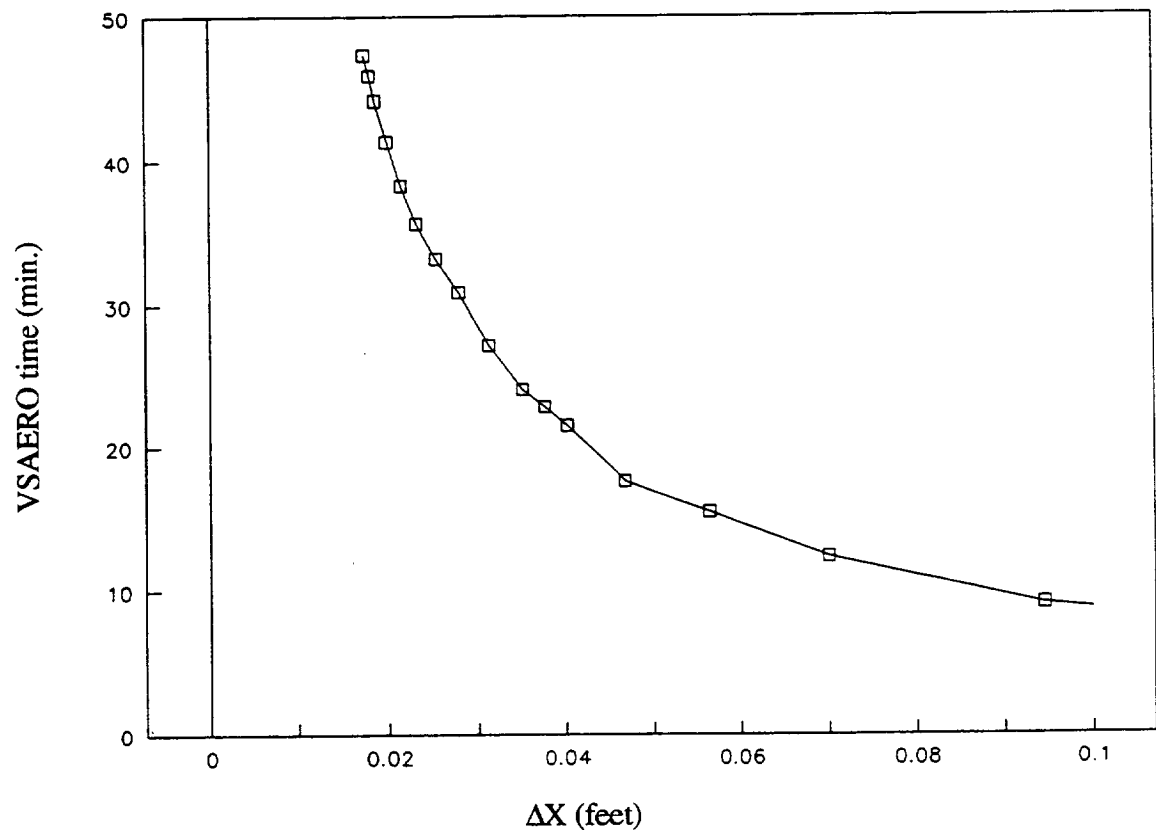
Figure C.25 Grid resolution study, ?x50x25 grid, D=14.7 microns, VSAERO time vs. x-grid spacing

Figure C.26 Grid resolution study, ?x50x25 grid, D=11.5 microns, x-direction accuracy vs. x-grid spacing

Figure C.27 Grid resolution study, ?x50x25 grid, D=11.5 microns, y-direction accuracy vs. x-grid spacing

Figure C.28 Grid resolution study, ?x50x25 grid, D=11.5 microns, z-direction accuracy vs. x-grid spacing

Figure C.29 Grid resolution study, ?x50x25 grid, D=11.5 microns, maximum $V_{total,error}$ vs. x-grid spacing

191

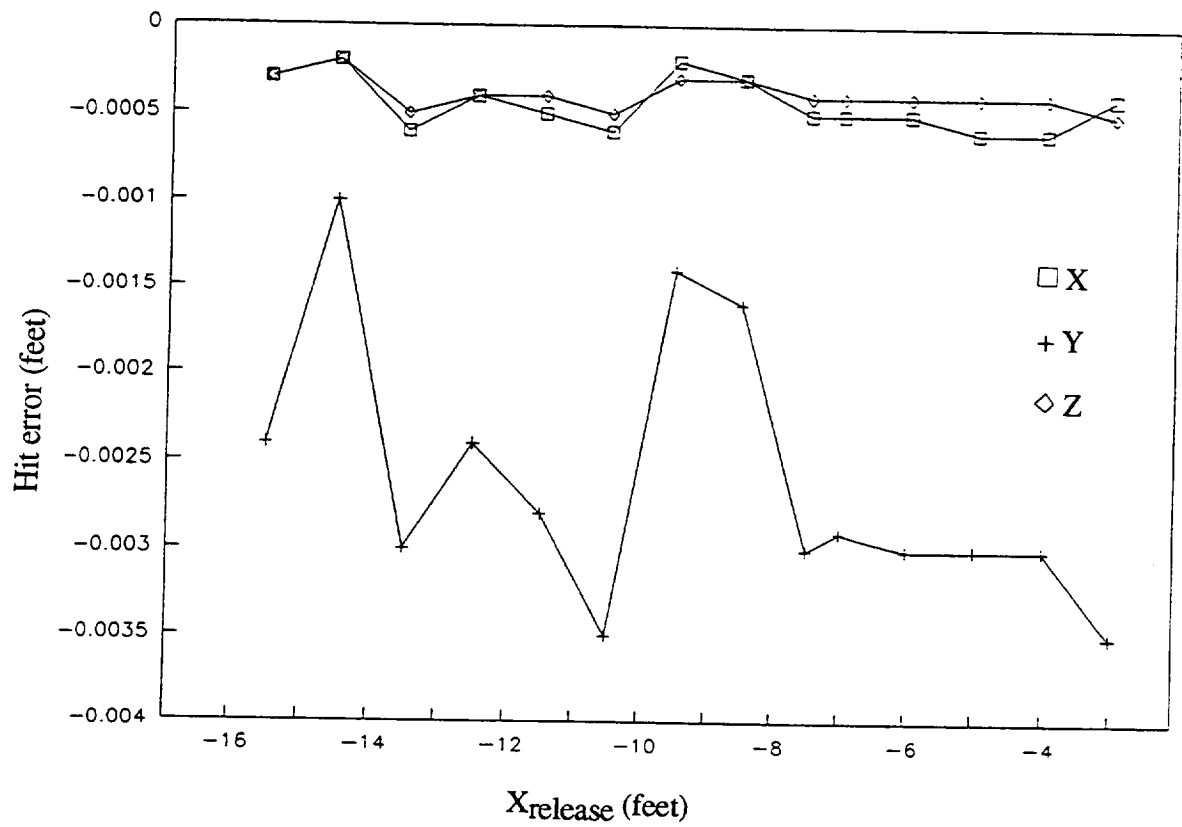Figure C.30 Grid resolution study, ?x50x25 grid, D=11.5 microns, VSAERO time vs. x-grid spacing

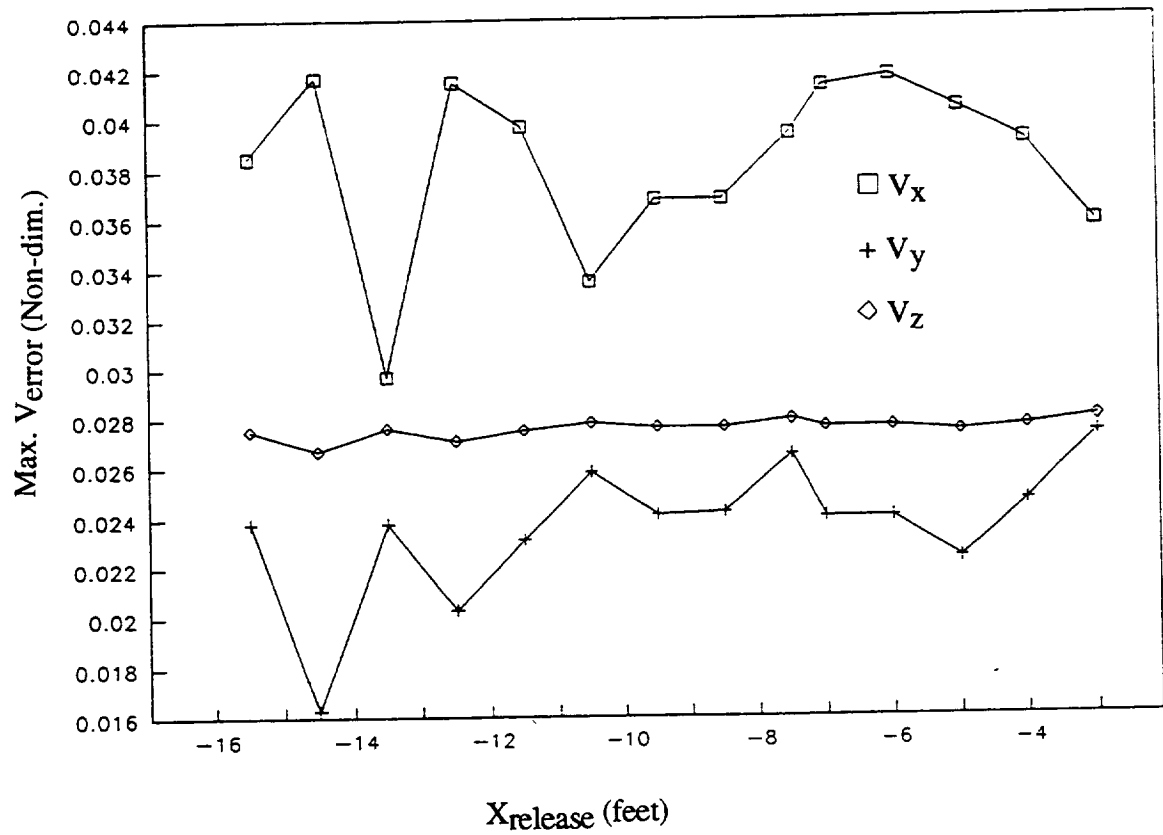Figure C.31 Trajectory length study, trajectory accuracies

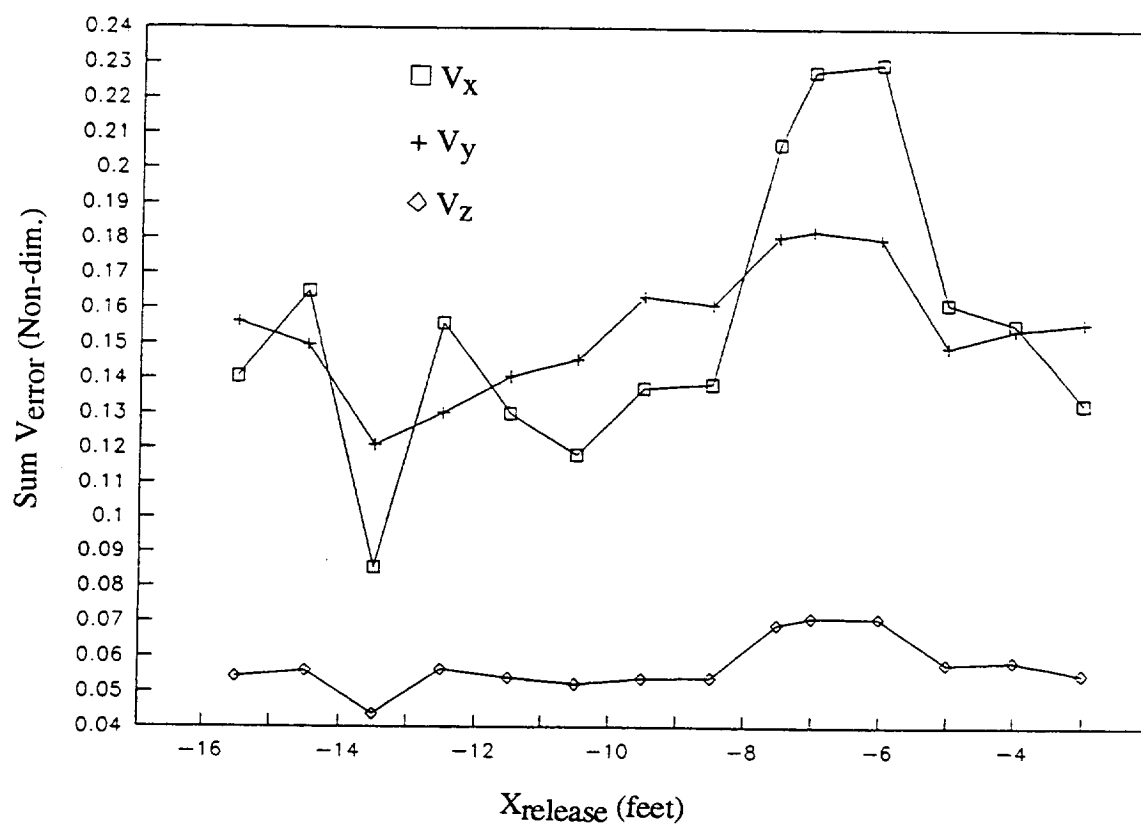Figure C.32 Trajectory length study, maximum velocity errors

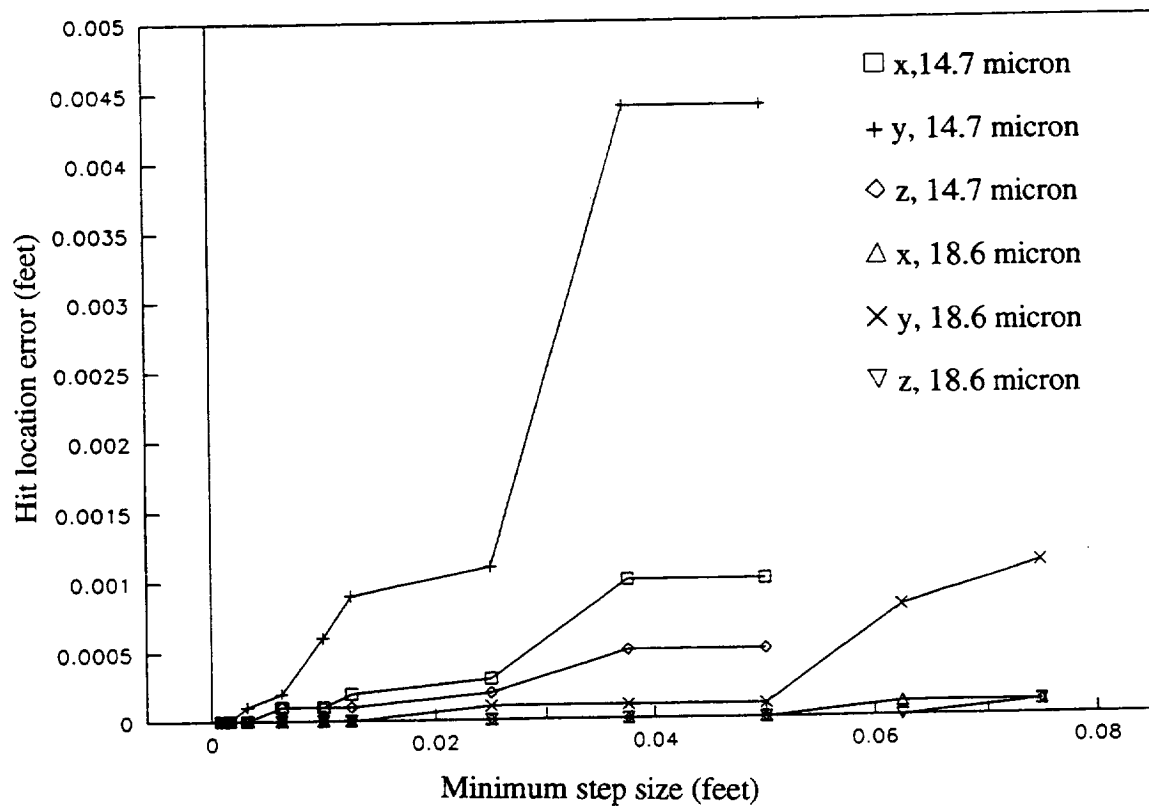Figure C.33 Trajectory length study, summed velocity errors

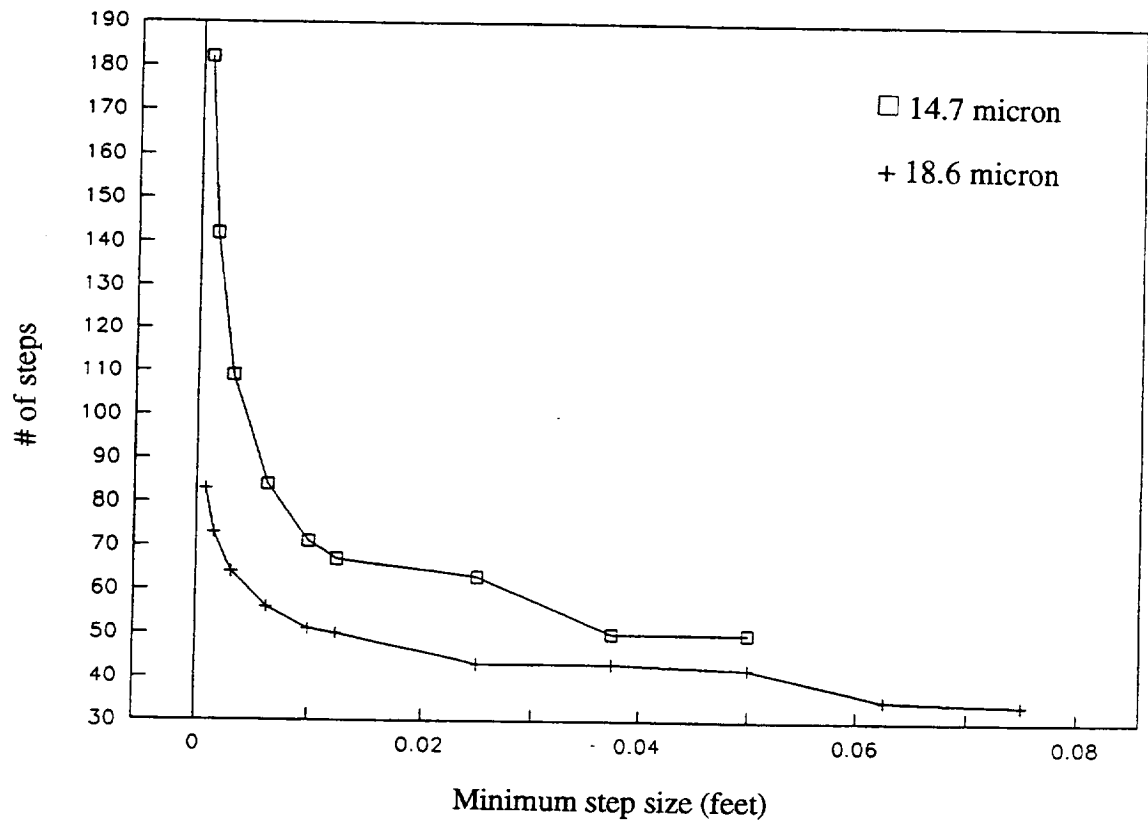Figure C.34 Minimum step size study, trajectory accuracies

Figure C.35 Minimum step size study, number of steps required

REPORT DOCUMENTATION PAGE

1. AGENCY USE ONLY (Leave blank)	2. REPORT DATE May 1996	3. REPORT TYPE AND DATES COVERED Technical Memorandum

4. TITLE AND SUBTITLE

Study of Water Droplet Trajectories in the NASA Lewis Research Center
Icing Research Tunnel (IRT)

5. FUNDING NUMBERS

WU–505–68–10

6. AUTHOR(S)

Andrew L. Reehorst

7. PERFORMING ORGANIZATION NAME(S) AND ADDRESS(ES)

National Aeronautics and Space Administration
Lewis Research Center
Cleveland, Ohio 44135–3191

8. PERFORMING ORGANIZATION REPORT NUMBER

E–10253

9. SPONSORING/MONITORING AGENCY NAME(S) AND ADDRESS(ES)

National Aeronautics and Space Administration
Washington, D.C. 20546–0001

10. SPONSORING/MONITORING AGENCY REPORT NUMBER

NASA TM–107221

11. SUPPLEMENTARY NOTES

Responsible person, Andrew L. Reehorst, organization code 2720, (216) 433–3938.

12a. DISTRIBUTION/AVAILABILITY STATEMENT

Unclassified - Unlimited
Subject Category 01

This publication is available from the NASA Center for AeroSpace Information, (301) 621–0390.

12b. DISTRIBUTION CODE

13. ABSTRACT (Maximum 200 words)

Water droplet trajectories within the NASA Lewis Research Center's Icing Research Tunnel (IRT) were studied through both experiment and computer analysis. Of interest was the influence of the wind tunnel contraction and wind tunnel model blockage on the water droplet trajectories. The computer analysis was carried out with a program package consisting of a three-dimensional potential panel code with integral boundary layer modeling and a three-dimensional droplet trajectory code utilizing a "local Stokes" approximation. An initial computational parameter study was performed using a spherical geometry to assess the accuracy of the computer code methodology. The gravity term was examined by calculating droplets falling in stagnant air. An experiment was conducted that consisted of a single moveable nozzle spraying water onto a grid installed in the center of the tunnel test section. Water impingement on the grid was recorded with the use of blotter paper. Agreement between the calculated trajectories within the IRT and the experimental data was found to be very good. The wind tunnel contraction was found to influence the water droplet cloud size distribution and liquid water content distribution across the test section from that at the inlet. The wind tunnel walls were found to have negligible influence upon the impingement of water droplets upon a wing model.

14. SUBJECT TERMS

Aircraft icing; Wind tunnels; Computational fluid dynamics

15. NUMBER OF PAGES

217

16. PRICE CODE

A10

17. SECURITY CLASSIFICATION OF REPORT Unclassified	18. SECURITY CLASSIFICATION OF THIS PAGE Unclassified	19. SECURITY CLASSIFICATION OF ABSTRACT Unclassified	20. LIMITATION OF ABSTRACT

National Aeronautics and
Space Administration

Lewis Research Center
21000 Brookpark Rd.
Cleveland, OH 44135-3191